DNA Motor-protein Hybrids for Molecular Transport and Self-organisation

ADAM WOLLMAN

A thesis submitted in partial fulfillment of
the requirements for the degree of
Doctor of Philosophy at the University of Oxford

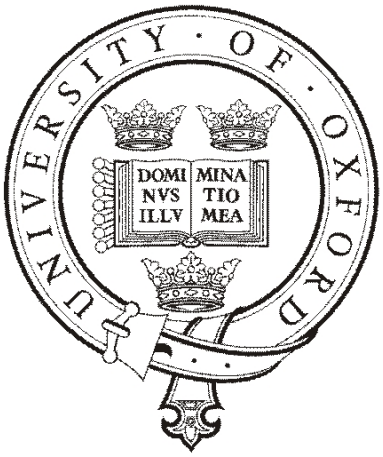

Linacre College
University of Oxford
Trinity Term 2013

DNA Motor Protein Hybrids for Molecular Transport and Self-organisation

Adam Wollman, Linacre College.
(Department of Physics)

Thesis submitted for the degree of Doctor of Philosophy
at the University of Oxford, Trinity Term 2013.

Abstract

Kinesin is a molecular motor which walks on microtubule tracks in the eukaryotic cytoskeleton. It transports cargo but is also involved in cytoskeletal organisation. This thesis demonstrates fusing kinesin and DNA to construct a molecular transport system using self-organised tracks and to study the mechanics of the minimal motor unit of kinesin.

The programmability of DNA allows for the formation of nanostructures with controllable interactions. Kinesin is conjugated to various DNA nanostructures to accomplish different tasks. Instructions encoded into DNA sequences are used to direct the assembly of a polar array of microtubules, to control the loading, active concentration and unloading of cargo on this track network and to trigger the disassembly of the network. Fluorescence microscopy was used to observe these microtubule arrays and the movement of cargo. It was found that the DNA signals used to control the unloading of cargo and the disassembly of the network had to be actively transported, rather than relying on diffusion, for effective delivery of the signal. This work lead to a first author publication, Wollman et al. (2013).

DNA was also used to study kinesin by linking defined numbers of minimal functional motor units, single kinesin heads, into teams of 4-12 heads and observing their movement along microtubules via fluorescent labelling. A minimum of 5 heads were required for sustained movement, in agreement with the predictions of Hancock and Howard (1998). The velocity of teams

increased with more heads, up to 8, and then a decrease was observed in teams with more heads.

Acknowledgements

I would like to thank the many people that have helped and contributed to my work over the years. Firstly, I would like to thank my supervisor, Prof. Andrew J. Turberfield for all his support, advice, ideas and guidance. I would also like to thank Dr Carlos Sanchez-Cano and Dr Helen Carstairs. My work would not have existed without the foundation laid by Helen and her expert training, guiding me through my first pipettes. Likewise, Carlos for all he has taught me, our (not so) heated arguments and so many cups of coffee. The kinesin side of the project was supervised by our expert collaborators, initially at the Marie Curie Research Institute (MCRI) in Oxted, Surrey and then later at the Centre for Mechano-chemical Cell Biology (CMCB) at the University of Warwick. I thank Prof. Rob Cross for all his advice and ideas and also Dr Maria Alonso, Dr Doug Drummond and Dr Miho Katsuki for welcoming us to their lab and helping us to use their equipment. Past and present members of DNA group, Shelley Wickham, Anthony Genot, Richard Muscat, Anthony Walsh, Daniele Selmi, Mireya Mckee, Jon Bath, Robert Machinek, Aiman Entwistle, Katherine Dunn, Alex Lucas, Florence Benn, Ibon Santiago, Thom Sharpe and Wenjing Meng made it an incredible place to work and I thank all of them for all their help and support. I would also like to thank the EPSRC for funding my work. Finally I would like to thank my family and my partner, Sarah.

Adam Wollman
Oxford, September 2013

To Sarah

Contents

Chapter 1

Introduction

All cells make use of a variety of different molecular motors for a huge array of different tasks. DNA and RNA polymerases unzip and traverse polynucleotides to copy or transcribe the genetic code. Rotary motors like F_1-ATPase generate ATP in mitochondria and the bacterial flagellar motor drives bacterial swimming. The cytoskeleton of eukaryotic cells serves as a transport network for a class of linear motors, kinesin, dynein and myosin. These motors not only use the cytoskeleton to transport cargo around the cell but are capable of re-organising their cytoskeletal tracks. They are well studied, partially because they are vital for cellular function but also for their potential use in nanotechnology.

The work presented here aims to harness the kinesin molecular motor and its abilities to transport cargo and organise its tracks but also, to better understand the motor's mechanics. This chapter reviews the current understanding of kinesin and the questions left to answer, as well as its role in self-organisation *in vivo* and the existing *in vitro* systems designed to harness it. New work is presented in the subsequent chapters. In Chapter 2, methods for harnessing kinesin for self-organisation are shown. These are used in Chapter 3 for a molecular transport system, controlled by encoded molecular signals. In Chapter 4, the system is modified to allow molecular signals to interrupt self-organisation. The methods used to harness kinesin are re-purposed in Chapter 5 to study the mechanics of the motor.

1.1 Cytoskeletal Motors

Kinesin, dynein and myosin travel on the cytoskeleton. Myosin moves on actin filaments, whereas kinesin and dynein travel on microtubules. Both of these tracks consist of repeating binding sites for the motors so they move by stepping between binding sites, usually with two identical protein 'feet'. Not all motors translocate and each exists as a superfamily of different proteins adapted for often quite diverse functions. Taking myosin as an example, myosin 5 transports cargo but myosin 2 pulls strongly on actin inside

sarcomeres driving muscle contraction (Hartman and Spudich (2012)). Although having different chemo-mechanical cycles and using different tracks, kinesin and myosin step with a similar mechanism and are thought to have a common ancestor (Kull et al. (1998)). Despite dynein and kinesin sharing a track, dynein has a radically different structure (Kon et al. (2012)) and there have been only very recent insights into its stepping mechanism (Qiu et al. (2012)).

1.2 Kinesin

The kinesin motor protein is better characterised than dynein but many aspects of its behaviour are still unknown. In this section, the structure and mechanism of kinesin and its microtubule track are discussed. The cellular role of the different kinesin sub-classes is summarised and an overview is given of the questions left to answer about the protein.

1.2.1 Kinesin structure

Kinesin 1 was the first kinesin to be identified, from squid giant axons by Vale et al. (1985). It is also the most well characterised. The motor is a dimer composed of two heads bound by a protein coiled coil. The crystal structure, from Kozielski et al. (1997) is shown in Figure 1.1, with the two

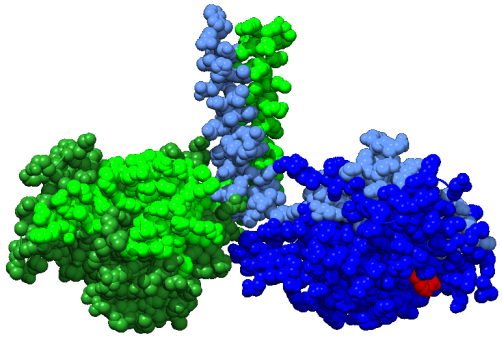

Figure 1.1: The crystal structure of dimeric rat kinesin 1 from Kozielski et al. (1997). The two heads of the protein are in green and blue and the ATP is in red.

heads in green and blue. The head domain can bind to the microtubule and also contains a catalytic domain for hydrolysing ATP. Hydrolysing ATP into di-phosphate ADP releases energy and serves as fuel for the motor. Motion between the two heads is coordinated, allowing them to walk along the microtubule. There is a region between the head and the coiled coil called the neck linker which is thought to be crucial for co-ordination. The step size has been experimentally determined to be 8nm (Svoboda et al. (1993)). Unless otherwise stated in the text, kinesin refers to kinesin 1.

1.2.2 Microtubules

The microtubule polymerises from two sub unit proteins, alpha and beta tubulin. A cryo-electron microscopy reconstruction of a microtubule (Sui and Downing (2010)) with the crystal structure of the alpha-beta tubulin dimer (Nogales et al. (1998)) is shown in Figure 1.2. These subunits use the

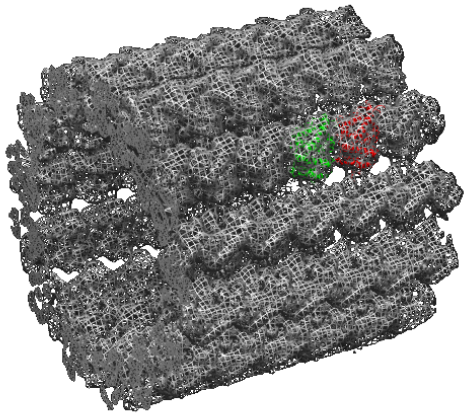

Figure 1.2: Cryo Electron Microscopy reconstruction of a microtubule (Sui and Downing (2010)) with the crystal structure of the alpha and beta tubulin subunits (Nogales et al. (1998)) shown in red and green respectively.

energy from hydrolysing the nucleotide guanosine tri-phosphate (GTP) to polymerise into protofilaments. For microtubules spontaneously assembled from mammalian tubulin, 10-15 of these filaments bundle together to form a microtubule (Desai and Mitchison (1997)). There is a slight offset between the protofilaments, making the microtubule chiral. Unless 10 or 16 protofilaments bundle together, the microtubule has a visible seam in cryo-electron microscopy reconstructions (as the summed offset of the protofilaments does not equal the tubulin spacing). The microtubule has two ends, a fast growing plus end and slow growing minus end. Growing stops when a cap of unhydrolysed GTP forms at the plus end (Gardner et al. (2013)). This cap is eventually hydrolysed and the microtubule collapses; this is known as catastrophe. *In vivo* microtubules cycle through growing and collapsing states. *In*

vitro, microtubules can be stabilised using a compound, originally discovered in the Pacific yew tree, called taxol which binds between the alpha and beta subunits, halting growth and collapse.

1.2.3 The Kinesin Family

There are a family of different kinesins, each adapted to a specific task in the cell. From observations made using electron microscopy, five major kinesin classes were initially discovered. From analysis of the mammalian genome, 45 kinesin genes have been identified (Hirokawa et al. (2009)). They have now been grouped into 15 classes, kinesin 1 to 14 (14 is split into 14A and B) (Lawrence et al. (2004)). They can also be placed into three groups, depending on the location of the motor domain within the protein. N-kinesins have a motor domain in the amino, N-terminus; M-kinesins have a motor domain in the middle and in C-kinesins, the motor domain is at the carboxyl C-terminus. In general, N-kinesins move towards the plus end of the microtubule and C-kinesins move towards the minus end. M-kinesins do not translocate but depolymerise the microtubule (Hirokawa et al. (2009)). M-kinesins are only found in the kinesin 13 subclass and C kinesins are only found in the kinesin 14A and B classes. All other classes consist of N-kinesins. Most kinesins transport various cargoes including organelles, protein com-

plexes and mRNA (Verhey et al. (2011)) but some perform other functions.

Kinesins 5 and 14 are required for eukaryotic cell division (Subramanian and Kapoor (2012)). Kinesin 5 is required for bipolar spindle assembly. It is a homotetramer which can cross-link microtubules by binding to each with a pair of motor domains. Kinesin 14 is needed to organize the two poles of the bipolar spindle. This motor cross links microtubules by attaching to one with a non-motile domain and a minus end directed active motor domain to the other. The mechanism of kinesin 14 is further discussed in Section 1.4.1.

Kinesin 8 and 13 can destabilise or depolymerise microtubules (Verhey et al. (2011)), to regulate length. Kinesin 13 helps regulate the size of microtubule structures and in establishing chromosome microtubule attachments during mitosis (Wordeman (2005)). Kinesin 8 is needed for chromosome alignment to the spindle equator (Gardner et al. (2008)). These proteins destabilise microtubules using different mechanisms. Kinesin 13 finds the microtubule end by 1D diffusion and stabilises curved protofilaments, promoting depolymerisation (Subramanian and Kapoor (2012)). Kinesin 8 actively walks to the end of the microtubule. It destabilises longer microtubules more than shorter ones as more motors accumulate on longer microtubules. At the ends, co-operative action between kinesin 8s, displaces kinesin 8 bound to tubulin dimer, promoting depolymerisation (Varga et al. (2009)).

1.2.4 Chemo-mechanical cycle

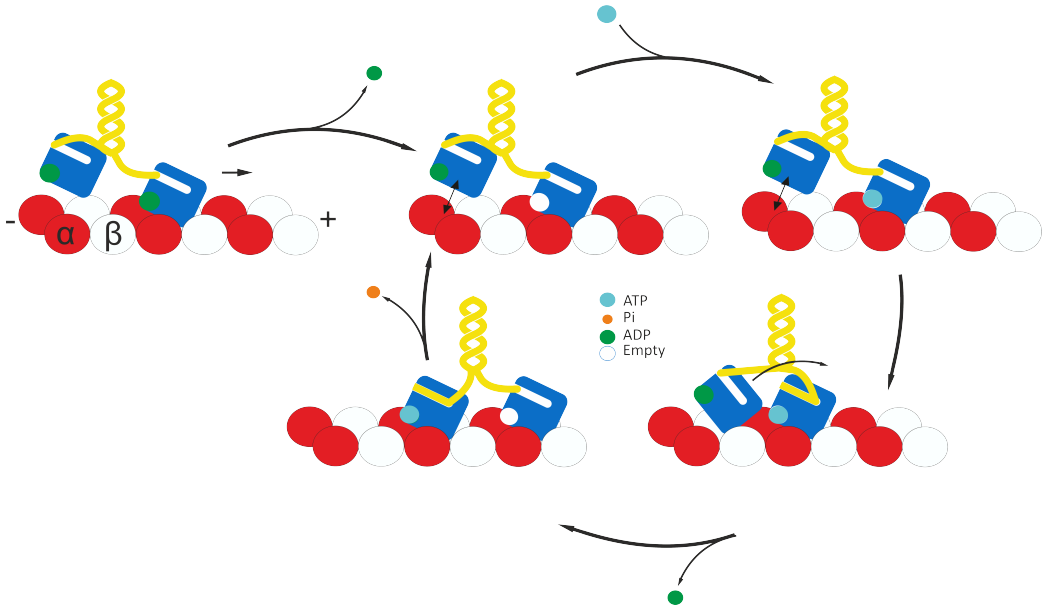

Figure 1.3: The Chemo-mechanical cycle of kinesin. The microtubule is in red and white, kinesins heads in blue and neck in yellow. One head binds in the ADP containing state which catalyses the release of nucleotide. The free head tends not to bind until the bound head binds ATP. ATP hydrolysis in the first head induces a conformational change in the neck linker which biases the free head forward. The free head binds, catalysing release of its nucleotide and the previously bound head releases phosphate and detaches from the microtubule.

Kinesin movement is coupled to the hydrolysis of ATP (Hua et al. (1997)) with one molecule of ATP hydrolysed (Coy (1999)) per 8nm step (Schnitzer and Block (1997)). It can take many steps before disassociating (Howard et al. (1989); Svoboda and Block (1994)). The full walking cycle is illustrated in Figure 1.3. Initially, one head binds in the ADP containing state; binding catalyses the release of nucleotide (Hackney (1994); Ma and Taylor (1997); Gilbert et al. (1998)). The free head tends not to bind until the bound head binds ATP (Hackney (1994)) but without necessarily hydrolysing nucleotide

(Ma and Taylor (1997); Gilbert et al. (1998)). This free head undergoes a diffusional search for the next binding site (Mather and Fox (2006)) until ATP hydrolysis in the first head induces a conformational change in the neck linker (Rice et al. (1999)) which biases the free head forward. The free head binds, catalysing release of its nucleotide and the previously bound head releases phosphate and detaches from the microtubule (Cross (2004b)). In this way kinesin can take ∼100 steps/second and >100 before dropping off (Svoboda and Block (1994)). In gliding assays, where a surface is coated in kinesin heads and microtubules are observed gliding over them, motors move microtubules at 800nm/s (Howard (1996)).

1.2.5 Stepping mechanism

There are three possible stepping mechanisms for a two footed stepping motor: an inchworm model where the front head steps forward and then the trailing head steps forward to catch it up; and a hand over hand model where feet step over each other in either a symmetric or asymmetric gait (Asbury (2005)). It is now well established that kinesin walks with an asymmetric hand over hand mechanism. Kaseda et al. (2003) created a hetereodimeric kinesin with a head mutated in the nucleotide binding pocket. They saw alternate fast and slow stepping, inconsistent with an inchworm model. Yildiz

et al. (2004) labelled one head with a fluorophore and detected 16nm steps, also inconsistent with the inchworm model. The mechanism was shown to be asymmetric by Hua et al. (2002). They used a truncated kinesin stiffly bound to a surface and observed the rotation of microtubules bound to motors. A 180° rotation is expected for the symmetric hand over hand mechanism, as the entire protein would swivel 180° during a step, but only small rotations were observed.

There is still some uncertainty as to whether kinesin steps along a single protofilament. It has been shown that kinesin walks parallel to the microtubule protofilament axis (Kuo et al. (1991); Ray (1993); Shibata et al. (2012)), even under sideways load (Block et al. (2003)) but it is unclear if kinesin is walking on one protofilament, straddling two or a random walk averaging to one (Cross (2004a)).

1.2.6 Force Production

There is a discrepancy between the tubulin dimer spacing on the microtubule of 8nm and the distance between the two kinesin heads of 5nm (Kozielski et al. (1997)). The kinesin neck section, the dimerisation domain of the coiled coil and the neck linker region, is highly conserved in plus end directed kinesins (Vale and Fletterick (1997)) and essential for motility (Case et al.

(2000)). Mutating sections of the neck (Romberg et al. (1998)) and chemically cross-linking sections of it (Tomishige and Vale (2000)) have shown that conformational changes to the neck linker, rather than unwinding of the coiled coil, allow for motility. Specifically the neck linker must be allowed to undock (Hahlen et al. (2006)). Rice et al. (1999) have shown that the neck linker is undocked and in a mobile conformation when the head is in the ADP state and docked when the head is bound to ATP and the microtubule. Labelling the head and neck linker with FRET pairs (Tomishige et al. (2006)) showed alternating FRET states in the leading and trailing head, consistent with docking and undocking.

It has been proposed that neck linker docking is the kinesin force producing step (Rice et al. (2003)) but the ∼2nm displacement of the neck linker is not enough to explain the ∼8nm kinesin step size (Kawaguchi (2008)) and the free energy of neck linker docking is only 5% of hydrolysis (Rice et al. (2003)). Even with kinesins 50% efficiency (Block (2007)), there is an energy mismatch, and so diffusion must play a role in finding the next binding site. A Brownian ratchet mechanism has been proposed (Taniguchi et al. (2005)) and also some structural aspects of the microtubule may produce a forward bias (Kikkawa (2008)).

The neck linker plays an important role in coordinating the heads (see

Gennerich and Vale (2009) for a review of co-ordination). Crevel et al. (2004); Schief et al. (2004) have shown that mechanical strain through the neck linker increases ADP detachment from the rear head. Yildiz et al. (2008) created kinesin mutants with extended neck linkers which decreased the mechanical tension between heads. These motors remained processive but were slower. Velocity could be restored by applying tension either by chemically cross-linking the neck linkers or using an optical trap.

1.2.7 Waiting state of the rear head

The waiting state of the rear head remains unclear (Block (2007); Kawaguchi (2008)). Electron microscopy studies show both 1 and 2 head binding in both nucleotide free and adenosine 5-(β, γ-imido)triphosphate bound states (AMP PNP is a non-hydrolysable analogue of ATP) (Hirose et al. (1999); Arnal and Wade (1998); Thormählen et al. (1998); Hoenger et al. (1998)). All of these studies were conducted far from physiological conditions, at saturating kinesin concentration (Block (2007)). An optical trap study by Uemura et al. (2002) found that the force to detach single headed and double headed kinesin in the ADP state was the same, implying 1 head binding. However the alternating 16nm and 0nm steps found by Yildiz et al. (2004) imply 2 heads bound. These findings are complicated by the observations of Alonso et al.

(2007). They studied kinesin dimers binding to free tubulin dimers. In the ADP state each kinesin dimer bound one tubulin dimer but using AMP PNP, both heads bound to one dimer each. Mori et al. (2007) conducted a single molecule FRET assay and came up with a consistent model to explain the conflicting results. They found that at saturating ATP, both heads remain bound to the microtubule most of the time but at low ATP, where waiting for nucleotide is the rate limiting step, the results are consistent with the rear head quickly unbinding and waiting close to the bound head for it to bind ATP.

1.2.8 Obstacles

There is some controversy around kinesin behaviour upon encountering obstacles on the microtubule. Crevel et al. (2004) found accelerated kinesin unbinding using light scattering and photolysis (laser induced release of caged nucleotide) when rigor kinesin mutants were used as road blocks. This result is in apparent contradiction with some single molecule studies. Seitz and Surrey (2006) decorated microtubules with a mutant kinesin which could take one step and then tightly bind to the microtubule. The mutant could release with ATP but 10 times slower than conventional kinesin. They followed quantum dot labelled kinesins moving on the decorated microtubules

and found reduced velocities but similar run lengths. They interpret this to mean that kinesin waits until the roadblock is removed. Similar results were obtained by Leduc et al. (2012) using active motors as roadblocks. Korten and Diez (2008) used biotinylated microtubules decorated with streptavidin roadblocks. They found that kinesin paused at blockages but that ∼50% restarted. This implies kinesin was able to manoeuvre around the block. Dreblow et al. (2010) produced similar results using chemically cross-linked kif5A as obstacles with kinesins passing by after pausing. Telley et al. (2009) investigated a range of different obstacles, rigor kinesin mutants, active wild type kinesin and cell extract containing a complex mixture of microtubule associated proteins. They found the run length of kinesin was strongly reduced but they did see some evidence that motors could move past obstacles.

1.2.9 Minimal Motor Unit

Wild type kinesin-1 is a dimer but studies have shown that artificially truncated constructs which have only one head are still motile. The part of the protein is thus the minimal motor unit and understanding its motility is important for understanding the operation of the full motor. It is unclear if a single head can produce processive motility or how many heads are required for processive motion. The optimum number of heads is also unknown.

Gliding assays at various single head motor densities were performed by Hancock and Howard (1998). Single headed motors moved towards the plus end of microtubules at 0.096± 0.030 μm/s. Movement was uneven compared to double headed motion, which may be caused by dead heads interacting with gliding microtubules or contaminating dimers. Dead heads were removed by pelleting microtubules and kinesins without ATP, in a centrifuge - removing all heads incapable of binding microtubules - and then adding ATP so that heads capable of hydrolysing nucleotide detach and those which cannot are removed. Removing dead heads did not change microtubule motion. Using sucrose density centrifugation, no contaminating dimers were observed and so the authors conclude that the uneven motion is due to single head gliding. Surface motor density was estimated from the concentration of motors used and was very uncertain. Below 10 motors/μm^2 microtubules swivelled on the surface (indicating single molecules interacting (Hunt and Howard (1993))) and diffused back into solution without movement. There was also a steep decline in the rate at which microtubules landed on the surface below 100 motors/μm^2, indicating that more than 1 motor is required for movement. The authors fit their data to a model which assumes microtubules bind randomly to the surface and move if they encounter n motors. For wild type dimers *n=1* but for single heads the best fit to the data was with *n=4*. There is uncertainty in this analysis caused by the difficulty in

determining the surface density, so the authors suggest 4-6 motors are needed for continuous movement. They suggest that when an insufficient number of motors is present, motors unbind very slowly. Wild type heads must detach at $50s^{-1}$ to step 100 times/second but single heads only detach at $0.3s^{-1}$ (Hancock and Howard (1999)) so the second head must increase detachment rate by orders of magnitude. To produce velocities of 100nm/s in the gliding assay, single heads need to detach at $12s^{-1}$ or higher if the single head step size is <8nm, which implies some communication between heads.

The number of heads needed for movement can also be determined from single molecule studies, observing motors moving on microtubules. Most studies have shown that single kinesin heads cannot move processively by themselves (Hancock and Howard (1999); Bieling et al. (2008); Kamei et al. (2005); Vale et al. (1996)) but Inoue et al. (2001) found some movement of single heads. Observing fluorescently labelled single heads moving on microtubules, Inoue et al. (2001) saw some heads moving as far as 600nm before detaching. They also observed many back-steps such that the run length distribution is centred almost at zero. Figure 1.4 shows the run length distribution from Inoue et al. (2001) of single heads moving on microtubules. When ATP is present, there is a slight forward bias of the motors with a mean run length of 38±8nm and mean velocity of 40±3nm/s but it is unclear

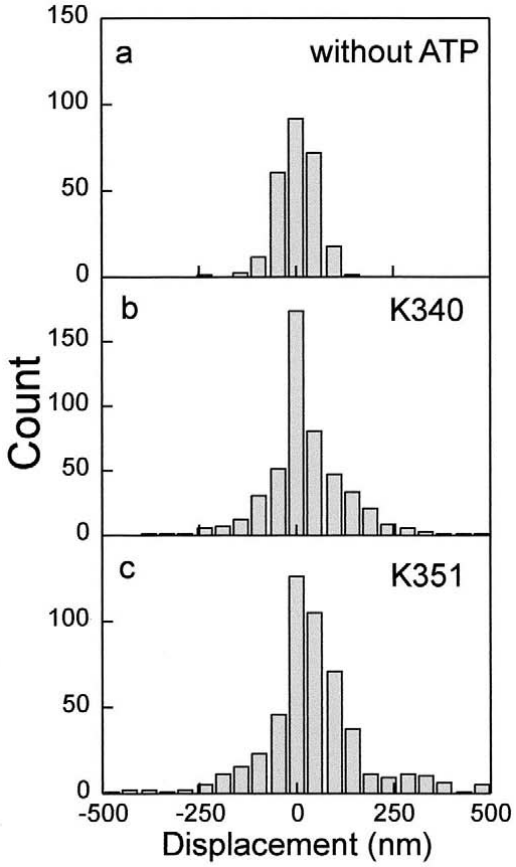

Figure 1.4: Run length distributions of single headed motors truncated at the 340th amino acid (at the neck linker) and 351st amino acid (just before neck linker) from Inoue et al. (2001). **a** the 340 amino acid construct with no ATP. **b** the 340 amino acid construct with ATP. **c**. the 351 amino acid construct with ATP.

whether this can be considered processive motion.

It may be possible to restore processive movement by linking two or more motors together. Kamei et al. (2005) investigated beads coated with single heads in a laser trap. The number of motors bound to a bead was estimated from the concentration of motors by a Poisson distribution. The number of motors interacting could then be estimated from the bead geometry. Single

heads were not found to move processively but two heads could displace the bead by ∼50nm. The bead velocity remains constant at 350nm/s with up to 10 motors on the bead (2 interacting with the microtubule) and decreased steadily above this to 230nm/s at >60 heads per bead (3 interacting with the microtubule). These velocities are significantly faster than the gliding velocity of their motor construct of ∼120nm/s which they suggest may be due to crowding. If this were the case Hancock and Howard (1998) should have observed faster gliding at lower kinesin concentrations but gliding velocity remained constant.

Defined numbers of single heads have been linked together using DNA (Miyazono et al. (2009)) and protein (Diehl et al. (2006)). Miyazono et al. (2009) mutated a single headed kinesin to have only one exposed cysteine at the coil end and attached maleimide modified DNA. They created dimers in this way and observed their movement on microtubules. Mean velocity was 235nm/s with run length of 130nm, thus dimer behaviour was not restored. They attribute the poor performance of their dimer to lack of coiled coil residues. Diehl et al. (2006) also did not observed dimer velocities to be restored with their construct. They created single heads with a leucine zipper motif which could be linked together with an elastin linker. The ATPase rate increased with 2 motors but no further for 3. Gliding velocity also increased

slightly from 0.03μm/s for 1, 0.07μm/s for 2 and 0.08μm/s for 3.

1.2.10 Teams of motors

In the cell, kinesins work in teams (Verhey et al. (2011)) and so a number of studies have investigated teams of defined numbers of motors. Rogers et al. (2009) used a similar method to Diehl et al. (2006) to link two double headed motors together and observe them moving on sea urchin axonemes. They found an increase in run length from 800 to 1300nm but identical velocity for both of 500nm/s. Off axis events were seen where a motor detached, swivelled and rebound. A similar construct was used by Jamison et al. (2010) in an optical trap. The distribution of detachment force for a single dimer peaks at 7.3pN and drops off suddenly; with two dimers it is broader (up to 17pN) but peaked at 5.6pN. This implies kinesins within assemblies influence each other's dynamics, increasing detachment rates, and implying that only one motor is interacting with the microtubule at any one time. A study by Derr et al. (2012) observed teams of up to 7 kinesin dimers on a DNA origami moving on microtubules. They also saw an increase in run length but no change to velocity, even with 7 motors, which they also attribute to only one kinesin interacting per team. A similar study by Furuta et al. (2012) saw the same increase in run length but they did observe a slight decrease in speed

with number of kinesins. These studies imply that communication between motors in teams leads to co-operative detachment such that there may only be one motor interacting with the microtubule at one time (Jamison et al. (2010); Derr et al. (2012)).

1.3 Organised Microtubules *in vivo*

Cells need to organise themselves. They must interact mechanically with their environment, keep the correct shape and change it if need be, be physically robust, internally structured and move around. They achieve all of this using motor proteins and their accompanying filaments, self organised into the cytoskeleton and a range of other structures discussed in this section.

1.3.1 Cytoskeleton

The cytoskeleton is a self-organised cellular scaffold of microtubules, actin and intermediate filaments. It fulfils structural functions in eukaryotes by supporting the fragile plasma membrane and bears strain on the cell through mechanical linkages. It also performs this function in plants where it guides the formation of the cell wall. The cytoskeleton also helps produce internal structure by cellular transport, driving and guiding organelles. Microtubules, being much more rigid than actin or intermediate filaments and supporting

more processive motors, provide a lot of this functionality.

In interphase cells, cytoplasmic microtubules are arranged into a star like array. This organisation occurs from a microtubule organising centre (MTOC) called a centrisome located near the nucleus. A special γ-tubulin forms around a γ-tubulin ring complex (γ-TuRC) which, in turn, nucleates the growth of microtubules (Zheng et al. (1995)). There are more than 50 copies of γ-TuRC in the centrisome (Moritz et al. (1995)). Thus a microtubule array with astral plus ends grows from the centrisome. This arrangement is very robust and acts to survey the outlying regions of the cell and position the centrisome at the centre. This behaviour has been replicated *in vitro* in micro-fabricated chambers serving as an artificial enclosure (Holy et al. (1997), discussed further in Section 1.4.2). The ability of the microtubule cytoskeleton to locate the cell center, defines a general coordinate system used to position organelles. It also helps position the endoplasmic reticulum almost to the cell periphery while the Golgi apparatus remains at the centrisome.

1.3.2 Mitosis and the mitotic spindle

Kinesin and microtubules also play a vital role in mitosis. Figure 1.5 shows drosophila embryos at different stages during mitosis from Rogers et al.

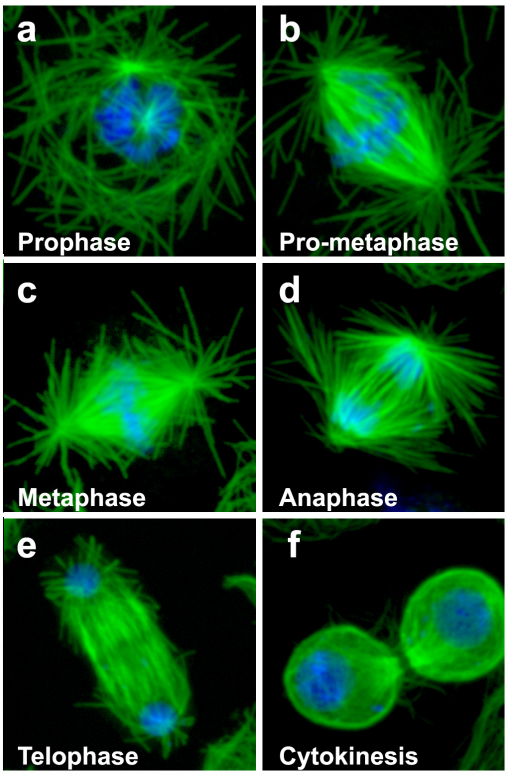

Figure 1.5: Drosophila embryos, tubulin stained green and DNA in blue, undergoing **a** prometaphase **b**, metaphase **c**, anaphase **d**, telophase **e**, and cytokinesis **f** from Rogers et al. (2002).

(2002). During the prophase of mitosis, the centrisome duplicates and splits. Each new centrosome travels to the opposite side of the cell in pro-metaphase. The cytoskeleton completely re-arranges, during metaphase, as microtubules nucleate from each centrisome to form the mitotic spindle. Spindle microtubules bind chromosomes through a large protein complex called the kinetichore. Chromosomes are pulled apart into their sister chromatids, into each half of the dividing cell by retreating spindle microtubules during anaphase. Kinesins, specifically kinesin 5 and 14 class members (Subramanian and Kapoor (2012)), help maintain and organise the mitotic spindle.

1.3.3 Cilia and Flagella

Microtubules are also organised into cilia and flagella. These are hair like appendages incorporating bundles of microtubules. Flagella are found on sperm and protozoa. It is their undulating motion that allow these cells to swim. Cilia are organised similarly to flagella. They move by beating with a whip like motion. Multiple cilia beat slightly out of sync with each other, producing a wave like motion (a metachronal wave(Sanderson and Sleigh (1981))). They can propel single cells such as the swimming protozoan Paramecium or, when coating a tissue surface, move fluid. The human respitory tract is covered in 10^9 cilia per cm^2 (Carson and Collier (1981)) where they remove mucous, dust or bacteria. Similarly uterine cilia move the ovum into the oviduct.

Figure 1.6: Electron micrograph of cross section of a human respiratory cilia from Satir (2011). 1. Dynein arm, 2. Nexin links and 3. Radial spokes.

Cilia and flagella movement is produced by bending a core called an axoneme. This core is composed of a distinct pattern of doublet microtubules around a central pair of microtubules, shown in Figure 1.6. The doublet microtubules consist of a half formed microtubule around a complete one. The axoneme arrangement is found in almost all eukaryotes, from protozoa to humans (Popodi et al. (2008)). The doublet microtubules are held from the centre by radial spokes and connected to each other by elastic nexin links, which resist the sliding motion produced by dynein (Lindemann and Lesich (2010)). Ciliary dyneins protude from doublet microtubules and bind to neighbouring doublet microtubules (Gibbons (1966)). When these motors are active, they walk along microtubules until prevented by the structure. The force produced by these motors rectifies as a bending of the axoneme and in this way drives the bulk movement of the structure (Warner and Satir (1974)). Side to side motion is thought to arise from switching between the dyneins on either side (Lindemann and Lesich (2010)) of the axoneme.

1.3.4 Axons and dendrites

Neurons start in the embryo as unremarkable cells and then migrate to specific locations. Once there they send out long protrusions called neurites. They contain microtubule bundles and either receive electrical signals, in

which case they are called dendrites, or transmit them, called axons. In axons the microtubules are orientated in the same direction with the minus end back toward the cell body and the plus end to the axon terminal. Microtubules are staggered along the axon as it can be vastly longer than an individual microtubule. The longest axon in the human body is ∼1m (Goldstein and Yang (2000)) and runs from the base of the spinal cord to the tip of the big toe. Kinesins power fast axonal transport (Amaratunga et al. (2002)) where mitochondria, specific proteins in transport vesicles and synaptic vesicle precursors are transported (Goldstein and Yang (2000)). They travel away from the cell (anterograde) while, negative end motors take used components back to the cell for recycling (retrograde).

1.3.5 Melanophore

An interesting use of molecular transport in biology is found in the melanophore in the cells of certain fish (Tuma et al. (1998)). This is a radial cytoskeletal arrangement which allows motor proteins to concentrate or disperse pigment containing melanosomes. When the pigment is dispersed, the cell is opaque and when concentrated, the cell is transparent. This allows the fish to change colour. Melanosomes are concentrated by dynein (Nilsson and Wallin (1997)) and dispersed by kinesin (Tuma et al. (1998)).

1.4 Organised microtubules *in vitro*

Some of the capability of kinesin and microtubules to self-organise has been replicated *in vitro*. Kinesin 14 has been used to create bundles of microtubules. Several methods for creating astral arrays of microtubules have been developed. It has even been possible to create very unnatural geometries including spools and ultra-long wires. Dynamic structures have also been created in the form of active bundles.

1.4.1 Bundles

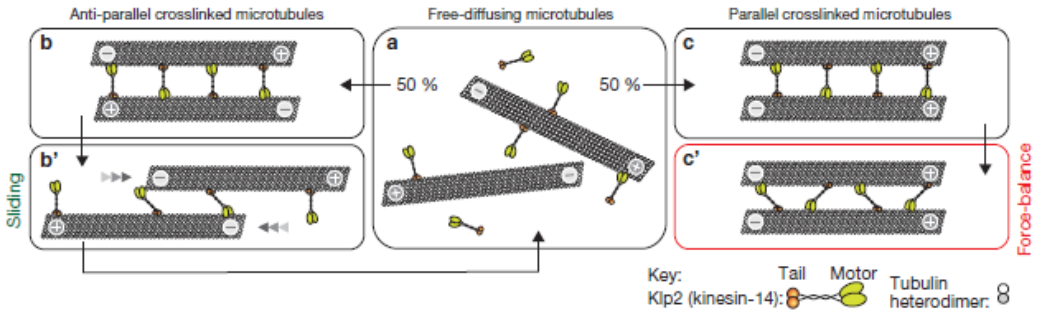

Figure 1.7: Schematic illustrating bundle formation from klp2 and S. Pombe microtubules from Braun et al. (2009). In **a** freely diffusing microtubules with bound klp2 encounter each other. If the microtubules are anti-parallel, they are slid apart as in **b** or if parallel a state of force balance locks them together into a bundle **c**.

A minimal system for forming parallel microtubule bundles was created by Braun et al. (2009). They found that microtubules and a kinesin 14, klp2, from fission yeast, Schizosaccharomyces pombe (S. Pombe), self organised into parallel bundles in the presence of ATP. Klp2 contains an active

homodimeric motor domain at the N-terminus and a non active domain at the C-terminus. These proteins can cross-link microtubules through the active and non-active motor domains. If anti-parallel microtubules are cross-linked, they will slide apart but parallel microtubules will bundle as the motors will be in force balance - illustrated in Figure 1.7.

1.4.2 Asters

Microtubule asters are an extremely important structure in cells utilised for molecular transport in the interphase array and important in mitosis. They are polar as all astral microtubules are aligned with their minus ends in the centre and thus define a general coordinate system in the cell. A number of systems have been developed to form asters *in vitro* by self-organising the microtubules with motors or by growing the microtubules from an artificial MTOC.

Self-organised asters

It was first demonstrated that asters could be self-organised by artificially created teams of motors by Nédélec et al. (1997). Asters had previously been found to self assemble in Xenopus egg extracts (Heald et al. (1996)). Nédélec et al. (1997) created a biotinylated kinesin which was bound to streptavidin tetramers in a ratio of four to one. When mixed with microtubules, these

teams capture and cross-link microtubules. As the motors can only walk towards one end of the microtubule, in this case the plus end, the microtubules are sorted by polarity. The action of many of these teams aligns the microtubules into radial asters (the assembly mechanism is further discussed in Chapter 2 Section 2.7.1). Most of this work used dynamic microtubules but asters were also demonstrated with stabilised microtubules.

Artificial Microtubule Organising Centres

Alternatively, asters can be formed using a microtubule organising centre (MTOC). In the cell, these are protein complexes which nucleate microtubule growth, thus forming a radial array as the microtubules grow away from the centre. Holy et al. (1997) created artificial MTOCs by polymerising short biotinylated microtubule seeds and binding them to streptavidin coated magnetic beads. With the addition of tubulin, microtubules polymerise away from the MTOC, forming an aster. Although growth occurs from both ends of the seeds, it occurs much faster from the plus end, thus all the longer microtubules in the aster are similarly orientated.

Spoerke et al. (2008) improved on the artificial MTOC method to create asters of either polarity. They also used biotinylated tubulin and streptavidin microspheres but with the addition of N-ethylmalemide (NEMS) tubu-

lin. Polymerising microtubules in the presence of NEMS tubulin has been shown to inhibit growth from the minus end Hyman et al. (1991). Thus by forming fluorescently labelled microtubules with NEMS tubulin and then adding biotinylated tubulin, segmented microtubules are formed with short biotinylated sections on the plus ends. When mixed with the streptavidin coated microspheres, asters are formed. Asters of the opposite polarity to this can be formed by polymerising short biotinylated seeds first and in the presence of NEMS tubulin and then adding fluorescently labelled tubulin.

1.4.3 Spools

Hess et al. (2005) demonstrated the assembly of spool shaped structures (shown in Figure 1.8) in the gliding geometry. Microtubules were polymerised from biotinylated tubulin. They were then placed onto a kinesin coated surface, as in the gliding assay but in the absence of ATP. A solution of fluorescently labelled streptavidin was added which bound to 50% of available biotins on each microtubule. When ATP was added, the microtubules glide over the surface. When a biotin on a microtubule meets a free steptavidin on another microtubule they can bind. This bond can be pulled apart by the motor protein (Hess et al. (2002)) or further bonds can be made along the length of the microtubule 'zipping' them together into a filament.

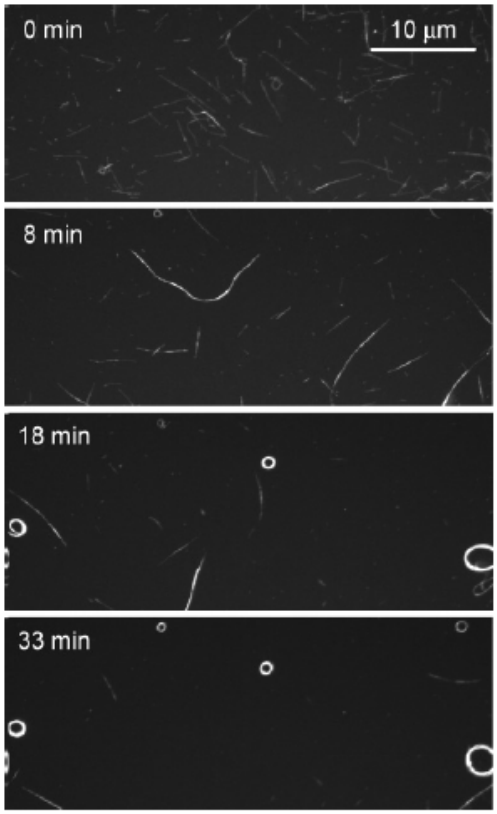

Figure 1.8: fluorescence micrographs of self-assembled spools using biotinylated microtubules cross-linked by streptavidin from Hess et al. (2005). By 8 minutes, filaments have formed which wrap up into spools by 18 minutes and become the dominant structure by 33 minutes.

Microtubules were parallel in all 'zipping' events observed, implying that the filaments are also aligned parallel. In some of these filaments the leading tip becomes bent, possibly through interaction with contaminants on the surface. The tip can bend back on itself and bind to the tail of the filament. In this way, spools are formed. Gliding filaments bind to spools, becoming caught and woven into the spool. These interactions lead to spools becoming the dominant structure as once a filament tip has bent back on itself and bound to the filament, it cannot unwind and subsequent filaments become trapped

in the spool. Figure 1.8 shows the time evolution of the spools system. By 8 minutes, filaments have formed which wrap up into spools by 18 minutes and become the dominant structure by 33 minutes.

1.4.4 Wires

The Hess et al. (2005) system for spool formation was re-tooled to form millimetre scale wires by Idan et al. (2012). Bundles are formed as transient structures before wrapping up into spools. Changing the motor velocity, through the ATP concentration, affected the bundle length. By tuning the other assembly parameters - steptavidin concentration, microtubule density and biotinilation and assembly time - the formation of bundles was optimised. ATP concentration was kept constant using an ATP regeneration system and found to be optimal at 20 μM. These bundles or wires were frequently over 0.5 mm in length and in one instance, almost a millimetre.

1.4.5 Active Bundles

Active bundles of microtubules that demonstrate cilia like beating have been demonstrated by Sanchez et al. (2011). They create motor clusters from biotinylated kinesins bound to a streptavidin. When these clusters are mixed with microtubules they form asters (Nédélec et al. (1997)) but with the ad-

dition of polyethylene glycol (PEG), oscillating bundles are formed. The PEG provides an attractive depletion force between the microtubules causing bundling. These bundles require an interface to form, such as the edge of the microscope coverslip or air bubbles. Away from these interfaces, microtubules are largely arranged in asters. These bundles were observed to oscillate in a manner similar to beating cilia. The frequency was determined by the length of the bundles which varied from 10-100μm with longer bundles beating slower. As well as individual bundles, they were able to observe emergent behaviour from multiple bundles. When the density was sufficient, the oscillating bundles interact producing metachronal waves similar to beating cilia.

1.5 Kinesin Nanotechnology

The kinesin-microtubule system has much to offer nanotechnology. The motor is nanoscale, highly efficient and capable of moving over a hundred times its own length. To use them, they must be harnessed and controlled. Broadly, systems fall into two categories, inverted and natural geometry. The inverted geometry makes use of the gliding assay with microtubules serving as shuttles to carry cargo. In the natural geometry, kinesin carries the cargo as it does in the cell. Several systems making use of both geometries are reviewed

here.

1.5.1 Inverted Geometry

There are a number of challenges associated with making use of the gliding assay or inverted geometry. If microtubules are to serve as shuttles, a means of attaching cargo to them is required by functionalising the microtubule. This cargo must be loaded onto the microtubule and unloaded at a specific destination. In the gliding assay, microtubules glide in random directions so some means of controlling the direction of travel is needed and possibly a way to stop moving shuttles. A number of different strategies have been employed to tackle these problems and devices have been built which use microtubule shuttles, including a smart dust biosensor (Fischer et al. (2009)).

Functionalised Microtubules

In order to attach cargo, or even just to visualise microtubules, it is often necessary to chemically functionalise them (Malcos and Hancock (2011)). The first molecules to be chemically linked to microtubules were fluorophores, with fluorescein being the first. It was linked using dichlorotriazinyl fluorescein (Keith et al. (1981)). As this fluorophore photo-bleaches easily, rhodamine is now more commonly used - linked using the succinimidyl ester form (Malcos and Hancock (2011)). To make functionalised tubulin, pre-formed

microtubules are functionalised and then depolymerised so that functionalisation does not interfere with polymerisation. Fluorescent labelling allows for fluorescence microscopy visualisation of *in vivo* and *in vitro* microtubules.

For nanotechnology purposes, general attachment of molecules to microtubules is often required. This is usually done with the streptavidin protein which binds strongly to biotin. Microtubules can be biotinylated by reacting biotin-XX succinimidyl ester with polymerised tubulin (Hyman et al. (1991)). The XX denotes a linker to increase the availability of biotin to streptavidin. This allows many different cargoes to be attached to microtubules including streptavidin coated nanospheres (Fischer et al. (2009)), biotinylated single stranded DNA (Schmidt and Vogel (2010)) and antibodies (Fischer et al. (2009)).

It is also possible to covalently link cargo to microtubules using chemical cross-linkers and this has been used to attach DNA directly. Hiyama et al. (2009) reacted microtubules with the cross-linker, Sulfo-GMBS (N-[γ-maleimidobutyryloxy]succinimide) ester, which reacts with thiolated single stranded DNA. Future functionalisations may make use of post translational modifications (PTMs) or recombinant tubulin. Cellular microtubules often have PTMs and it is thought that these govern interactions with microtubule associated proteins (MAPs) (Hammond et al. (2008)). Recombinant tubulin

would allow expression of already modified tubulin proteins by genetic modification. Alpha and Beta tubulin have now been successfully purified from yeast (Drummond et al. (2011)) so synthetic systems may soon make use of recombinant tubulin.

Cargo Loading and Unloading

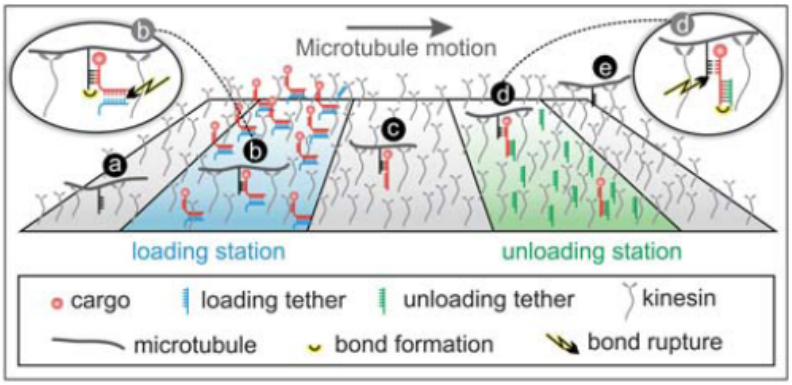

Figure 1.9: Schematic of microtubule molecular shuttle loading and unloading sites from Schmidt and Vogel (2010). **a** A gliding microtubule shuttle. **b** The shuttle picks up cargo. **c** Cargo is transported to the unloading site. **d** Cargo is unloaded. **e** shuttle leaves the unloading site.

Microtubule molecular shuttles have been loaded and unloaded with cargo by Schmidt and Vogel (2010), using DNA as a programmable linker (see Figure 1.9). Microtubules were functionalised with DNA using biotinylated tubulin and DNA - linking them via a streptavidin. The cargo was a gold nanoparticle functionalised with single stranded DNA. Shuttles glide on a kinesin coated surface micro-printed with loading and unloading stations. The loading station was made by evaporating a thin gold film. Thiol modified

single stranded DNA with a region complementary to the cargo's DNA was attached to the gold film. The unloading station was made by micro-contact printing streptavidin and attaching biotinylated single stranded DNA with a region complementary to the cargo.

Figure 1.9 shows a microtubule gliding, picking up cargo and depositing it at an unloading station. Cargo is bound to the loading station in a 'zipper' geometry with a 30 base pair (bp) overlap (Figure 1.9 **b**). The microtubule DNA only contains a 20bp complementary region but because the 'zipper' geometry requires much less force to break than trying to break all the base pairs at once, the shuttle strips the cargo from the loading station. Cargo is transported (Figure 1.9 **c**) to the unloading station where it binds to the unloading DNA in a shearing conformation with 30bp (Figure 1.9 **d**). This time the moving microtubule pulls its DNA off the cargo, leaving it at the unloading station.

Guiding Microtubule Shuttles

Gliding microtubules can be guided by patterning the kinesin surface. Dennis et al. (1999) adsorbed kinesin onto ridged films of poly(tetrafluoroethylene) (PTFE). The ridged film was created by simply rubbing a block of PTFE across the surface of a coverslip. Deposited PTFE molecules are stretched

and aligned along the shear direction. The ridges had a random height distribution of 1-30nm and were also spaced randomly 10-1000nm apart. The surface was coated in casein solution before kinesin was added to prevent kinesin denaturation on the surface. Kinesin surface concentrations of 0.5 μg/ml (low), 3 μg/ml (medium) and 18 μg/ml (high) were tested. It was found that at medium concentration, microtubule trajectories aligned with the surface polymer but at low and high concentrations, orthogonal trajectories were observed. They theorise that at low concentration, some microtubules are only bound by one kinesin and can thus swivel (Hunt and Howard (1993)). At high concentration there are not sufficient gaps between tracks and microtubules can move perpendicularly.

Although using polymers to pattern the surface aligns the microtubule motion, it does not control the direction and microtubules can fall off the track. Hiratsuka et al. (2001) developed channels using photolithography which restrict microtubules to a specific track and rectify microtubule motion. Unlike previous patterned surfaces (Dennis et al. (1999)), the kinesin tracks were in depressed channels. When microtubules struck the walls, they either bounced off or more often, moved along the wall. By using an arrowhead motif in the channel shape, microtubule gliding was rectified along the direction of the arrow (see Figure 1.10). A circular track was created with several arrowheads at regular intervals. Figure 1.10 shows the track

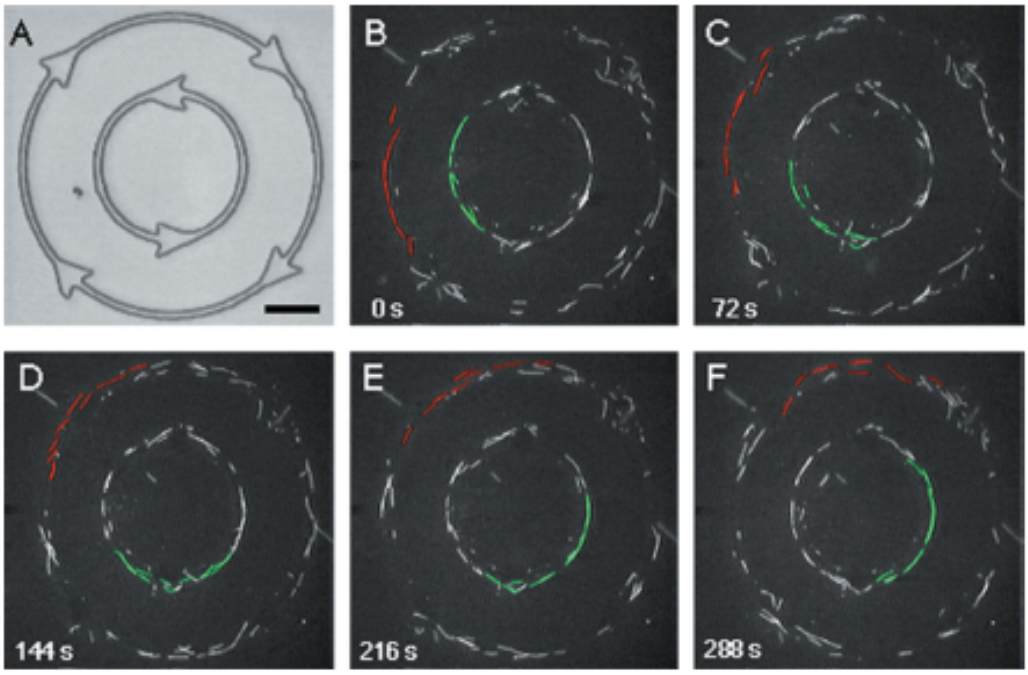

Figure 1.10: Light microscopy of the arrowhead track design in A and a time series of fluorescence micrographs of rectified gliding microtubules from Hiratsuka et al. (2001). Scale bar 20μm.

geometry and a time series of microtubules moving directionally. The outer microtubules are moving clockwise and the inner are moving counter clockwise. An asymmetric track design utilising arrowheads was also created which trapped microtubules into the left half of the chamber.

Microtubules have also been guided by braking. Korten et al. (2012) have used a thermally responsive polymer to selectively stop and restart gliding microtubule populations. Microtubules were functionalised with poly(N-isopropylacrylamide) (PNIPAM). This polymer has a lower critical solution temperature (LCST) of about 32 - 33° C. Above this temperature the polymer forms a complex, dehydrated structure but below it, the polymer extends

by hydration. The polymer was biotinylated and attached to biotinylated microtubules via a streptavidin. A gliding assay was performed with these microtubules with the temperature oscillating between 35°C and 20°C every 2 minutes. At 35°C microtubules remained bound to the surface and did not glide. When the temperature was decreased to 20°C, microtubules moved across the surface and stopped again after the temperature increased. They propose a mechanism to explain their data based on surface interaction of microtubule bound streptavidin. When the polymer is extended, streptavidin does not interact with the surface and the microtubule glides but when the polymer is compact, the streptavidin binds to the surface and inhibits gliding. In this way microtubule shuttle gliding is controlled by temperature.

Smart Dust Biosensor

The available control over the inverted geometry has been employed to power a smart dust biosensor (Fischer et al. (2009)). These are devices designed to monitor an environment and detect specific analytes. Here transport replaces the wash step in a double antibody sandwich assay. Streptavidin was used as a test analyte. biotinylated microtubules were set gliding on a kinesin surface in a circular chamber with overhangs at the edges and in the presence of biotinylated fluorescent nanospheres, used as an optical tag. When the analyte is present, it is captured by the microtubule shut-

tles, transported from the detection region and labelled with the optical tag. The shuttles transport the nanospheres to the edge of the chamber where they stick due to the overhangs. Without the analyte, nanospheres are not deposited. Glutathione-S-transferase (GST) was also used as an analyte by using commercially available GST antibodies, one biotinylated and the other conjugated to a quantum dot. The biotinylated antibody was conjugated to the microtubules via streptavidin to detect the analyte and the quantum dot conjugated antibody served as the optical tag. This system represents a significant step forward incorporating kinesin and microtubules into useful devices.

1.5.2 Natural Geometry

There are fewer examples of systems making use of the natural geometry. In the inverted geometry, with a high enough motor density, the microtubule shuttles remain almost permanently bound to the surface but in the natural geometry, it is difficult to stop kinesin shuttles from disassociating. Natural systems, found in biology, demonstrate what can be achieved with this geometry and there have been some systems which exploit it.

Nanoharvesters

Nanoharvesters have been created which can perform the function of the microtubule shuttles in the smart dust biosensor. Carroll-Portillo et al. (2009) used quantum dots conjugated to antibodies for tumour necrosis factor-α (TNF-α) and kinesin. These nanoharvesters can travel along microtubules and pick up their analyte. Their ability to do so was tested with a double antibody sandwich assay using another TNF-α attached to a quantum dot of a different colour. The nanoharvesters were found to capture analyte and move well but with some inhibition owing to the relative sizes of the antibodies and the kinesin.

Organised microtubule tracks

Much of the difficulty in using the natural geometry could be overcome by using organised microtubule tracks (Goel and Vogel (2008)). Doot et al. (2007) have used micro-patterned channels in the inverted geometry to create a network of tracks for single kinesin teams. A pinwheel shaped channel with overhangs was micro-fabricated and coated with kinesin. Rhodamine labelled microtubule seeds were set gliding in the channel. The shape of the channel causes one direction of microtubule travel to be much more likely (see Figure 1.5.1). The seeds are much more likely to enter one of the arms

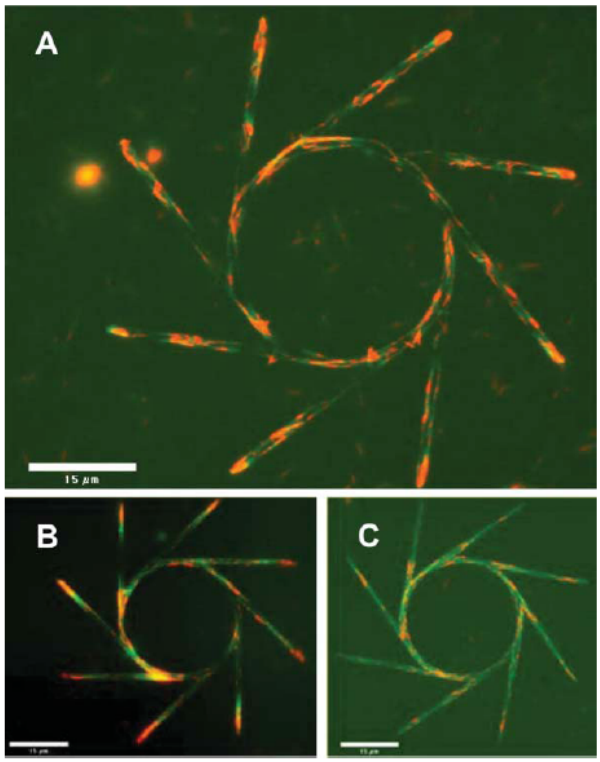

Figure 1.11: Aligned microtubule pinwheel from Doot et al. (2007) Rhodamine seeds are in red and fluorescein tubulin in green. A shows a 5 minute, 1.8μM fluorescein tubulin exposure; B a 10 minute 3.6μM exposure and C a 15 minute 3.6μM exposure.

of the pinwheel, than to leave it. The overhang in the channel also stops seeds from climbing the walls. Thus seeds are similarly orientated around the pinwheel. Florescein labelled tubulin was polymerised from these seeds, created a network in the shape of the pinwheel. Figure 1.11 shows the effects of florescein tubulin concentration and exposure time on network formation. With a dilute solution of gluteraldehyde,the network can be cross-linked with the kinesin surface,to immobilise the network, but not so much that further transport cannot be sustained. Uni-directional transport of kinesin coated

nanospheres was demonstrated on the network with 80% of observed moving cargo travelling in the intended direction. Creating this track network using top-down methods is challenging. A more facile method for creating organised tracks is to use, as nature does, self-organisation.

Theoretical devices

Bouchard et al. (2006) describe possible uses of self-organised microtubules in a device. They demonstrate some simulations using plus and minus ended motors combined with dynamically unstable microtubules and MTOCs. A sorting machine is described where two different cargoes are attached to the two different motors. Microtubules nucleate from the MTOC and an aster forms. the minus ended motors move along the microtubules into the centre of the aster, concentrating this cargo, while the plus ended motors are repelled from the centre, relegating the cargo to the periphery. A synthetic melanophore is also described. In this scheme each cargo is attached to both a plus and minus ended motor and each motor can be inhibited by a signal. Initially the cargo is dispersed and the plus ended motors are inhibited. If the cargo is pigment, as in the melanophore, then the system is in the opaque state. Asters form from microtubules nucleated on the MTOC and the cargo concentrates in the centre through the minus ended motors. This leaves most of the system transparent. The cargo can be re-dispersed by activating the

plus ended motor through a signal, returning the synthetic melanophore to an opaque state.

1.6 DNA and DNA nanotechnology

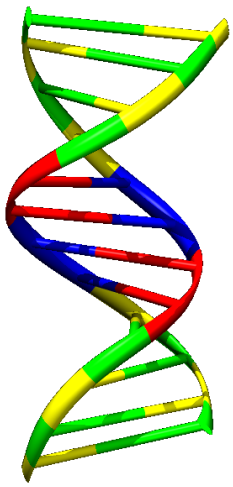

Figure 1.12: Crystal structure of a DNA double helix from Narayana and Weiss (2009). A and T in red and blue. C and G in yellow and green.

In Schmidt and Vogel (2010) DNA was used to address specific cargo to a nanoshuttle. The potential for other uses of DNA in such systems is enormous. DNA is the information carrying molecule for the cell. This information is stored as a code using 4 building blocks A,G,T,C: Adenosine, Guanine, Thymine and Cytosine. These blocks are complementary to each other, A binds to T and C binds to G. Template directed DNA polymerisation produces two complementary strands, twisted into a double helix (Figure

1.12). The cell uses the information encoded in the sequence of bases to create proteins. Encoded sequences of bases can also be used, *in vitro*, to specify interactions between strands. This programmability of interaction allows the creation of DNA structures formed from many interacting single strands of DNA, making DNA an excellent material for building on the nanoscale.

Early proposed DNA nanostructures were tile based. Seeman (1982) proposed a four arm DNA junction with single stranded 'sticky-ends'. Tile based designs led to the construction of μm sized two-dimensional arrays (Winfree et al. (1998)). Three dimensional structures were also made in the form of DNA polyhedra. Goodman et al. (2005) built a DNA cage in the shape of a tetrahedron capable of containing a cargo such as a drug, which could be released in response to a signal. The range of possible structures was vastly increased by the invention of DNA origami by Rothemund (2006). He used a series of short strands of single stranded DNA, called staple strands, to fold up a long strand of the bacteria-phage, m13's genome, the scaffold strand. This technique has been used to make geometric shapes and even smiley faces. DNA origami was extended into 3 dimensions by Douglas et al. (2009) allowing the creation of open-able boxes (Andersen et al. (2009)) among many other designs. It has even been possible to completely remove the scaffold strand and assemble 2D and 3D structures from single stranded DNA tiles

(Wei et al. (2012); Ke et al. (2012)).

1.6.1 Active DNA devices

Figure 1.13: Schematic illustrating a strand displacement reaction. The blue duplex has a dark blue overhang called a toehold. The red strand is fully complementary to the dark blue strand and so binds to the exposed toehold. This strand competes with the light blue strand for the dark blue and eventually fully displaces it to reach the lowest energy conformation.

Not only static structures can be made from DNA, but active machines. Various devices have been constructed from DNA (Yurke et al. (2000); Qian et al. (2011)) including molecular motors inspired by stepping motors like kinesin (Green et al. (2008); Wickham et al. (2011)). One of the crucial mechanisms which these machines use for operation is called toehold mediated strand displacement (Yurke et al. (2003)). This mechanisms is illustrated in Figure 1.13. The blue duplex contains a single stranded overhang called a toehold. This unbound region can bind to an invading strand (red) which competes with the light blue strand for the dark blue strand. Unpaired bases have higher free energy than paired so to a good approximation the system reaches equilibrium when the minimum number of unpaired bases is reached. The red strand thus strips the light blue strand from the dark blue.

1.7 Combining DNA and molecular motors

The work presented in the next chapters uses the structures, dynamic interactions and the information carrying properties of DNA, combined with the properties of kinesin for nanotechnology and to create novel motor complexes to better understand kinesin itself. DNA has been used with kinesin (Schmidt and Vogel (2010); Derr et al. (2012); Furuta et al. (2012)) but mostly as a simple linker. Much more can be achieved. The next chapters demonstrate how DNA can be used to control self-organisation reactions of kinesin and microtubules to build a track architecture for molecular transport. The kinesin natural geometry has been under used because of the difficulty building track architectures. Those track systems that have been created (Doot et al. (2007)) required top down construction rather than utilising the range of self-organised microtubule structures *in vivo* (Rogers et al. (2002); Tuma et al. (1998)) and *in vitro* (Nédélec et al. (1997); Hess et al. (2005)).

In Chapter 2 a DNA-kinesin hybrid is demonstrated. This hybrid is used as a component of a novel construct similar to the Eg5 kinesin in nature (Subramanian and Kapoor (2012) which is capable of self-organising microtubules into radial asters. Methods are developed to use asters as a platform for transport and in Chapter 3 a shuttle is demonstrated using the DNA-kinesin hybrid. These shuttles are used for molecular transport of cargo

but also to transport DNA encoded signals which control the distribution of cargo on the microtubule architectures. It is shown in Chapter 4 that shuttle transported signals can be made to interact with the self-organisation process itself, adding a DNA-encoded disassembly signal which can destroy asters.

Shuttles are studied at the single molecule level in Chapter 5 and then re-purposed to study the motor itself. DNA architectures can be used to link many motors together in defined geometries (Derr et al. (2012); Diehl et al. (2006); Furuta et al. (2012)). Shuttles were designed to link teams of single kinesin heads together, study their behaviour and understand the minimal motor unit of kinesin.

Chapter 2

Asters as a platform for transport

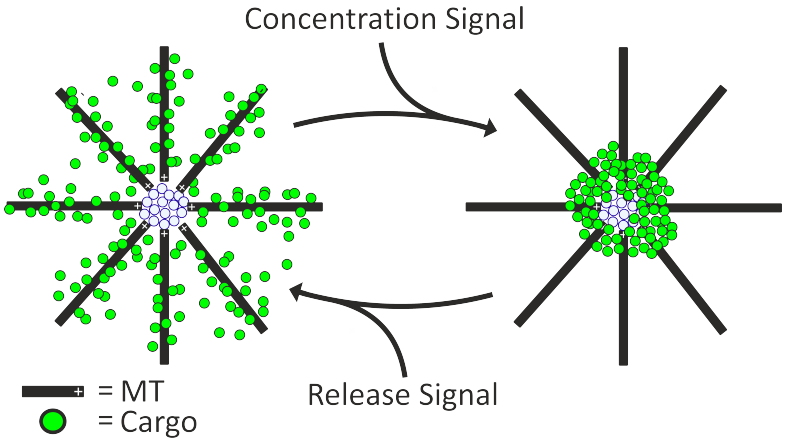

Figure 2.1: Schematic illustrating using signals to control the distribution of cargo on an aster.

The aim of the work presented in this and the next two chapters is to

create a molecular transport system similar to the cytoskeleton in eukaryotes. This system would use kinesin to self organise microtubules into radial asters similar to the interphase array. Asters would serve as a track network for other kinesins to transport cargo (illustrated in Figure 2.1). As in eukaryotes, molecular signals would control the transport of cargo and even re-configure the track network itself. The programmability of DNA interactions allows this to be realised.

DNA nanotechnology can be used in two ways to realise the molecular transport system. Firstly, DNA nanostructures allow the specification of the geometry of multiple attached kinesins, allowing teams of motors to possess new properties and functionality - specifically, simultaneous interaction with multiple microtubules. This enables kinesin to self-organise microtubules into asters. Secondly, programmable DNA interactions allow the encoding of signals which can interact with other DNA nanostructures and allow the system to be controlled.

This chapter outlines linking DNA and kinesin, forming and observing asters, as well as the practicalities of adding cargo and signals to asters whilst observing their effects. A kinesin zinc finger fusion is described which binds a specific sequence of DNA. Once fused with a DNA nanostructure, these assemblers can organise asters from microtubules in the presence of

ATP. Asters are characterised and methods for adding cargo and signals to them while imaging with fluorescence microscopy are developed.

The kinesin zinc finger fusions were designed by Dr Junichiro Yajima at the MCRI. Proteins were purified with help from Dr Helen Carstairs, Dr Carlos Sanchez-Cano and Dr Maria Alonso at MCRI and CMCB. The gliding assay protocol was developed by Dr Helen Carstairs. Flow chambers were designed with input from Dr Carlos Sanchez-Cano.

2.1 Kinesin-DNA binding

A zinc finger kinesin fusion protein was created to link DNA and kinesin. Two other DNA-protein attachment strategies were investigated and are included in Appendix A Section A.1. These included modifying DNA with a tris-NTA motif, which would bind the his-tag on the kinesin, and using a chemical cross-linker (Sulfo-SMCC) to bind thiolated DNA to a single exposed cysteine residue on a mutant kinesin.

2.1.1 Zinc-Finger

Zinc fingers are small protein motifs capable of binding specific sequences of DNA, requiring zinc ions to fold. Yajima and Cross (2005) fused an sp1 zinc finger to kinesin. Dr Junichiro Yajima improved this using a stronger binding

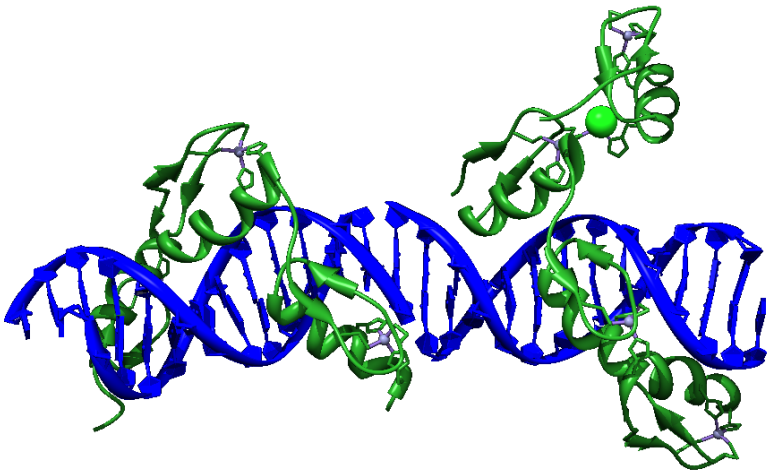

Figure 2.2: Crystal structure of the zinc finger protein bound to a DNA duplex shown in two orientations. DNA in blue and zinc finger protein in green from Kim and Berg (1996).

zinc finger protein (Carstairs (2008)). A designer peptide from Papworth et al. (2003) containing three zinc fingers was fused to kinesin. It binds to a specific 9 base pair sequence of DNA with a high affinity (1nM). Figure 2.2 shows two orientations of a similar zinc finger protein from Kim and Berg (1996). The DNA is shown in blue, the protein in green and the zinc ions in purple. The advantage of this attachment strategy is that no chemical modification of the DNA or protein is required although the binding is not as strong as covalent binding.

2.2 Kinesin Construct

The kinesin construct was designed by Dr Junichiro Yajima starting with wild type dimeric rat kinesin 1 truncated to the first 430 amino acids. This

contains the head, neck linker and enough of the coiled coil to dimerise. The A1 zinc finger from Papworth et al. (2003) was added with five glycine residues between the neck and zinc finger to improve protein solubility. This flexible region allows separation between kinesin and zinc finger chains as the protein folds. Six histidines, a his-tag, were included on the protein for metal affinity purification.

This kinesin construct has two zinc fingers and the potential to bind to two binding sites on the DNA. The two zinc fingers are ∼1nm apart (by examining the crystal structure (Kozielski et al. (1997))) and also oppositely orientated by symmetry. It would be very difficult for the protein to bind to two sites on the same DNA as they would have to be very close together and oppositely orientated. Binding to two DNA molecules at once is also difficult as the DNA would be held very close together, below the Debye screening distance. The zinc finger binding is sufficiently weak that an excess of protein was used making binding to multiple DNA molecules more unlikely. Gel electrophoresis shown in Figure 2.10b shows that only one zinc finger per kinesin can bind to a DNA binding site.

2.2.1 Protein Purification

A full protocol for expressing and purifying the protein is described in Appendix A Section A.2: a brief outline is given here. The plasmids for the kinesin proteins used were created by Dr Junichiro Yajima. The plasmid for the desired protein was transfected into *E. coli* and grown into ∼8l starting material. These cells were collected by centrifugation and lysed open by sonication and Lysol. After further centrifugation to remove cell fragments, the supernatant was incubated with cobalt beads for metal affinity purification. The his tag on the protein binds to the metal beads and can then be displaced by imidazole. The bead protein mixture was loaded onto a column in a fast protein liquid chromatography (FPLC) system and buffer pumped through to remove anything not bound to the beads. Fractions were collected as an imidazole gradient was run and then ran on a denaturing gel. After the protein was identified on the gel, fractions containing it were pooled and concentrated using dialysis. The purified protein was aliquoted and flash frozen, ready for use.

2.3 DNA

A variety of different DNA nanostructures were used but an outline of general design and experimental techniques is given here. The sequences of all

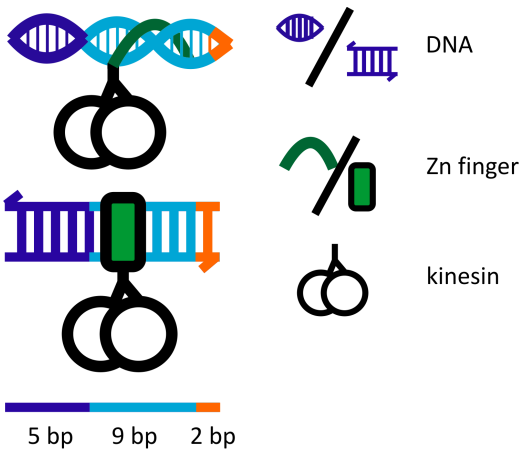

Figure 2.3: Schematic of the zinc finger DNA

DNA used are in Appendix B. DNA sequences were designed using the Nupack software (Zadeh et al. (2010)) to generate sequences based on design constraints. The software was also used to carefully analyse different combinations of strands to check they interacted in the desired way. Zinc finger constructs contained the 9 base pair binding sequence and then 2 bases either side as a spacer. Adding the spacer creates an 11 base pairs for each zinc finger sequence, close to the DNA helicity of 10.5 base pairs per turn (Drew and Wing (1981)). At least five bases were included at both ends for stability. Figure 2.3 shows a schematic of the zinc finger DNA. The full protocols for creating DNA nanostructures are in Appendix A Section A.5 and all DNA sequences used are in Appendix B. Synthetic DNA was purchased from IDT. Single strands were ordered and then mixed, in salt containing buffer solutions, to form desired structures. DNA nanostructures were formed by

heating to 95°C and cooling over 30 minutes. Zinc finger kinesin was bound to DNA nanostructures containing the binding sequence by mixing them in zinc containing buffer and incubating for 30 minutes.

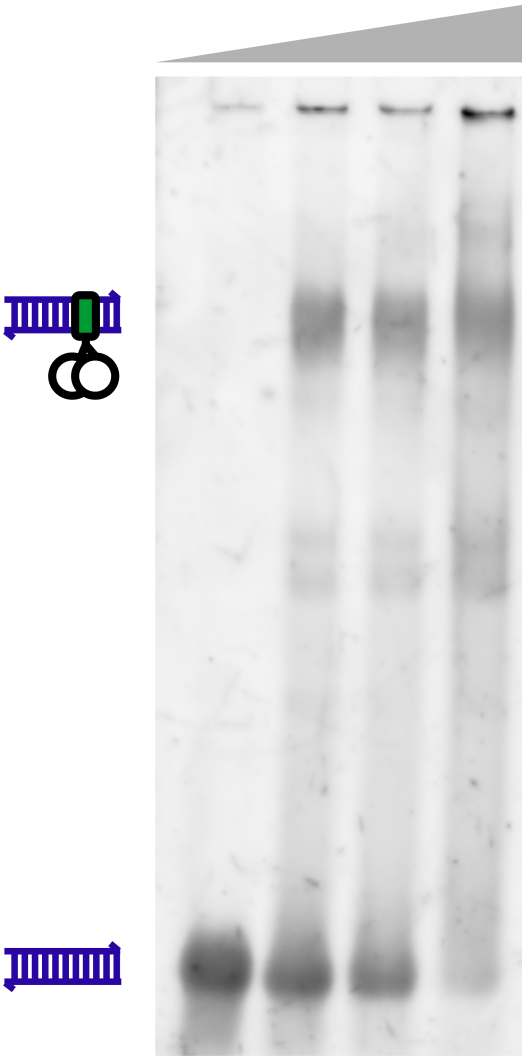

Figure 2.4: Native polyacrylamide gel stained with SYBR^{TM}Gold containing samples of DNA with one zinc finger binding site (0.25μM) and different concentrations of zinc finger kinesin (0μM, 0.25μM ,0.5μM, 0.75μM)

Binding of zinc finger kinesin to DNA nanostructures was tested us-

ing native polyacrylamide gel electrophoresis (PAGE), the full protocol is in Appendix A Section A.6.1. DNA has a highly charged backbone so is pulled through the polyacrylamide gel matrix by an applied electric field. Bound protein increases the size of the complex and decreases its mobility through the gel. Figure 2.4 shows a native polyacrylamide gel stained with SYBR^{TM}Gold containing samples of DNA with one zinc finger binding site (0.25μM) and different concentrations of zinc finger kinesin (0μM, 0.25μM ,0.5μM, 0.75μM). The DNA only band decreases in intensity with increasing protein concentration while the kinesin-DNA band increases. Around a three times excess of protein was required for acceptable DNA binding.

2.4 Microtubules

Microtubules were polymerised from solutions of free tubulin protein, which were either obtained commercially (Cytoskeleton^{TM}) or purified by collaborators, formerly at the Marie Curie Research Centre (Oxted, Surrey) and now at the Centre for Chemo-Mechanical Cell Biology, University of Warwick. Tubulin is present in high concentration in the brains of cows and pigs and can be purified from fresh brain matter by cycles of polymerisation, centrifugation and de-polymerisation. Tubulin solutions were flash frozen and stored in liquid nitrogen. The full protocol for microtubule formation is in

Appendix A Section A.4. Microtubules were polymerised from these solutions by adding GTP and $MgCl_2$, required to catalyse GTP hydrolysis, and incubating at 37°C for 30 minutes to form microtubule seeds. With the addition of taxol, further polymerisation occurs from these seeds overnight at room temperature. Taxol microtubules remain stable for up to a week although they become progressively longer through a process of end-end joining.

2.5 Fluorescence Microscopy

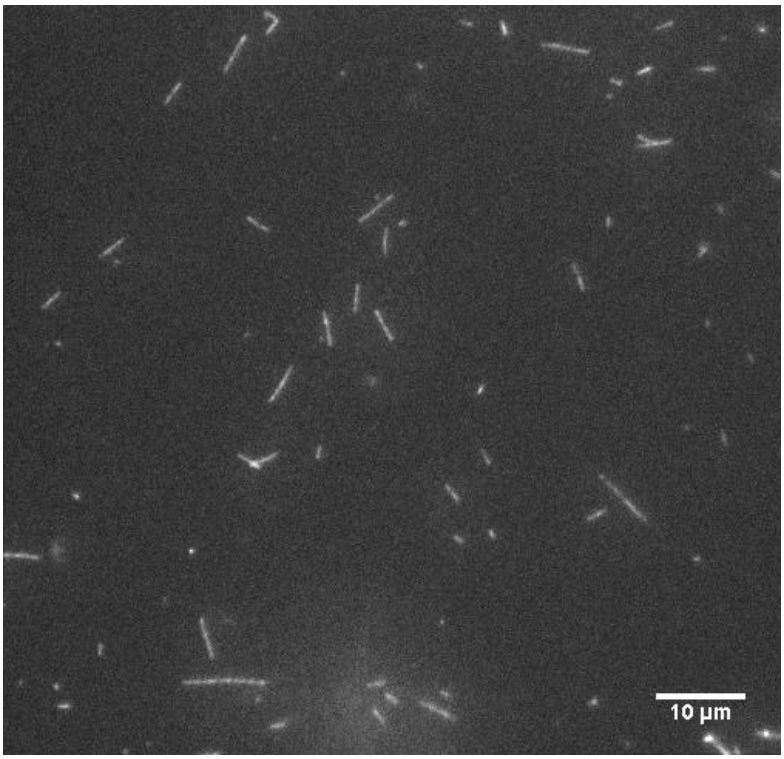

Figure 2.5: Fluorescence micrograph of Rhodamine labelled microtubules. Scale bar 10 μm.

Microtubules were imaged using fluorescence microscopy. Tubulin la-

belled with fluorophores, Rhodamine of Hylite 647 (Cytoskeleton^{TM}), was mixed with unlabelled tubulin and polymerised creating speckled microtubules. A standard inverted microscope (Olympus, IX71) with a 60x (NA 1.6) or 100x (NA 1.45) oil immersion objective with a 50μm or 85μm field of view was used. Figure 2.5 shows a fluorescence micrograph of Rhodamine labelled microtubules. Illumination can cause photo-damage so an oxygen scavenging system of glucose oxidase, D-glucose and catalase was used. These were diluted in an imaging buffer, used for in all microscopy experiments. This buffer also contained an ATP regeneration system of creatine kinase and creatine phosphate. Taxol was added to keep microtubules from depolymerising and bovine serum albumin to stop unwanted aggregation of proteins. ATP was added, as required at saturating concentration of 4mM (Howard et al. (1989)).

2.5.1 Simple Flow Chamber

Basic fluorescence imaging was carried out using a simple flow chamber. A 25x50mm glass coverslip (Matsunami) was used as the bottom of the chamber. Two strips of parafilm were placed on top of the coverslip to create a channel and then a 22x22mm coverslip placed on top to cover the chamber. The flow chamber was heated to 50°C which partially melts the parafilm and

allows the flow chamber to be sealed by gently pressing the two coverslips together. These chambers had a volume of 7μl.

2.6 Gliding assays

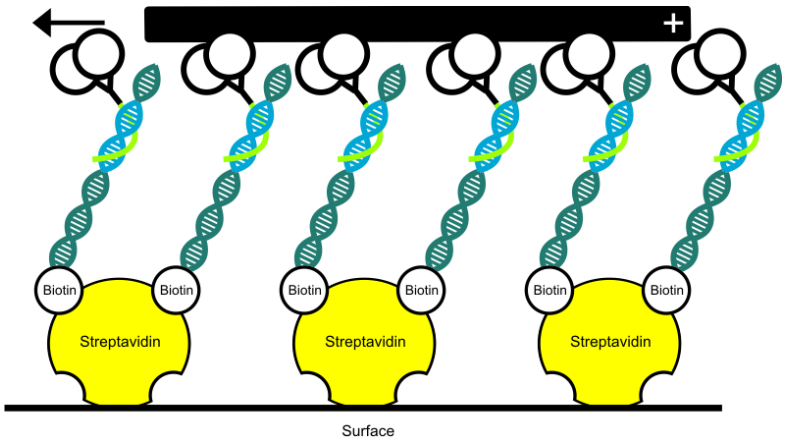

Figure 2.6: Schematic illustrating the geometry of a gliding assay. streptavidin in yellow, biotin in white, kinesin as two black circles with a green zinc finger, microtubule as black rod with the plus end labelled. The DNA is in blue with the zinc finger site in light blue. Direction of microtubule travel marked with an arrow.

A key experimental technique for studying kinesin has been the gliding assay, first used by Vale et al. (1985). A microscope slide is coated with kinesin such that the motor domain faces away from the surface. This can either be done with a specific attachment strategy such as biotin-streptavidin or by non-specific binding as some kinesin constructs will attach naturally to the surface in the correct orientation. A solution containing microtubules and ATP is then added. Microtubules can be imaged either directly, through differential interference contrast (DIC) microscopy, bright field (with back-

ground subtraction and image averaging, see Gutierrez-Medina and Block (2010)) or by fluorescent labelling. Microtubules glide with a velocity dependent on the motor, temperature and ATP concentration. The saturating ATP concentration at which ATP binding is not rate limiting has been measured at 4mM (Howard et al. (1989)). At room temperature with kinesin 1, microtubules glide at 800nm/s (Howard (1996)).

Gliding velocity is normally found to be independent of motor surface density (Howard et al. (1989)) but in a study by Bieling et al. (2008) a density dependence was observed. Using a kinesin dimer construct truncated at the 612th amino acid, Bieling et al. (2008) observed a decrease in velocity at >1000motors/μ m^2. This slow down occurred at lower densities for a construct truncated at the 401st amino acid and very long microtubules (>25μm) were observed to move more slowly at intermediate densities. This indicates that the total number of motors interacting with the microtubule is the important factor. The density effect was more pronounced when the buffer ionic strength was decreased, increasing the microtubule affinity of the motors (Thorn et al. (2000)). They attribute the slow down to mechanical coupling between motors.

Kinesin-DNA motility was tested using a gliding assay (full protocol in Appendix A Section A.9). A biotinylated duplex of DNA containing the

zinc finger binding site at one end was coupled to the kinesin-zinc finger fusion. This duplex contained 9 base pair zinc finger sequence and 36 base pair linker before the biotin. An extra 5 base pairs were also included after the zinc finger to stabilise the end. The full sequence of the biotinylated strand is in Appendix B B.1.1. Two chamber volumes (7μl) of streptavidin were pipetted into the simple flow chamber allowing streptavidin to bind non-specifically to the surface. Parts of the surface uncovered by streptavidin were blocked by flowing in a solution of bovine serum albumin (BSA). The kinesin-DNA solution was added and bound to the streptavidin. The surface was further blocked with BSA to prevent non-specific interactions with the surface before adding a solution of fluorescently labelled microtubules. The gliding assay geometry is illustrated in Figure 2.6. With the addition of the ATP containing imaging buffer, microtubules were observed gliding along the surface of the chamber. Moving microtubules could be tracked using the Retrac program (as used in Crevel et al. (1997)). This software allows the user to define the microtubule end in each frame, manually tracking its trajectory. Microtubules were observed to glide on the kinesin-DNA construct at 0.570$\pm$0.066μm/s ($\pm$standard deviation) at room temperature and saturating ATP concentration.

2.7 Assembler design

DNA-kinesin hybrid nanostructures were designed to form asters using DNA-kinesin hybrids. To form asters, kinesin-DNA constructs must be able to cross-link microtubules (Nédélec et al. (1997)). In initial experiments, streptavidin was used to link DNA-kinesin together in an aster forming construct similar to Nédélec et al. (1997). In later experiments an all DNA nanostructure was used.

2.7.1 Aster Formation

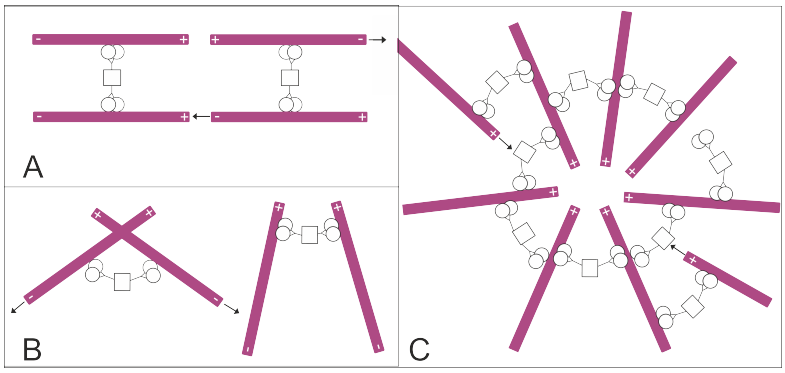

Figure 2.7: Schematic illustrating the formation of asters. Microtubules are in purple with ends labelled. Kinesin dimers are represented as two circles and joined together by a rectangular linker. **A** anti-parallel microtubules are slid apart by motor teams while aligned microtubules are held together. **B** Microtubules are sorted and teams wait at the microtubule ends. **C** The action of many motor teams organises the microtubules into asters. Teams are shown sliding microtubules into the aster.

The aster formation process is illustrated in Figure 2.7. To form asters, motor teams must be capable of cross-linking microtubules, binding to more than one at a time. Aster forming constructs must therefore have multiple motor domains orientated such that they are more likely to bind to two (or

more) microtubules. As motors only walk towards one end of the microtubule, cross-linking motor teams sort microtubules by polarity, as shown in Figure 2.7 panel **A**. Anti-parallel microtubules are slid apart whilst parallel microtubules are held together. Surrey et al. (2001) found this sliding mechanism to be crucial for aster formation. Simulations run by Nédélec and Surrey (2001), found that motor teams must also wait at the ends of microtubules before dropping off, in order for asters to form. The action of many such motor teams leads to the formation of asters illustrated in Figure 2.7 panel B and C.

Different motors and cross-linkers have been shown to form asters. Streptavidin linked biotinylated kinesin 1 was used in Nédélec et al. (1997) and antibody linked, glutathione-S-transferase non-claret disjunctional (GST-Ncd) kinesin, a negative ended motor, was used in Surrey et al. (2001). The microtubule orientation in asters was experimentally determined by Surrey et al. (2001) using polarity marked microtubules. When plus ended motors were used, like kinesin 1, microtubule plus ends were in the centre but when Ncd was used, minus ends were in the centre. The motor density distribution was found theoretically and experimentally, by Nédélec et al. (2001) to be exponential, reducing from the centre. They also measured the number of microtubules in an aster in quasi-2D geometry (a 9 μm thick chamber). They

found asters ranged in the number of microtubules involved from ∼300-1000.

2.7.2 Streptavidin Assembler

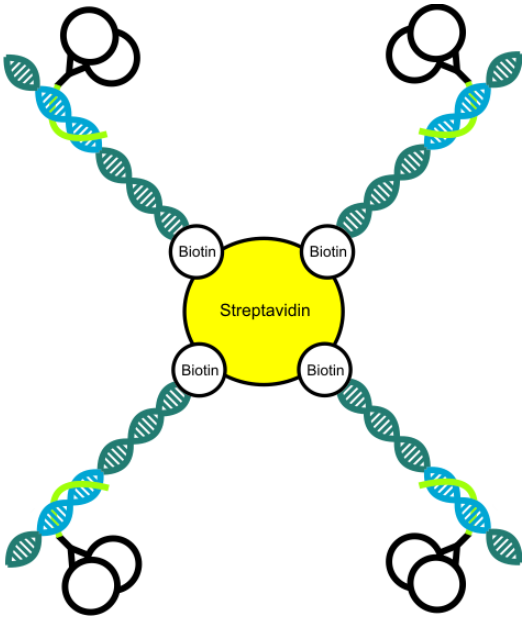

Figure 2.8: Schematic illustrating the streptavidin construct. streptavidin in yellow, biotin in white, kinesin as two black circles with a green zinc finger, microtubule as black rod with the plus end labelled. The DNA is in blue with the zinc finger site in light blue.

In order to replicate the work in Nédélec et al. (1997), a streptavidin based construct was designed. Nédélec et al. (1997) used biotinylated kinesin and streptavidin to create a tetrameric construct which could organise microtubules into asters. A very similar construct was created but with biotinylated DNA linking the kinesin to the streptavidin. A schematic of the construct is shown in Figure 2.8. The biotinylated DNA strand used for gliding assays was bound to kinesin and streptavidin to form a tetramer. This

construct was found to readily organise asters when mixed with microtubules and ATP after ∼10 minutes. Figure 2.9 shows a fluorescence micrograph of an aster formed using this construct.

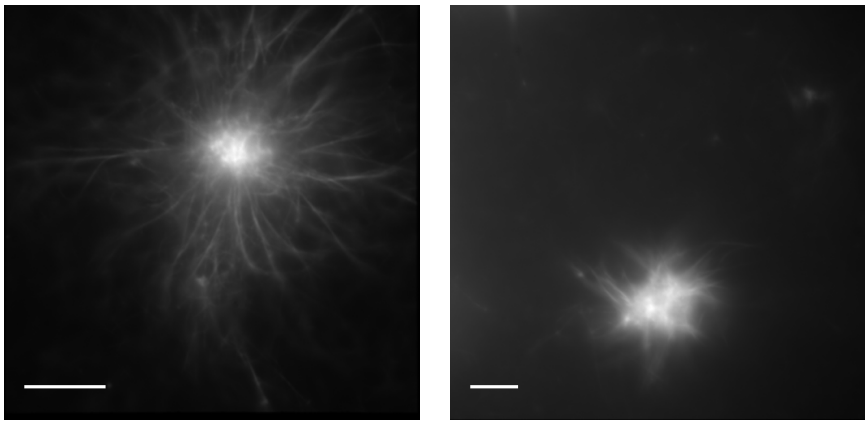

Figure 2.9: fluorescence micrographs of asters formed using the DNA-streptavidin assembler (left) and the DNA assembler (right). Scale Bar 10μm.

2.7.3 DNA Assembler

A minimal DNA based aster forming construct was created. Using a DNA nanostructure to link motors in the assembler allows better control over motor geometry and adds the possibility of controlling the assembler through DNA signals. A DNA nanostructure containing two 9 base pair zinc finger binding sites on a simple duplex was designed. Two extra base pairs were placed at either side of each binding site to stabilise the DNA and reduce bending by the zinc finger. Under standard conditions, B-DNA has a helical period of 10.5 base pairs (Drew and Wing (1981)). Thus if two binding sites

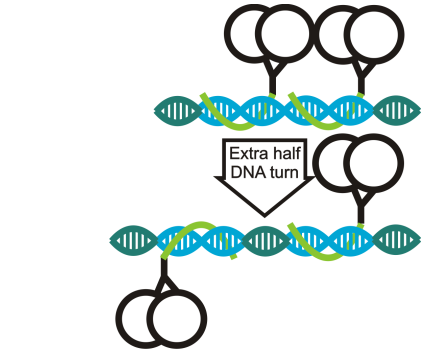

(a)

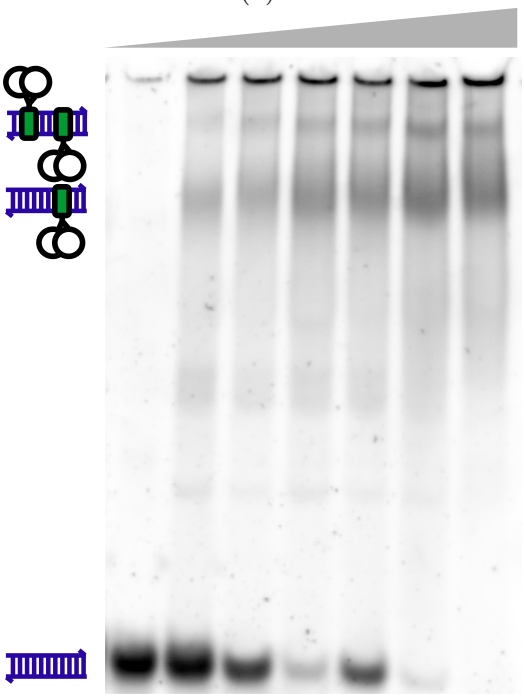

(b)

Figure 2.10: **a** Schematic illustrating the DNA-kinesin assembler. **b** Native polyacrylamide gel stained with SYBR^{TM}Gold containing samples of assembler DNA (0.25μM) and different concentrations of zinc finger kinesin (0 μM, 0.5μM ,1μM, 1.25μM , 1.5μM, 2μM, 2.5μM)

are next to each other, bound protein will protrude from the DNA in approximately the same orientation (schematic shown in Figure 2.10a). In order to maximise the likelihood of the two motors binding to different microtubules, the binding sites were orientated approximately anti-parallel by inserting an

extra 5 bases of DNA between them. This DNA-kinesin complex is called the assembler (full sequence in Appendix B B.1.1). Figure 2.10b shows a native polyacrylamide gel of the assembler with different concentrations of kinesin. As the concentration of kinesin is increased the intensity of a band corresponding to two motors bound to the DNA also increases. This construct was also found to readily form asters when mixed with microtubules and ATP. Figure 2.9 shows a fluorescence micrograph of an aster formed using this construct.

2.8 Controlling microtubule length

Aster formation is sensitive to the microtubule length distribution. This sets the size and shape of asters formed and can completely impede self-organisation. If microtubules are too long, greater than $\sim 25\mu$m, asters will not form. At these lengths, microtubules at sufficient concentration for aster formation, are not freely diffusing in solution but tangled in a network of microtubules. This disrupts organisation as the assembler motors cannot work against the tension from the microtubule network. In order to ensure the formation of asters, various methods for controlling microtubule length were investigated. Microtubules can be shortened after polymerisation through shearing, either with a fine gauge needle or by centrifugation. The tubulin

polymerisation protocol can also be adjusted for optimum length.

Shearing

Microtubules can be shortened by exposing them to shear flow (Williams and Rone (1989)). One method for doing this is to pass solutions through a fine gauge needle. This was investigated by Jeune-Smith and Hess (2010) and it was found that the mean length could be reduced significantly but the distribution in length polydispersity was unaffected. Microtubule solutions which were too long to form asters were passed through a 29G needle with 1 to 2 passes. Inconsistent results were obtained with aster organisation observed with some solutions but not others.

Centrifugation

Shear flow can be achieved through centrifugation. This will also separate longer microtubules from shorter ones. Solutions of microtubules which were too long to form asters were centrifuged at 12,000g for 10 minutes and samples taken from the top of the solution. Again this did not result in consistent aster organisation, possibly due to the unknown changes to microtubule concentration caused by separating microtubules in solution.

Growth protocol

The effects of changes to the tubulin polymerisation protocol, outlined in Section 2.4, were investigated. Changes to seed formation time and GTP concentration were found to have little effect. Tuning the final tubulin concentration and the end to end joining time were found to have the most effect on microtubule length. The tubulin concentration was varied from 10-20μM by adding buffer to microtubule solutions. In this way microtubules were tuned for aster formation with an optimum tubulin concentration of $\sim$16μM. If microtubules were too short for use, they were elongated by leaving for 1-2 days to allow room temperature end to end joining to occur. This process could potentially be speeded up by annealing (Jeune-Smith and Hess (2010)). Batches of microtubules were flash frozen and stored at -80°C.

Microtubule length distribution

The size distribution for microtubules made using the growth protocol above with optimum tubulin concentration was measured. fluorescence micrographs of microtubules stuck to the surface in a gliding assay were recorded and lines of best fit drawn along microtubule lengths in the program ImageJ. The lengths of these lines were measured and their distribution is shown in Figure 2.11. The distribution is approximately exponential as the likelihood

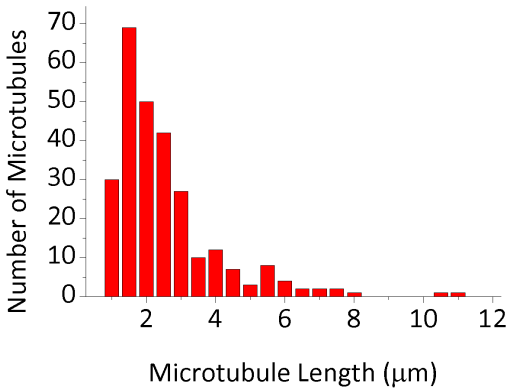

Figure 2.11: Microtubule length distribution measured by drawing the line of best fit in ImageJ. Microtubules made with the same protocol as those used to make asters. Short microtubules are under sampled.

of longer microtubules decreases. Very small microtubules $<0.5\mu$m are under sampled as it is difficult to differentiate these microtubules from free fluorescent material (such as unpolymerised labelled tubulin).

2.9 Fluid addition

In order to use asters as a transport network, a means of adding cargo and signals was required. These additions were in the form of fluid flows and so asters had to be tethered to the surface whilst imaging. Various tethering methods were investigated and a system for achieving fluid flows whilst imaging under the microscope was also developed, utilising the phenomenon of passive pumping. Experiments were then carried out to check that asters could survive fluid flow.

2.9.1 Flow chambers

Passive pumping

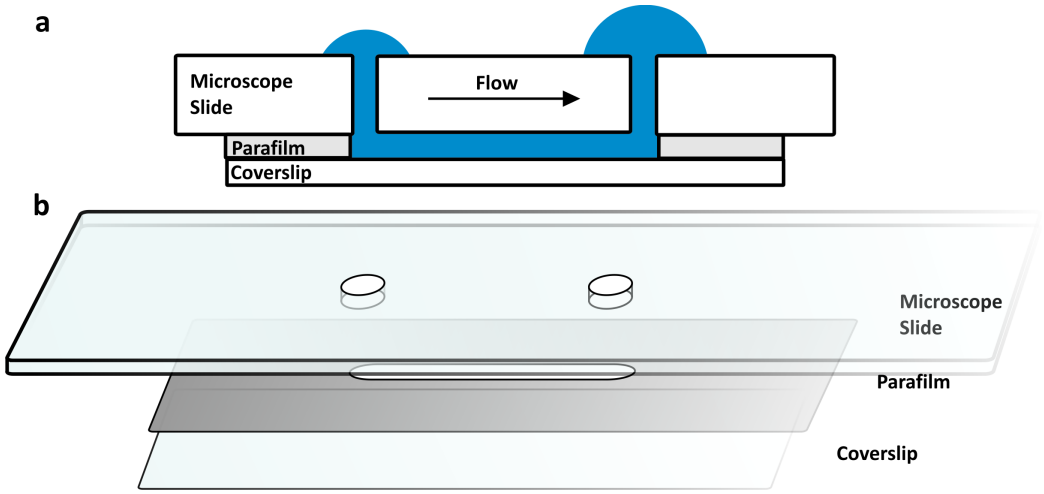

Figure 2.12: Schematic of the passive pumping chamber. **a** side view of the chamber with fluid flow from a small droplet at one inlet to a larger droplet at the other. **b** exploded view of the passive pumping chamber.

The experiments described in Chapter 3 and Chapter 4 required a method for adding solutions to a microscope sample whilst imaging. These solutions usually contained DNA or protein and so it was desirable to be able to add small volumes. The samples being imaged contained delicate microtubule structures and so a gentle method of fluid addition was required to avoid damaging structures. Many microfluidic systems use external pumps connected to a flow chamber but these often require large volumes of fluid. A flow chamber was designed which utilised passive pumping for fluid addition which needed only very small volumes and basic equipment.

Fluid can be pumped passively into chambers by utilising the pressure difference between two liquid drops of different size. The Young-Laplace equation,

$$\Delta P = \frac{2\gamma}{R} \tag{2.1}$$

describes the pressure difference at the air liquid interface, P, for a drop of radius, R and with a surface tension, γ, (Walker and Beebe (2002)). As this pressure is inversely proportional to radius, if a small drop and a larger drop are connected by a channel, fluid will be passively pumped from the small drop to the larger drop. With this simple system, sophisticated fluid flows can be achieved including the creation of stable gradients (Du et al. (2009)) and continuous flows. Flow from the small drop is biphasic, the second phase having a stable flow rate (Berthier and Beebe (2007)). This allows continuous flow to be achieved using an automated dropper (Resto et al. (2010)).

Passive pumping chambers are often made from polydimethylsiloxane (PDMS) (Walker and Beebe (2002)) which can be moulded into inlets and a channel. A passive pumping chamber made from glass slides and parafilm was devised, illustrated in Figure 2.12. Two 0.5mm holes, 25mm apart were drilled into a glass microscope slide using an ultrasonic drill. A section of

parafilm was placed over the two holes and a 3mm channel cut between them. The channel was covered with a glass coverslip and heated to seal the chamber. The chamber volume was $\sim 7\mu$l (which gives a chamber height of 0.1mm). The top surface, containing the inlets, was coated with Rain X$^{\text{TM}}$(Bazylak et al. (2008)), a hydrophobic coating designed for car windscreens, which ensured droplet formation at the inlets. The chamber was initially filled with a pipette and then fluid added using a large 5μl drop at one inlet and successive 2μl additions at the other inlet. During imaging, any liquid drops were removed by pipette and a coverslip was placed over both inlets as evaporation drives flow away from the large drop (Du et al. (2009)). Assuming a drop radius of a $\sim 2\mu$l sphere (0.78mm) and the surface tension of water to be $\sim$ 75 mN/m (Jasper (1972)) the pressure difference is 200 Pa. The flow in the channel can be modelled as plane Poiseuille flow (Landau and Lifšic (1995)) by the following equation:

$$Q = \frac{h^3 W}{8\mu} \frac{dP}{dz} \tag{2.2}$$

where Q is the volumetric flow rate, h is the chamber height, W is the chamber width, μ is the viscosity, dP is the pressure difference between the inlets and dz is the length of the channel. Using the pressure difference calculated from the Young-Laplace equation and the dimensions of the chamber

given above, gives a flow rate of $\sim 3\mu$L/s. This is faster than the observed rate of $\sim$1uL/s but this is in part due to the increase in drop radius during flow such that this is the maximum pressure and flow rate (Walker and Beebe (2002)). This leads to a complicated flow rate as a function of time (Walker and Beebe (2002)) which can be biphasic if the droplet radius is march larger than the inlet (Berthier and Beebe (2007)). Depending on the hydrophobicity of the surface, the droplet will not be a perfect hemisphere above the inlet and so the radius may be slightly larger, further explaining the observed flow rate.

Mixing chambers

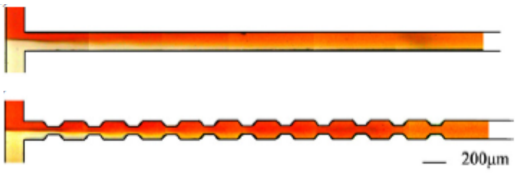

Figure 2.13: Mixing chambers from Hsieh and Huang (2008) filed with water and Iodine dye. Fluid in the lower, roughed chamber mixes better than the smooth chamber.

To image aster formation it was desirable to observe the mixing of assemblers and microtubules. Passive pumping chambers allow addition of fluid but not necessarily mixing. If the sample in the flow chamber is anchored to the surface, then whatever is pumped in will mix with the sample. The Reynold's number in microfluidic systems is low, causing laminar flow. This means pumping one fluid into another will not mix the two. A flow chamber

was designed, similarly to the passive pumping chamber but with two inlets, so that two solutions could be pumped in simultaneously. The solutions will not mix unless laminar flow is disrupted. This can be achieved by roughing the edges of the chamber or placing obstacles in the flow (Hsieh and Huang (2008)). Figure 2.13 contains images of mixing chambers from Hsieh and Huang (2008) filled with water and Iodine dye. Full mixing only occurs in the roughed chamber. A similar chamber shape was cut into Parafilm^{TM}and constructed similarly to the simple flow chamber.

2.9.2 Surface Binding

Two strategies for tethering asters were tested. Non-specific attachment was tested using polylysine and specific attachment was tested using tubulin antibody, biotinylated tubulin and biotinylated DNA.

Polylysine

Polylysine can be used to attach cells and proteins to microscope coverslips. A simple flow chamber was coated in polylysine by washing twice with 0.01% polylysine and incubating for 4 minutes. Two washes with 20mg/mL BSA were used to block uncovered parts of the surface and partially temper the polylysine binding strength to avoid inhibiting motors. A solution of asters was added and imaged. Asters were found to stick tightly to the sur-

face. Some were still dynamic but many were static implying the polylysine may hinder the motors. Solutions of microtubules which contained more depolymerised tubulin, such as older microtubule solutions, contained a higher percentage of active asters when bound to polylysine. This implies that adequate blocking of the polylysine could tether asters without impeding motors. Polylysine also binds DNA (Evett and Isenberg (1969)) so this attachment was not used as cargo and signals could become stuck to the surface.

Tubulin antibody

Tubulin antibody was obtained commercially (Cytoskeleton^{TM}). Flow chambers were coated in antibody with two washes of 0.1mg/mL polyclonal tubulin antibody with 3 minute incubations and then two washes with 6mg/mL BSA. This surface coating was found to bind microtubules well but not asters. The antibody preferentially binds free tubulin and microtubules. The few asters bound were either very small or were only tethered by a few microtubule ends at the aster periphery. In solution, asters are 3D so only the microtubule astral ends are accessible to the surface.

The tension in the motors and microtubules holds the aster away from the surface, preventing more of the astral microtubules from binding to the antibody.

biotinylated Tubulin

Asters could be tethered to the surface by assembling them from microtubules made with a dilute mix of biotinylated tubulin and coating the surface in streptavidin. Flow chambers were coated in streptavidin as in Section 2.6. This means of tethering had similar problems to antibody; most of the biotins on the aster were inaccessible to the surface. Unpolymerised biotinylated tubulin covered the surface and asters that were stuck were not anchored by enough microtubules.

biotinylated DNA

The best aster tethering was obtained using a streptavidin coated surface and biotin on the assembler DNA. Asters were formed as normal using the biotinylated assembler and then added into a streptavidin coated chamber. This worked very well with a large proportion of asters stuck to the surface. The action of the motors, splays the aster on the surface. This allows many more biotins to be accessible to the surface, anchoring the aster by more points, as well as improving microscopy of asters by making them quasi-2D structures.

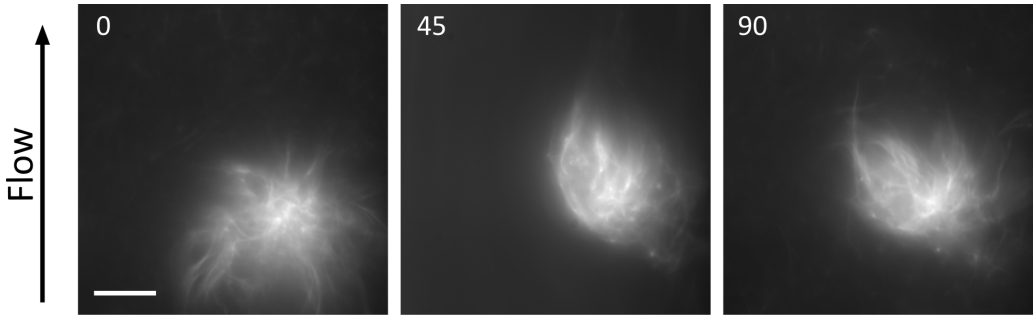

Figure 2.14: Series of fluorescence micrographs of an aster surviving a flow of buffer in a passive pumping chamber. Scale Bar 10μm. Time in seconds indicated.

2.9.3 Asters and fluid flow

Experiments were performed to check if the surface attachment was strong enough for asters to survive flow in passive pumping chambers. Asters were tethered in a streptavidin coated passive pumping chamber before imaging buffer was added. Figure 2.14 shows a sequence of fluorescence micrographs before the flow at 0s, during flow at 45s and recovery after flow at 90s. The asters remains intact and tethered to the surface throughout the flow. At 45s, the aster is deformed into tear drop by the flow field. Once the flow has stopped, the structure returns to a more astral shape as bent microtubules straighten and are re-organised by assemblers.

2.10 Characterising Structures

With a DNA-kinesin assembler capable of forming asters and system of surface tethering and flow chambers to allow asters to be used a platform

for transport, experiments were undertaken to characterise the structure of asters and their dynamics. Asters were characterised by microscopy and their size distribution was measured. Controls were performed with modified assembler DNA. Experiments were performed to attempt to visualise the formation of asters but only some intermediate dynamics were found to be observable. Different structures formed by the system, including a very long microtubule bundle, are discussed.

2.10.1 Aster Microscopy

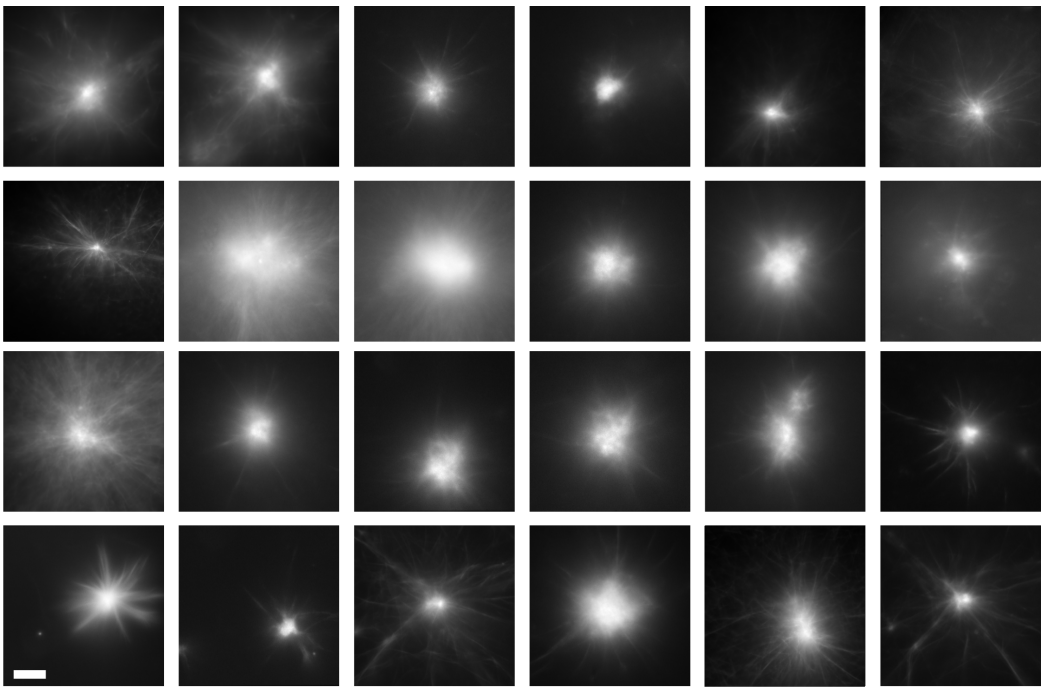

Figure 2.15: fluorescence micrographs of typical asters formed using the DNA-kinesin assembler, showing their radial structure. Scale bar 10μm.

Fluorescence microscopy was used to observe asters throughout. Figure

2.15 shows fluorescence micrographs of typical asters formed using the assembler and tethered to the surface. Their radial structure is clearly visible. Some appear more splayed and are more closely bound to the surface . The size and microtubule density profile varies between asters. The efficacy of aster formation by the assembler was measured and the size distribution of the asters formed was characterised.

Formation Control Experiments

Experiments were performed to measure the efficacy of aster formation by the assembler by measuring the aster surface density in the flow chamber. A solution of asters was tethered to the surface in a simple flow chamber. The chamber was systematically sampled, moving the field of view across the chamber and counting the asters seen. With the assembler, asters were found with a density of approximately $10^{-4}\mu m^{-2}$ or one every two fields of view (50 μm across).

Control experiments were performed with an assembler without the half twist between the two kinesins and with a mutated binding site such that only one kinesin was bound to the assembler. No asters were seen with either of these assemblers. Therefore the geometry of the motors is crucial for aster organisation.

Radius of gyration

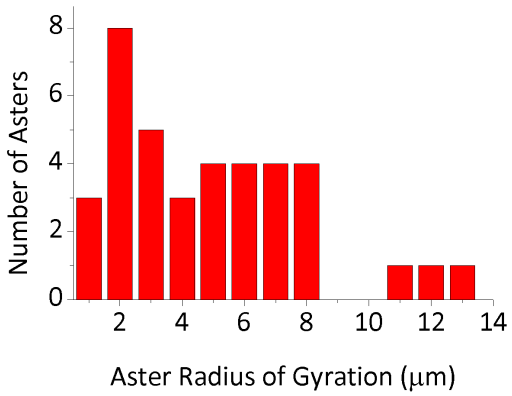

Figure 2.16: Aster radius of gyration distribution of a systematically sampled chamber.

A chamber containing asters was systematically sampled and the size measured for all asters found to avoid bias. Images were first thresholded, to identify microtubules, using the mode pixel intensity as a measure of the background. Aster radius of gyration of pixels above the threshold was measured, first by calculating the centre of mass, using the intensity (proportional the to aster mass):

$$r_c = \frac{1}{I_{sum}} \int I r \, dr \tag{2.3}$$

where I is the intensity, I_{sum} is the total aster intensity and r is the spatial co-ordinate. Then the radius of gyration is:

$$r_g^2 = \frac{1}{A} \int (r - r_c)^2 \, dr \tag{2.4}$$

where A is the aster area. The results are shown in Figure 2.16. The distribution of radii is consistent with the microtubule length distribution in Figure 2.11.

2.10.2 Aster Dynamics

Imaging Formation

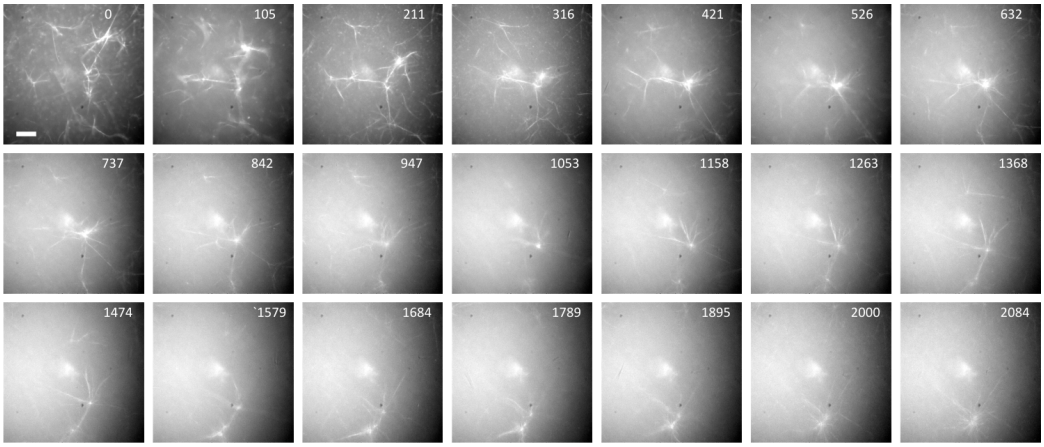

Figure 2.17: Time series micrographs of aster dynamics. Scale bar is 10 microns. Time in seconds indicated.

Observing the complete formation of asters from free microtubules is very difficult. The formation process is discussed in Nédélec et al. (1997, 2001); Surrey et al. (2001) but no data showing formation is shown. Asters or proto-asters form immediately after mixing microtubules and assemblers. Experiments were attempted to see formation from the moment microtubules and assemblers were mixed using the mixing chamber described in Section 2.9.1. Imaging with a 100x or 60x objective has a field of view of $\sim$50 μm and $\sim$80

μm across respectively. The chances of observing a structure forming inside the field of view and in the right focal plane are slim. Even if a structure starts forming whilst observing, it is not likely to remain still and will drift in 3D. The beginnings of asters are also difficult to distinguish from free microtubules in solution. These factors combined have meant that it has not been possible to watch formation from individual microtubules.

The closest to seeing microtubules and assemblers form asters is shown in Figure 2.17, using the streptavidin assembler and lower ATP concentration ($\sim$100μ M)to slow down formation. Small proto-aster structures are seen coalescing into an aster. Imaging time was very long, over 30 minutes and so photo-bleaching occurs. Time lapse imaging (to avoid photo-bleaching) was not initially possible as the timescale of aster dynamics was unknown, however it could be used in future experiments. Initial joining is rapid and then much slower as the structure grows larger. This implies initial structures form very quickly and so imaging this process would be very challenging.

Joining

Observation of the aster joining process was much easier. Figure 2.18 shows fluorescence micrographs of asters formed using the assembler. Two asters are seen merging over $\sim$2 minutes. A slightly elongated central region is

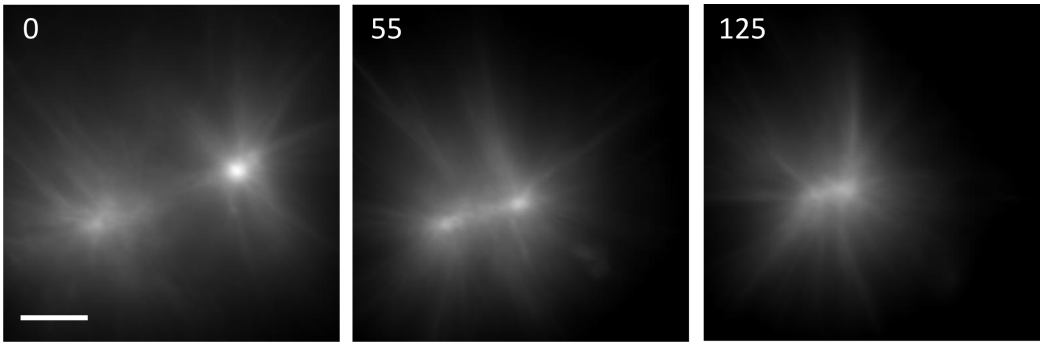

Figure 2.18: Time series micrographs of aster dynamics. Scale bar is 10μm. Time in seconds indicated.

visible after the asters have joined where the centres have not completely merged.

2.10.3 Mega-bundle

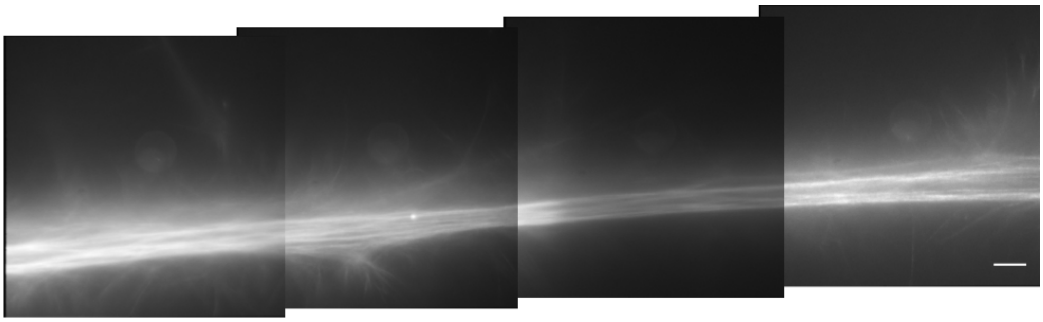

Figure 2.19: Section of megabundle. Scale bar 10μm.

If there is a large population of long microtubules, but not so many as to completely repress the organisation of any structures, very large bundles have been observed. Figure 2.19 shows several micrographs hand-stitched together of a section of one such bundle. This bundle was seen to extend over hundreds of microns and may even extend into the millimetre length scale similar

to Idan et al. (2012). Some of these bundles were observed to form from networks of asters which constrict together over time. These aster networks are elongated by flow into the chamber as they were always found parallel to the flow direction. It would be interesting to investigate the microtubule orientation inside these bundles. If they are all formed from coalescence of asters then presumably they have periods of aligned microtubules separated by nodes. Orientation could be ascertained by observing single molecule kinesin transport and comparing direction between different bundle regions.

2.11 Conclusion

A DNA-kinesin hybrid has been developed using a zinc finger fusion kinesin whic binds to a specific 9 bp sequence of DNA. A DNA nanostructure was used to arrange hybrids such that they could cross-link microtubules and self-organise asters. Asters were tethered through the DNA to the surface of flow chambers. The passive pumping phenomenon was used to flow in new solutions and the surface tethering was found to be strong enough and the asters hardy enough to withstand these flows. Asters were characterised by measuring their density in the flow chamber and their size distribution. It was not possible to image their formation from free microtubules but intermediate dynamics were observed. With well characterised morphology and a robust

system for solution exchange - allowing signals to be added during imaging - asters can serve as a track network, providing a platform for molecular transport.

Chapter 3

Cargo Transport

This chapter describes the design and operation of a molecular transport system. Asters serve as a network of tracks for DNA-kinesin shuttles to ferry cargo. It will be shown that shuttles moving on orientated microtubules in the aster accumulate or actively concentrate cargo and that this effect can be harnessed for the molecular transport system. The concentration [1] of cargo can be controlled by the supply of ATP and cargo can be removed from the aster centre using DNA encoded signals carried by their own shuttles. This allows for repeated cycles of concentration and release. The system was used to investigate the requirement for active transport. The cargo release signal was delivered by diffusion, unattached to kinesin shuttles and found

[1] concentration refers to the accumulation of cargo

to be ineffective compared to active transport. Similarly to eukaryotic cells, molecular motors are required for effective transport but, in the molecular transport system's case, due to the molecular crowding at the center of the aster.

3.1 Designing a DNA-Kinesin shuttle

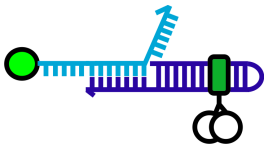

Figure 3.1: Schematic of the DNA-Kinesin shuttle. Cargo in light green, DNA in blue, Cargo DNA in light blue.

A simple DNA-kinesin shuttle was designed incorporating a DNA scaffold with only one zinc finger binding site (schematic shown in Figure 3.1 and sequences in Appendix B B.1.2). To minimise the number of single strands of DNA used to build the DNA nanostructure, the kinesin binding section of the shuttle (dark blue) was designed as a hairpin, with the stem containing the zinc finger sequence. A single stranded section protrudes from the stem which acts as a binding domain for a cargo strand (light blue). A portion of the cargo strand is fully complementary to the cargo binding domain on the shuttle. It also contains two single-stranded toe-holds which allow the cargo to be removed through toe-hold mediated strand displacement (see Chapter

1 Section 1.6.1). The cargo strand can carry cargo which can be attached to DNA.

3.2 Shuttles and asters

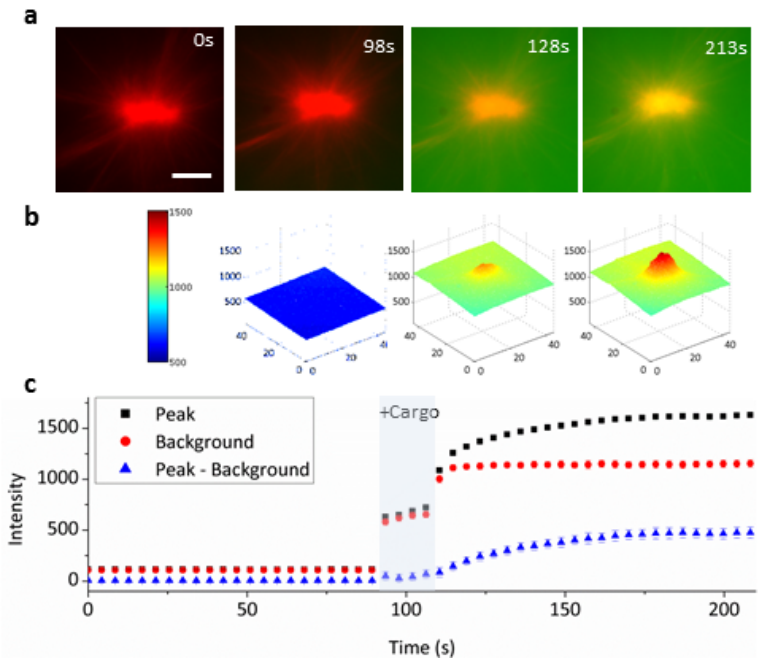

Figure 3.2: **a**. Fluorescence micrographs before and after addition of cargo. The cargo is seen concentrating in the centre of the aster over time. Rhodamine-labelled microtubules are shown as red; cargo (Cy3) is green. Scale bar 10μm. **b**. 3D surface plots of cargo in the micrographs in **a**. **c**. The peak, background and peak-background intensity over time.

Cargo shuttles were loaded with a fluorescent cargo, the cyanine dye - Cy3. A solution of shuttles was flowed over tethered asters and observed. Dual colour fluorescence micrographs, shown in Figure 3.2 **a**, were obtained using an automated filter cassette which switched between the microtubule and cargo filters (described in Appendix A Section A.8) every ∼4s setting

the frame rate. The micrographs show the cargo localising to the centre of the aster. To better visualise the localisation of cargo, the fluorescence intensity is plotted as a colour-mapped 3D surface in Figure 3.2 **b**. The addition of cargo on the plot is highlighted in blue to illustrate the finite time of fluid addition. An intensity peak forms as the cargo concentration in the centre increases. The central cargo concentration was followed over time by plotting the background subtracted central peak intensity over time, shown in Figure 3.2 **c**. The peak height was determined by finding the maximum of a 2D Gaussian and the background defined as the mode pixel value. The background can also be defined by finding a part in frame where there is no aster and taking the mean. As long as the aster does not completely cover the field of view, then the mode serves as a good value for the background. As the cargo is added, the background and peak increase sharply but the peak-background remains unchanged (blue trace) until the shuttles actively concentrate cargo at the centre and it increases. The peak-background saturates as no more cargo can be brought to the centre.

3.2.1 Quenchers

The assembler was modified with a quencher which could quench the Cy3 on the cargo strand. Experiments were performed similar to those in Section

3.2 to see if the quenchers could mask some of the fluorescence due to the concentrated cargo in the centre of the aster. The quenchers had no observable effect and were not found to be necessary. Some of the data shown here (Section 3.4, Section 3.5) used the quencher assembler but this did not change the dynamics of the system. If the quencher were to have any effect it would suppress the observed concentration of cargo. The quenchers were removed in later experiments.

3.3 Asters as a transport network

Asters and the concentration of cargo by shuttles can be the basis for transport network. Asters are polar structures with the microtubule minus ends at the periphery and plus ends at the centre. This allows cargo distribution to be controlled by the directionality of its attached motor. The microtubule plus ends are densely packed into the centre of the aster. Plus end directed motors will cluster around the aster centre. They will periodically drop off but due to the extremely high microtubule concentration at the centre, they are very likely to rebind. This gives rise to an active concentration effect where shuttles become ever more concentrated at the centre until a saturating point is reached. Conversely, attaching cargo to minus ended motors would deplete cargo concentration at the centre, although this effect is not

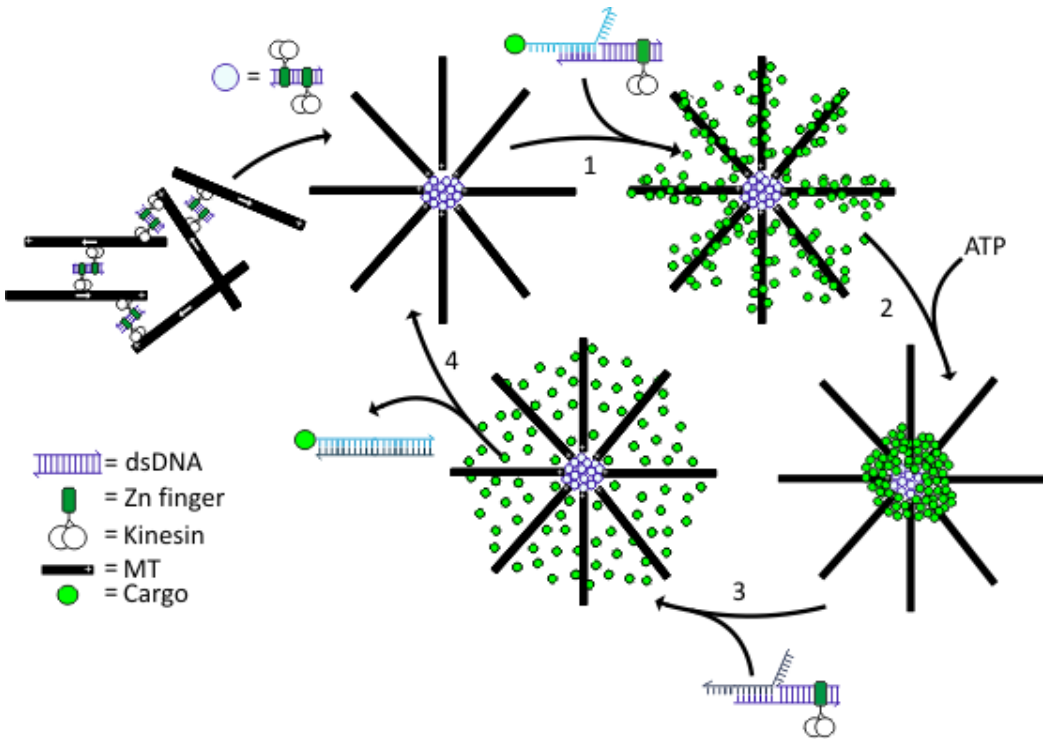

Figure 3.3: The self-organized transport system. 1. DNA-templated kinesin teams organise microtubules into radial asters. 2. Shuttles carrying fluorescent cargo decorate the aster uniformly in the absence of ATP. 3. ATP fuels cargo concentration. 4. A DNA-encoded signal is actively transported to the centre of the aster to release the cargo.

as strong as the concentration effect (Nédélec et al. (2001)).

The distribution of shuttle carried cargo on asters can be controlled. To control the concentration effect, and see cargo move from a dispersed to a concentrated state, the supply of ATP can be regulated. Cargo-loaded shuttles can be added in the absence of ATP and decorate the aster uniformly. With the addition of ATP, the shuttles will concentrate their cargo into the centre of the aster. The cargo can be removed by minus ended motors or by making use of DNA interactions. A strand displacement reaction using a release strand can strip off the cargo strand through its toe-holds. This strand can also be carried by a shuttle and cargo dispersed using a single molecular motor. In essence the release strand is a DNA encoded signal to unload the cargo.

A transport system was designed combining control of concentration and release. The full operation of the transport system is shown in Figure 3.3 including assembly of the synthetic astral track network and a cycle of loading, active concentration and release of the cargo. Microtubules and assemblers are mixed in the presence of ATP to form asters (step 1). ATP is removed and cargo-loaded shuttles are added, binding passively to the microtubules in the rigor state (step 2). On addition of ATP (step 3) the shuttles walk towards the centre of the aster, actively concentrating the cargo. Finally,

(step 4) shuttles carrying the DNA instruction to unload are added. They bind and walk to the centre of the aster, transporting the DNA signals towards the concentrated cargo shuttles. When a shuttle bearing an unloading instruction encounters a shuttle carrying cargo, unloading is initiated: hybridization between the instruction strand and the cargo strand displaces both from their respective shuttles, forming a stable duplex and releasing the cargo back into solution.

3.4 Concentrating cargo

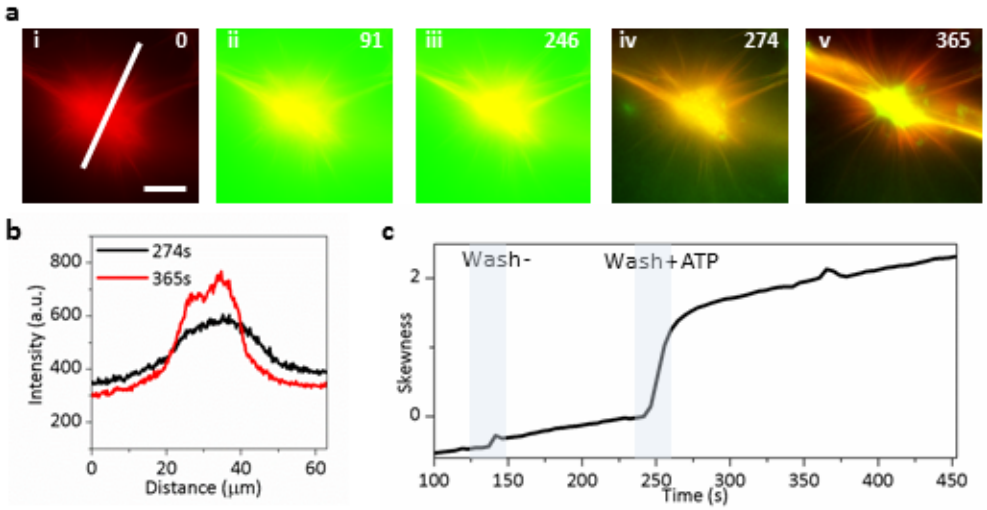

Figure 3.4: Active cargo transport to aster centre. **a**: Fluorescence micrographs: i before any additions; ii after addition of cargo without ATP; iii after wash without ATP; iv just after ATP addition; v 1min after ATP addition. Intensities are scaled consistently in all images. Rhodamine-labelled microtubules are shown as red; cargo (Cy3) is green. Scale bar 10μm. **b**: Intensity distributions along a cross section through the centre of the aster (shown as a white line in **a**(i) and the same in all frames) before and after ATP addition. **c**: Skewness (see Section 3.9) of the intensity-weighted pixel intensity histogram for cargo fluorescence channel images.

Experiments were performed to test sections of the transport system Fig-

ure 3.4 contains data from an experiment to test control of cargo concentration. Cargo loaded shuttles were added to an aster but without ATP. Figure 3.4 **a** shows a sequence of dual-colour fluorescence micrographs of an immobilized aster (**a**i). Cargo-loaded shuttles were added without ATP (**a**ii): after excess cargo was washed away (**a**iii), cargo decorated the aster uniformly through rigor-state binding of the shuttle kinesins. After addition of ATP ((**a**iv) the cargo was transported to the centre of the aster within ∼90s (**a**v). Figure 3.4 **b** shows the intensity of cargo fluorescence along a cross section through the centre of the aster: a central peak formed on addition of ATP, consistent with cargo concentration.

These experiments show that the shuttles play an active role in concentrating the cargo at the centre of the aster. In theory, the distribution of microtubules in the aster might cause shuttle bound cargo to accumulate at the centre of the aster. The microtubule density is much higher in the centre and if cargo loaded shuttles were free to bind anywhere, more would bind in the centre even in the absence of ATP. In these experiments cargo was seen to concentrate in the absence of free cargo loaded shuttles in solution and only in the presence of ATP, thus cargo is actively transported to the centre. Later results (Figure 3.8) and discussion (Section 3.8) imply that shuttles are not free to bind anywhere on the aster and may even be impeded from

binding in the centre.

3.5 Releasing cargo

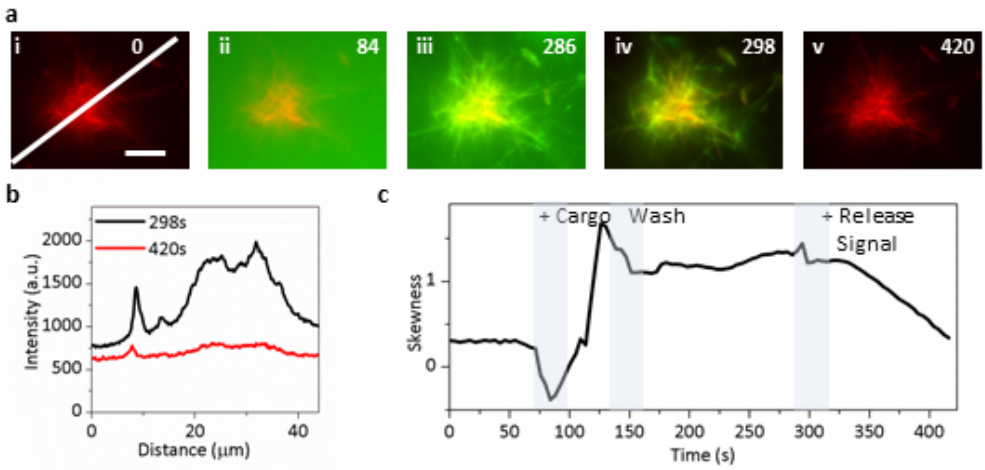

Figure 3.5: Release of cargo in response to signal. **a**: Fluorescence micrographs: i before any additions; ii after addition of cargo with ATP; iii after wash with ATP; iv just after addition of release strand; v 1min after addition of the release strand. Intensities are scaled consistently in all images. Rhodamine-labelled microtubules are shown in red; cargo (Cy3) is green. Scale bar 10μm. **b**: Intensity distributions along a cross section through the centre of the aster (shown as a white line in **a**(i) and the same in all frames) before and after addition of release signal. **c**: Skewness (see Section 3.9) of the intensity-weighted pixel intensity histogram for cargo fluorescence channel images.

An experiment was performed to test the release mechanism. Kinesin shuttles carrying cargo were added, with ATP, to an aster (Figure 3.5 **a**ii). The cargo was allowed to concentrate on the aster before excess cargo was washed out with buffer (Figure 3.5 **a**iii). Shuttles carrying the release signal were added (Figure 3.5 **a**iv) and the cargo can be seen to disperse from the aster (Figure 3.5 **a**v). A cross section of the cargo at the white line in Figure 3.5 **a**i is shown in Figure 3.5 **b**. The cargo peak decreases to almost

zero in response to the release signal. Control experiments where the release signal is delivered without ATP and the wrong signal is delivered are shown in Sections 3.10.1 and 3.10.2

3.6 Analysing Data

A metric to describe the behaviour of the system over time was required to adequately characterise it. In Figure 3.2 the peak above the background was used as a metric but better analysis of the system can be made by studying the intensity weighted pixel intensity histograms of the cargo fluorescence images.

3.6.1 Histograms

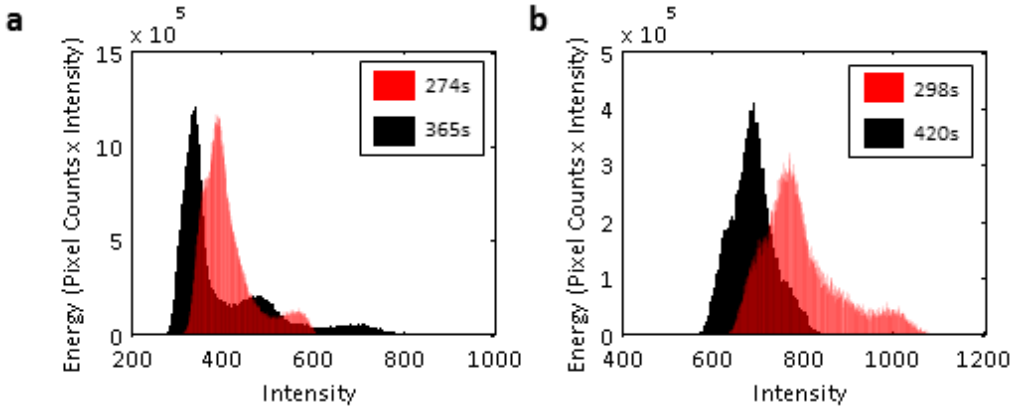

Figure 3.6: Intensity-weighted pixel intensity histograms of fluorescence micrographs of the cargo showing cargo concentration (data from Figure 3.4) and release(data from Figure 3.5). **a**: A high-intensity tail forms after ATP is added at 209s, consistent with cargo concentration at the centre of the aster. **b**: The tail disappears after addition of the release signal, actively transported to the centre of the aster, at 319s.

Figure 3.6 **a** shows two intensity weighted pixel intensity histograms of the cargo fluorescence images in Figure 3.4 iv (red) and v (black). iv is just after ATP has been added and v is ∼90s after the ATPs effect has been felt. A high intensity tail has formed in the black trace compared to the red trace. This tail corresponds to high intensity values at the centre of the aster. Thus as the cargo concentrates, higher intensity pixel values occur at the centre and the tail forms. Figure 3.6 **b** shows two intensity weighted pixel intensity histograms of the cargo fluorescence images in Figure 3.5 iv (red) and v (black). iv is just after the release signal has been added and v is ∼120s after the release signal has had time to act. The high intensity tail in the red trace disappears after 2 minutes in the black trace. This is due to the concentrated cargo in the centre of the aster dispersing in response to the release signal and the high intensity pixel values in the centre decreasing. The tail shrinks and ultimately disappears as the cargo is released. Thus by measuring the shape of the distribution, more specifically the high intensity tail, a metric of concentration and release is obtained. This can be done by measuring the asymmetry of the distribution by measuring its skewness.

3.6.2 Skewness

Skewness is a measure of the asymmetry of a distribution. Skewness (γ_1) is defined by

$$\gamma_1 = \frac{\mu_3}{\sigma^3} \tag{3.1}$$

where σ is the standard deviation and μ_3 is the third moment about the mean of the distribution. For the distribution f(x), μ_3 is defined by

$$\mu_3 = \int (x - \mu)^3 f(x)\, dx \tag{3.2}$$

where μ is the mean. Positive skewness indicates the formation of a high-intensity tail in the image intensity distribution corresponding to concentrated cargo at the centre of the aster.

Figure 3.4 **c** shows the skewness of intensity weighted pixel intensity histograms of the cargo fluorescence plotted over time for the concentration experiment. With the wash to remove excess cargo which does not contain ATP, there is little change to the skewness but when ATP was added the skewness increased dramatically and then saturated as no more cargo could be concentrated at the centre. There is a small increase in skewness when there was expected to be no ATP in the system, likely indicating that some

ATP remained and the cargo concentrated slowly. Figure 3.5 **c** shows a similar plot of skewness for the release experiment. Skewness remained static, at a low value until the cargo shuttles, containing ATP, were added. The skewness increased rapidly until a wash step removed background cargo shuttles. Then the release signal was added and the skewness decreased as cargo dispersed away from the aster and out of the field of view. Thus skewness is an excellent metric for cargo concentration and release. It is insensitive to aster morphology and only sensitive to relative changes to the distribution - thus insensitive to any change, such as photo-bleaching which affects the whole distribution. It is also very sensitive to the high intensity tail formed due to cargo accumulation which is only a small change in the distribution as a whole. The cargo central intensity used in Figure 3.2 does not have these properties. In the following analysis, skewness refers to the skewness of the intensity weighted pixel intensity histogram.

3.7 Complete cycle

Experiments were performed to demonstrate a full cycle of transport as shown in the schematic in Figure 3. Figure 3.7 **a** shows a sequence of dual-colour fluorescence micrographs of an immobilized aster. Cargo-loaded shuttles were added without ATP: after excess cargo was washed away, cargo decorated

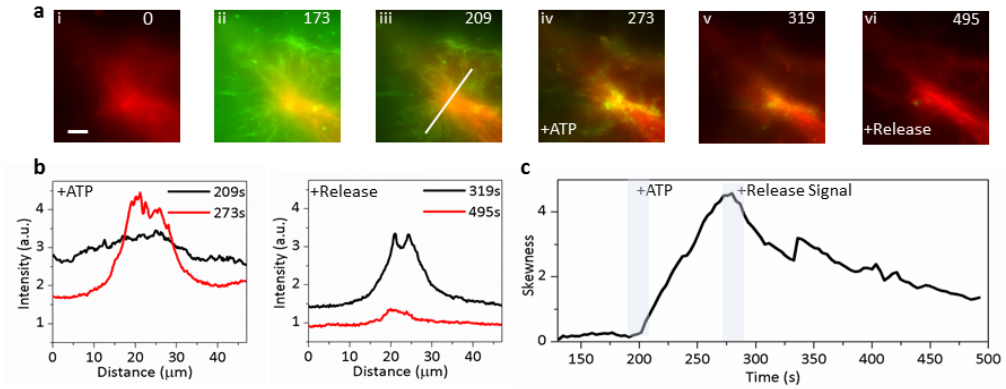

Figure 3.7: Operation of the transport system: **a**: fluorescence micrographs showing the transport cycle: i, before addition of cargo; ii, after cargo + wash with no ATP; iii, just after ATP addition; iv, 1min after ATP addition; v, just after release signal addition; vi, 3mins after unloading signal. Intensities are scaled consistently in all images. Hylite-labelled microtubules are shown in red; cargo (Cy3) is green. Scale bar 10μm. Times in seconds are indicated **b**: Intensity distributions along a cross section through the centre of the aster (shown as a white line in **a**(iii)) Top after ATP addition; Bottom after release strand addition. **c**: Skewness of the intensity-weighted pixel intensity histogram for the cargo fluorescence channel.

the aster uniformly through rigor-state binding of the shuttle kinesins. After addition of ATP the cargo was transported to the centre of the aster within 1min. Shuttles carrying the release signal were then added: having travelled to the centre of the aster they initiated cargo release and dispersal. Figure 3.7 **b** shows the intensity of cargo fluorescence along a cross section through the centre of the aster: a central peak formed on addition of ATP and dissipated on addition of the unloading signal, consistent with cargo concentration and release. Figure 3.7 **c** shows the time-dependent skewness of the intensity-weighted pixel intensity histogram corresponding to the cargo channel. The data indicate progressive cargo concentration, following addition of ATP, then dispersion triggered by addition of the release signal.

3.8 Active vs. Diffusive transport

Active transport of the release signal was compared to diffusive transport of the release signal by using the release strand alone, unattached to a shuttle in release experiments. Active transport of the signal is considerably more effective than passive transport. Figure 3.8 and Figure 3.9 combines data from 44 experiments where the cargo was actively concentrated and the release signal actively or passively transported. Skewness following addition of ATP is shown in Figure 3.8 **a**, initialised to zero in **b** and averaged over 4s time bins in **c**. On average, following addition of ATP, skewness increases with a time constant of 37s. Figure 3.9 shows the subsequent effect of the release signal, actively transported in 33 experiments and passively transported in 11. A range of different behaviours is observed in the skewness following addition of the signal (Figure 3.9 **a**). The skewness was initialised by subtracting the value after signal addition (Figure 3.9 **b**) and then averaged over all active and diffusive experiments in Figure 3.9 **c**. On average skewness decreases (with a time constant of 32s) with addition of the actively transported signal but remains static with the diffusive signal. An example of an ineffective diffusive release signal delivery is shown in Figure 3.11.

Single-molecule experiments (see Chapter 5 Section 5.4.2) show that the average shuttle velocity on isolated microtubules is $0.6 \pm 0.2 \mu m s^{-1}$ although

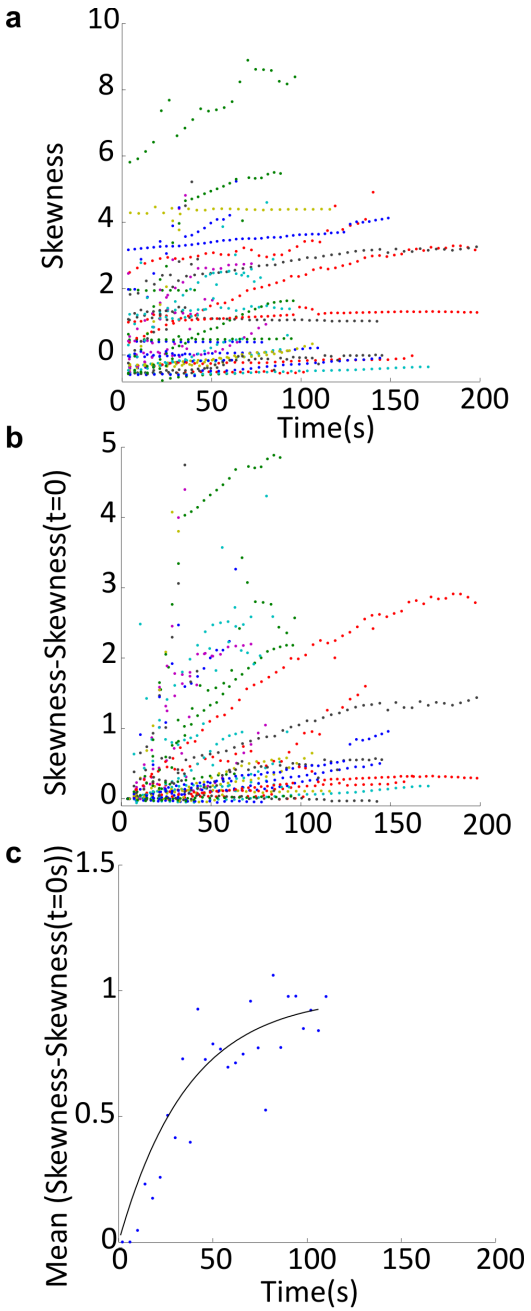

Figure 3.8: Active Cargo Concentration **a** Time-dependence of skewness after addition of the cargo and ATP b As **a**, but normalized by subtracting the skewness at t=0s, just after the ATP is added. **c** The mean of the normalized skewness in **b** over 4s time bins. The exponential function y=0.98(1-exp(-t/37)) has been fitted to the data. Averaged over all observations, skewness increases when ATP is present.

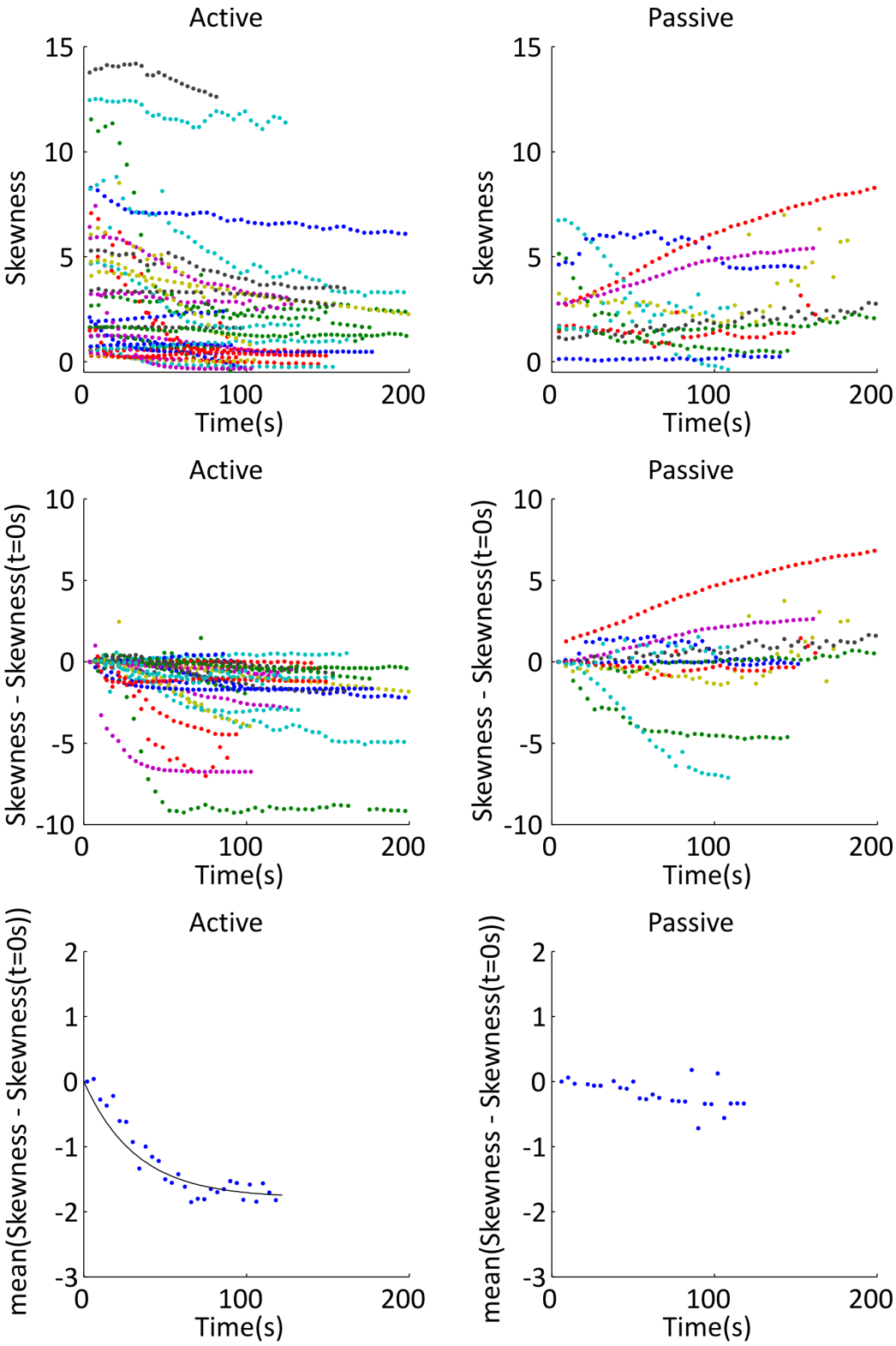

Figure 3.9: Active and passive signal transport *a* Time-dependence of skewness after addition of the release signal transported actively (left) or passively (right). **b** As **a**, but corrected by subtracting the skewness at t=0s, just after the signal is added. **c** The mean of the normalized skewness in **b** over 4s time bins. The exponential function y=1.78(exp(t/32)-1) has been fitted to the data for the actively transported signal. Averaged over all observations, skewness decreases only for the actively transported release signal.

shuttles may be slowed down by crowding (Leduc et al. (2012)) near the centre of an aster. The mean radius of gyration of asters used in these transport experiments was 10 μm (Figure 3.10), so a shuttle can traverse an aster in approximately 20s, consistent with the average timescale for active concentration and release of approximately 30s (the reaction of the release strand takes <1s at these concentrations (Turberfield et al. (2003))). Diffusive transport of the free signal strand over the same distance in water is significantly faster (Stellwagen and Stellwagen (2002)), taking of the order of 1s. Over longer distances (or with a larger, less mobile cargo), active transport would be faster than diffusion in water. The ineffectiveness of passive transport and the variation between asters is attributed to obstruction of diffusion caused by the dense packing of microtubules and assemblers at the aster centre (Nédélec et al. (2001)). This molecular crowding may also lead to signal depletion at the centre of the aster in the diffusive case. Flow delivers both signals to all parts of the aster but with active transport, the signal may be amplified. As active shuttles solution flows past, the aster will catch passing shuttles, possibly leading to an increased concentration of signal compared to the passive solution. This may further increase the effectiveness of the active signal.

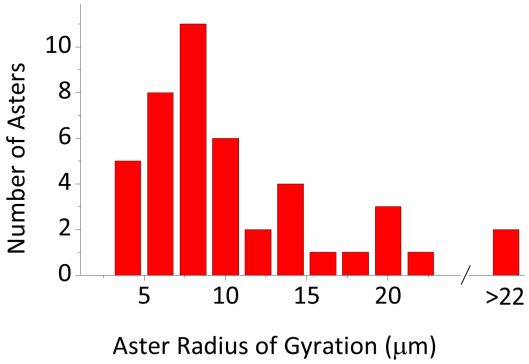

Figure 3.10: Aster radius of gyration distribution of asters in the release experiments above. Radius of gyration measured from images as described in Chapter 2 Section 2.10.1. Mean aster radius of gyration ± standard deviation is 9.8±6.6μm.

3.8.1 Diffusive Transport Example

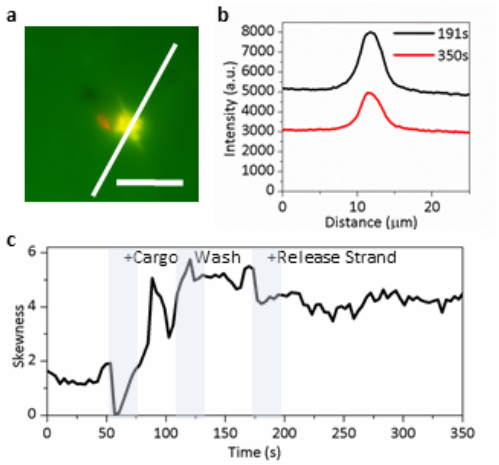

Figure 3.11: Release signal diffusively delivered. Control experiment as Figure 3.5 but release signal delivered diffusively, unattached to a motor. ATP in all additions. **a**: Fluorescence micrograph after addition of cargo and wash. Hylite-labelled microtubules are shown in red; cargo (Cy3) is green. Scale bar 10μm **b**: Intensity distribution along a cross section through the centre of the aster (shown as a white line in **a**). **c**: Skewness of the intensity-weighted pixel intensity histogram for cargo fluorescence channel images.

An example of non-active, diffusive delivery of the release signal is shown in Figure 3.11. Cargo-carrying shuttles were added to an aster in the presence of ATP and allowed to concentrate into the centre of the aster. A

corresponding increase in the skewness can be seen in Figure 3.11 **c**. Excess cargo was washed out and then the release strand alone, unattached to a kinesin shuttle was added. ATP was present at all stages of the experiment. In Figure 3.11 the skewness is unaffected and the cargo peak in the cross section remains unchanged against the background. The data is shown as an example of ineffective passive transport of the release signal but the full range of behaviour is shown in Figure 3.9.

3.9 Two cycles of transport

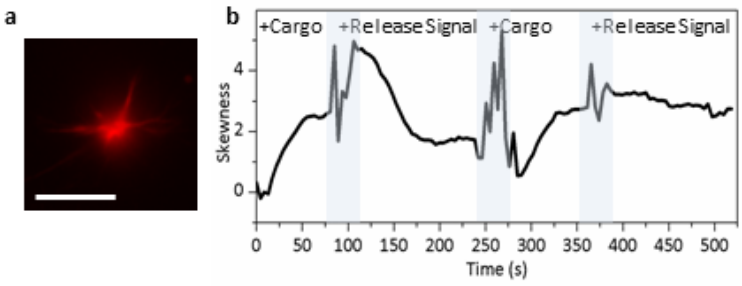

Figure 3.12: Two Cycles of cargo concentration and release a fluorescence micrograph of aster in two cycle experiment. Scale bar 10μm. b Skewness over time for two cycles of cargo concentration and release. Skewness increasing with the addition cargo and decreases with addition of the release signal in the presence of ATP.

Experiments were carried out to demonstrate that transport cycles could be repeated on the same aster. Figure 3.12 **a** shows a fluorescence micrograph of an aster used for two cycles of transport. The skewness over these two cycles is shown in Figure 3.12 **b**. Cargo shuttles and ATP were added to the

aster and skewness increased. With the addition of the release signal there is a drop in skewness. Additions of cargo and release signal shuttles were repeated on this aster with similar increases and decreases in skewness. The second release is not as effective as the first. With each addition of cargo and signals, spent empty shuttles remain in the system and may form a barrier to successive additions.

The number of additions is limited by the delicacy of microtubule asters and the violence of flow in our basic microfluidic system. With each addition there is a possibility that the aster will be washed away or damaged. With more sophisticated microfluidics, the flow rate could be more accurately controlled and more cycles of cargo concentration and release observed.

3.10 Release controls

Control experiments were performed to test the active delivery of DNA encoded signals by kinesin shuttles. Kinesin shuttles carrying the signal but without ATP and shuttles carrying an incorrect DNA signal were tested.

3.10.1 Without ATP

An experiment was carried out to test active delivery of the cargo release signal. Cargo carrying shuttles were added to an aster in the presence of

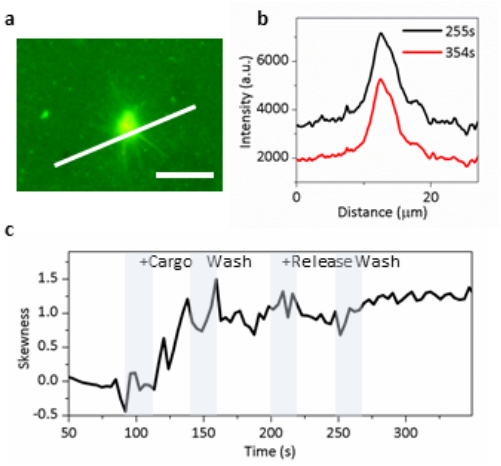

Figure 3.13: Release signal with no ATP. Control experiment as Figure 3.5 but no ATP added with release signal. Without ATP, the release signal is immobilised on the aster and the cargo is unaffected. **a**: Fluorescence micrograph after addition of cargo and wash. Hylite-labelled microtubules are shown in red; cargo (Cy3) is green. Scale bar 10μm **b**: Intensity distribution along a cross section through the centre of the aster (shown as a white line in **a**). **c**: Skewness of the intensity-weighted pixel intensity histogram for cargo fluorescence channel images.

ATP and allowed to concentrate into the centre of the aster (Figure 3.13). A corresponding increase in the skewness can be seen in Figure 3.13 **c**. The ATP was then washed out of the chamber by flowing in ATP-free buffer. The release signal bound to a kinesin shuttle was added without ATP and then a further buffer wash without ATP was performed. Cargo remains bound to the aster throughout. The skewness stays unchanged and the cargo peak in the cross section in Figure 3.13 **a** and **b** remains unchanged against the background.

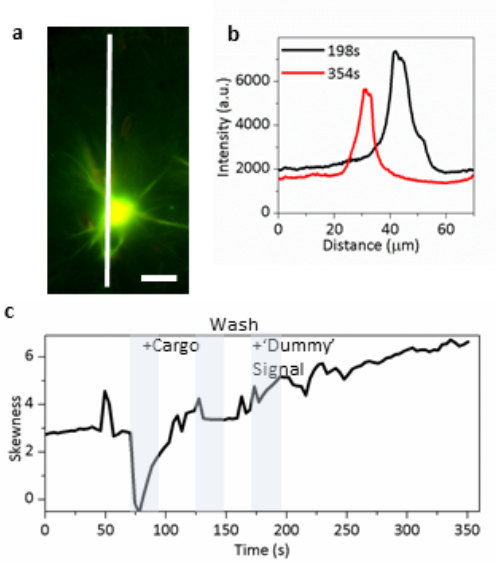

Figure 3.14: Dummy release signal delivered. Control experiment as Figure 3.5 but dummy signal added rather than release signal. ATP in all additions. With the wrong signal, no cargo is released. **a**: Fluorescence micrograph after addition of cargo and wash. Rhodamine-labelled microtubules are shown in red; cargo (Cy3) is green. Scale bar 10μm **b**: Intensity distribution along a cross section through the centre of the aster (shown as a white line in **a**). **c**: Skewness of the intensity-weighted pixel intensity histogram for cargo fluorescence channel images.

3.10.2 Dummy release signal

To test the specificity of the DNA encoded signal, DNA with the wrong sequence, a 'dummy' signal, was actively transported on the aster. Cargo carrying shuttles were added to an aster in the presence of ATP and allowed to concentrate into the centre of the aster (Figure 3.14). A corresponding increase in the skewness can be seen in Figure 3.14 **c**. Excess cargo was washed out and then kinesin shuttles without the release signal were added. ATP was present at all stages of the experiment. In Figure 3.14 the skewness is continues to increase in the presence of the 'dummy' signal, as does the

cargo peak in the cross section, Figure 3.14 **b**.

3.11 Scavenger

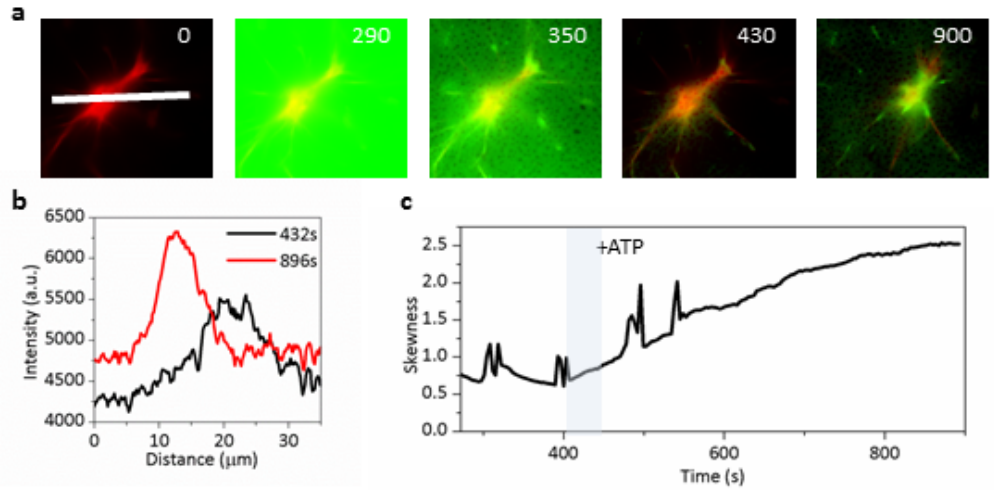

Figure 3.15: Scavenging cargo strand from solution. **a**: Fluorescence micrographs showing scavenging and transport of the cargo. 0s, the aster before any additions. Solution of shuttles, without cargo or ATP were then added. 290s the cargo strand alone was added. 350s the aster was washed without ATP to remove unbound cargo. The cargo can now be seen localised uniformly around the aster. 430s, ATP added. 900s the cargo has concentrated into the centre of the aster. Hylite-labelled microtubules are shown in red; cargo (Cy3) is green. Scale bar 10μm b: Intensity distribution along a cross section through the centre of the aster (shown as a white line in **a**). **c**: Skewness of the intensity-weighted pixel intensity histogram for cargo fluorescence channel images.

The aster transport system scavenges cargo loaded shuttles from solution. An experiment was performed to test whether the cargo loaded strand alone could be scavenged from solution. Figure 3.15 **a** shows a sequence of fluorescence micrographs of an immobilised aster. At 0s, the aster is shown before any additions. A solution of shuttles, without cargo or ATP were added to the aster. The cargo strand alone was added at 290s and given time to bind

to the unloaded shuttles. At 350s the aster was washed without ATP to remove unbound cargo. The cargo can now be seen localised uniformly around the aster. With the addition of ATP at 430s, the cargo concentrates into the centre of the aster by 900s. Cross sections showing the effects of ATP are shown in Figure 3.15 **b** and the skewness just before and after ATP addition are shown in Figure 3.15 **c**. These data demonstrate that cargo, unattached to a shuttle, can be scavenged from solution and then actively concentrated.

3.12 Conclusion

Natural geometry molecular transport systems are constrained without the use of organised tracks (Goel and Vogel (2008)). The aster structure, similar to the radial microtubule array utilised in nature, was used as a track network for the transport of cargo by DNA-kinesin shuttles. These shuttles actively concentrate their cargo on asters. This effect was harnessed to create a cyclic transport system where cargo was scavenged from solution, actively concentrated and then released back into solution by an actively transported DNA signal. Active signal delivery was compared to diffusion and found to be significantly more effective, in the crowded environment, at the centre of an aster. In these experiments, molecular complexes that are a few nanometres in dimension transport cargo and control information flow over

tens of micrometres. The active concentration of components, demonstrated by shuttles on asters, could be used to create colour changes (Bouchard et al. (2006); Tuma et al. (1998)) and to speed up reactions at low concentration of reactants or with high activation barriers (Simmel (2012)).

To use active concentration of components to speed up chemical reactions using the molecular transport system, a measure of the accumulated cargo concentration or the degree of accumulation is desirable. This is difficult to obtain using standard fluorescence microscopy as the whole 3D morphology of the cargo contributes to the fluorescence making a conversion between fluorescence intensity and concentration difficult. A very rough estimate of the degree of accumulation or concentration due to the motors can be made from the relative increase in peak height in the cross sections with ATP addition (shown in fig 3.4, 3.7 and 3.15). This is between 1.2-1.6x. This is only from the motors accumulating, asters will already have a higher amount of cargo than solution as cargo-loaded shuttles are scavenged from solution. The degree of accumulation may then be much higher. These values also assume that the fluorescence intensity is proportional to the concentration but there may be complex photo-physics with such tightly packed fluorophores. The term active concentration is used for cargo accumulation, despite the cargo being attached and not free in solution and so is not concentration in the

traditional sense. However, the cargo can be released back into solution using a DNA signal and at a higher concentration due to its accumulation by active transport.

Chapter 4

Disassembly

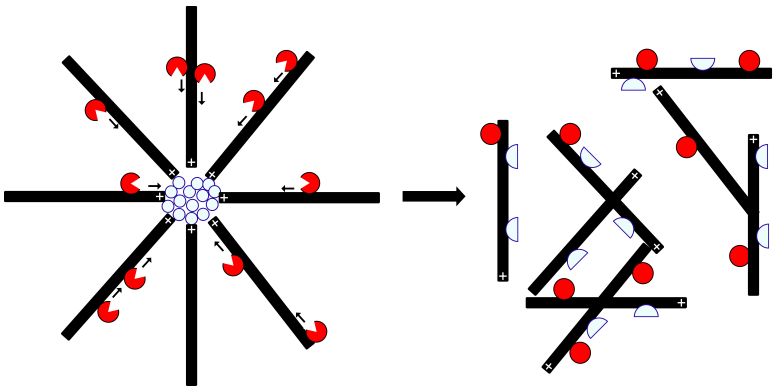

Figure 4.1: Schematic of aster breakup in response to a signal. Asters are formed from assemblers (white circles) and microtubules (black rods). A signal is carried by shuttles (red 'pac-mans') which causes the assembler to split and disassemble the aster. Spent signals are shown as red circles and assembler halves as half white circles.

As well as controlling the cargo, DNA encoded instructions were made to interact with the self-organisation process. The cargo transport system described in Chapter 3, was redesigned to allow asters to be destroyed in

response to a signal. This required a modified aster forming assembler which could respond to a DNA signal. Asters were formed using this modified assembler and signals, carried by kinesin shuttles were added. The signal causes the assembler to break in half, terminating the cross-links holding the aster together, and breaking the aster apart, illustrated in Figure 4.1.

4.1 DNA designs

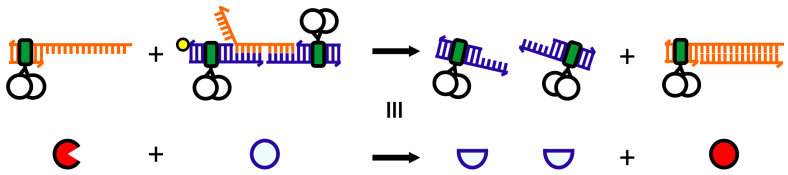

Figure 4.2: Structures and interactions of the assembler and of the shuttle carrying the disassembly signal. The assembler has two sections, each containing a zinc-finger binding site and a single stranded overhang (blue). These sections are linked by a complementary strand (orange). An additional toe-hold in this strand allows it to be stripped off by the signal strand (orange). The biotin anchorage on the assembler is indicated by a yellow circle.

To disassemble asters, the assembler was re-designed to be cleavable in response to a DNA encoded signal. The assembler DNA design (see Figure 4.2) was split into two duplex halves, each containing a zinc finger binding site. These halves are shown in blue in Figure 4.2. They each contain a single stranded overhang which allows them to be linked by a single strand of DNA, orange in Figure 4.2. When both halves are together, the assembler can cross-link microtubules but if the linking strand is removed, the

two halves disassociate and the microtubules are no longer cross-linked. The linking strand is removed by toe-hold mediated strand exchange (Yurke et al. (2003)). The linking strand contains a single stranded overhang which is free to interact with a complementary strand. If the interacting, stripping strand is not just complementary to the toehold region but also to the region linking the two blue halves, fully complementary to the orange strand, it will strip it off from the blue halves. With nothing linking the two halves, they disassociate. Thus the assembler will be cleaved in response to an interacting strand. This interacting strand is carried by a shuttle, orange in Figure 4.2. With these components, the complete scheme in Figure 4.1 is realised. Asters are formed with the cleavable assembler (light blue circles) and can be disassembled with addition of the disassembly shuttle (red 'pac-man'). The shuttle carries the stripping strand along the aster microtubules to the assemblers at the aster centre. The strand strips the linking strand from the assembler halves, splitting the assembler in half (blue half circles). The cross-links holding the aster together are terminated and the constituent microtubules disperse into solution. In principle, fresh assemblers could now re-organise the microtubules back into asters and the system could be cycled.

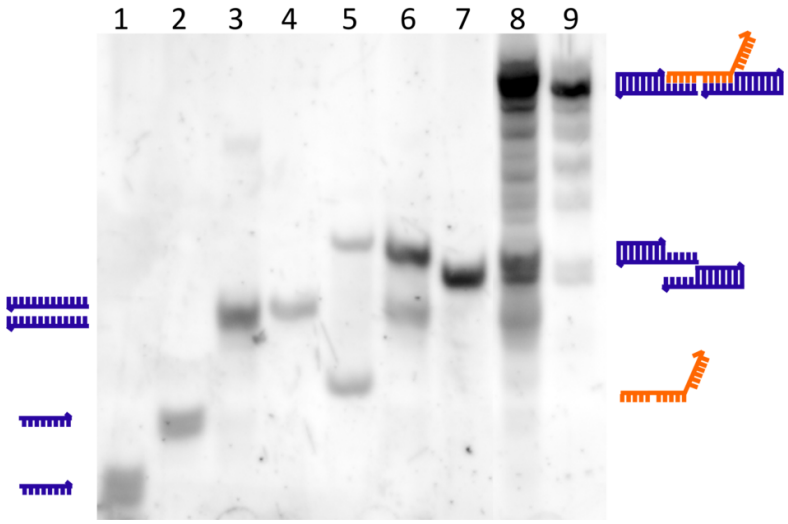

Figure 4.3: Native 15% 29:1 polyacrylamide gel of the duplex cleavable assembler and various combinations of its constituent strands - shown schematically. Lanes 1,2,3,4 and 5 contain the constituent strands of the assembler A2b1a, A2b1b, A2b2, A2b3, A2b4 respectively (outlined in Appendix B B.1.3). Lanes 6 and 7 contain assembler halves A2b1a+A2b2 and A2b1b+A2b3 respectively. Lane 8 contains the complete assembler and Lane 9 contains the same but PAGE purified. Final lane has been PAGE purified. The gel was stained with SYBR^{TM}gold.

4.1.1 Duplex Design

The DNA for the cleavable assembler described consists of five strands (sequences in Appendix B B.1.3). The formation of the assembler was tested by native PAGE (Figure 4.3). The individual strands which make up the assembler, as well as interacting combinations of strands were run in different lanes in the gel. A band corresponding to the assembler can be seen in the correct lane, but this lane also contains many other bands. These bands correspond to various partially formed assemblers. It is very difficult to mix the strands in exactly the correct ratio - due to small pipetting errors or inaccuracy in measurements of the DNA concentration, allowing complexes

to form without all five strands.

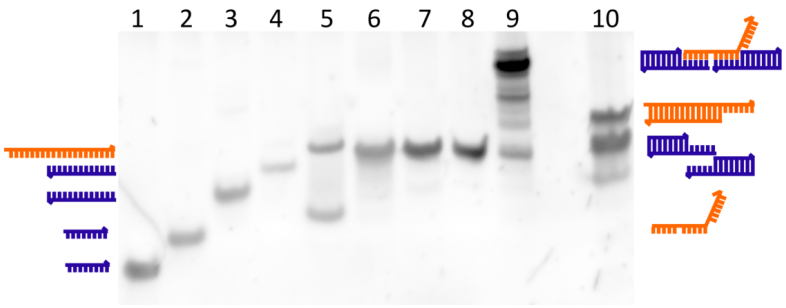

Figure 4.4: Native 15% 29:1 polyacrylamide gel of the duplex cleavable assembler and various combinations of its constituent parts - shown schematically, with the addition of the breaking strand. Lanes 1-5 are the same as Figure 4.3, with the breaking strand in lane 6. The assembler halves and complete assembler are in Lanes 7-9 respectively. The assembler with the breaking strand is lane 10. The gel was stained with SYBR^{TM}gold.

Despite impurities, the cleavable assembler was tested with the stripping strand in a gel. Figure 4.4 shows a similar gel to Figure 4.3 but the stripping strand has been added to the complete assembler in the final lane. The assembler band is gone from this lane and only the two halves of the assembler and the stripping-linker complex remain.

Despite the assembler being slightly contaminated by other structures, its aster forming capacity was tested. A kinesin titration gel was run and it was found to bind in the expected ratio, although the bands were not clean and smeared, shown in Figure 4.5. It was used in a gliding assay and was found to sustain normal gliding. It was also found to readily form asters, although less well than the regular assembler. Partially formed assembler structures reduce the number of completely formed assemblers which can bind to two

kinesins, which may be slightly hindering aster formation. Assemblers were PAGE purified to remove the partially formed structures.

4.1.2 PAGE purification

Aside from a purely analytical tool, PAGE can be used for purification. Mixtures of molecules are separated out into discrete bands by gel electrophoresis. Bands containing desired molecules can be cut from the gel and then soaked in buffer, allowing the molecule to diffuse into solution, out of the gel. The cleavable assembler was PAGE purified to remove partially formed structures (full protocol in Appendix A Section A.6.3). A sample of assembler was prepared (at a concentration ∼100 times that used in an analytical gel) and run in all lanes in a gel. The gel was imaged using UV shadowing in a transilluminator. It was placed over an UV fluorescent plate, under an UV lamp and a series of dark bands were observed due to DNA absorption of UV light. The band corresponding to the assembler was known from previous gels and cut out. It was soaked in buffer over night and the gel removed by centrifugation in a spin column. Purified assembler was obtained with ∼50% yield.

The purified assembler was tested by gel. It was run alongside the unpurified assembler in a DNA gel Figure 4.3 and was also run in a protein

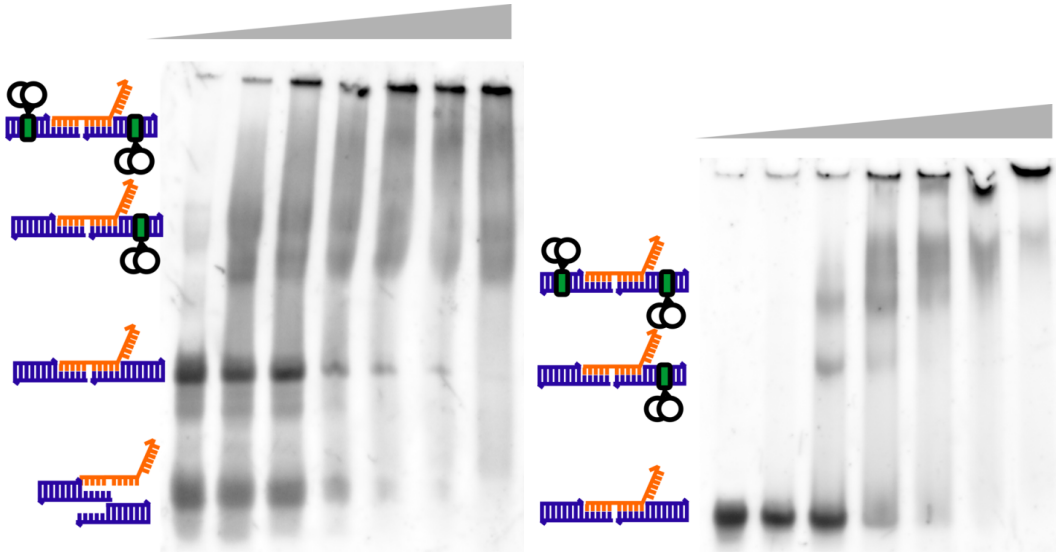

Figure 4.5: Native 7% 74:1 polyacrylamide gels, stained with SYBR™, of the duplex cleavable assembler DNA (0.25μM), un-purified (left) and purified (right), with increasing concentrations of kinesin (0 μM, 0.5μM ,1μM, 1.25μM , 1.5μM, 2μM, 2.5μM).

gel. The assembler band in the DNA gel was much cleaner. Figure 4.5 shows a protein gel with the purified and un-purified assembler. The bands are also much cleaner with the purified assembler. It was used in an aster assay but it was unclear if asters formed with an increased yield relative to pre-purification.

4.1.3 Hairpin Design

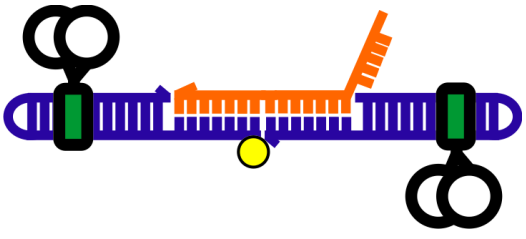

Figure 4.6: Schematic of the hairpin cleavable assembler. Colours similar to Figure 4.2.

An assembler construct was also designed which used DNA hairpins to reduce the number of strands. With fewer strands, the structure is much more likely to form correctly as there is less chance of incorrect stoichiometry. DNA hairpins are self interacting strands of DNA which fold-up on themselves. They contain a loop of unbound single stranded DNA, called a hairpin loop, held by duplex DNA. Figure 4.6 shows the hairpin assembler. The two linked halves, which before consisted of duplexes were replaced with hairpins. This assembler is shown on a gel and clearly forms a much cleaner band. This assembler was also found to form asters with a similar yield to the purified duplex assembler. The biotin on this assembler could not be located at the end of the duplex as in Figure 4.2 and was placed near the join between halves, shown in Figure 4.6. This impeded binding to the surface and so this construct was not used.

4.2 Microscopy Data

Fluorescence microscopy data of asters disassembling in response to a signal is shown in Figures 4.8, 4.9 and 4.11. Microtubules were labelled with rhodamine and are white in the micrographs. They were mixed with assemblers (without PAGE purification) and ATP, and placed in a streptavidin coated flow chamber as with the regular assembler. Shuttles carrying the

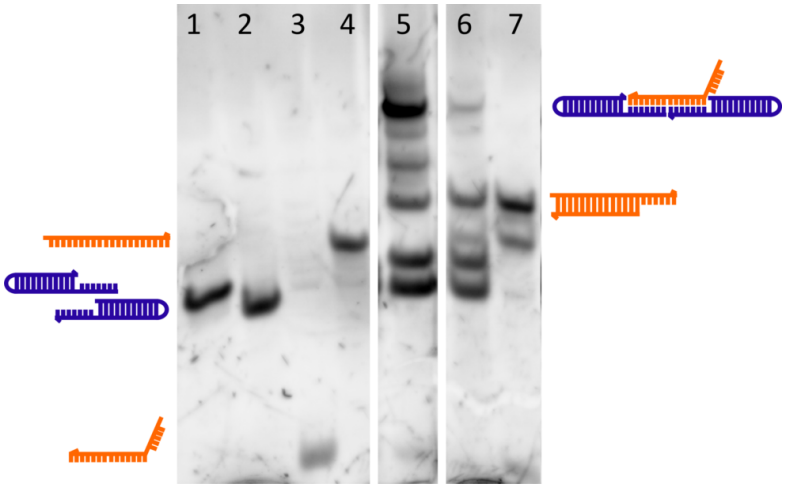

Figure 4.7: Native 15% 29:1 polyacrylamide gel of the duplex cleavable assembler and various combinations of its constituent parts - shown schematically, with the addition of the breaking strand. Lanes 1 and 2 contain the assembler halves and lane 3 contains the linking strand. The breaking strand is in lane 4. The complete assembler is in lane 5 and in lane 6 with the addition of the breaking strand. The spent duplex of breaking and linking strand is in lane 7. The gel was stained with SYBR^{TM}gold. Some lanes of the gel were removed as they were not relevant to these experiments.

disassembly signal were added and the aster disassembles. In Figure 4.8 the constituent microtubules are visible as they disassociate from the aster.

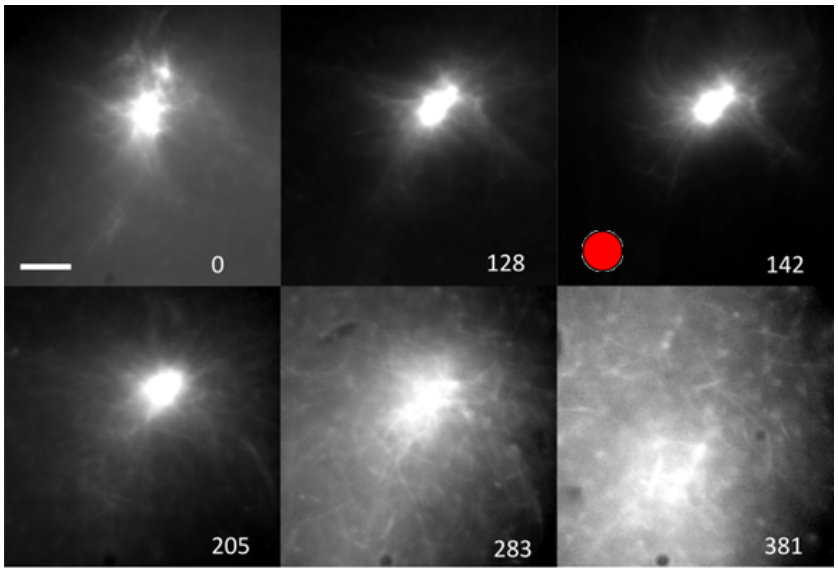

Figure 4.8: Fluorescence microscopy data of an aster breaking apart in response to a transported signal. The time in seconds is marked in the bottom right in each frame. Rhodamine labelled microtubules are in white. DNA signal is added at the red marker. Scale bar is 10μm.

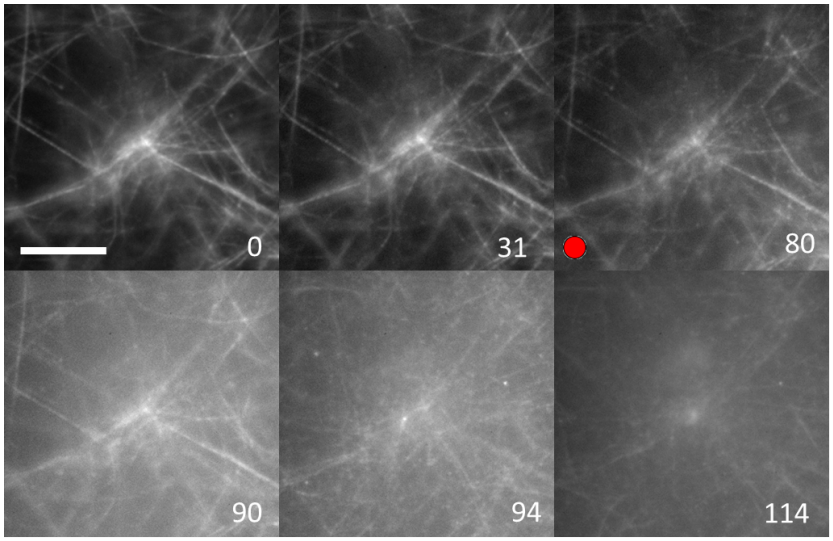

Figure 4.9: Further fluorescence microscopy data of an aster breaking apart in response to a transported signal. The time in seconds is marked in the bottom right in each frame. Rhodamine labelled microtubules are in white. DNA signal is added at the red marker. Scale bar is 10μm.

4.2.1 Radius of gyration

As a metric for aster disassembly, the aster radius of gyration was plotted as a function of time (see Chapter 2 Section 2.10.1 for a description of calculating aster radius of gyration). As the aster is destroyed, the radius should increase until it encompasses the entire field of view. Figure 4.10 shows a plot of radius of gyration for the microscopy data in Figure 4.8. The trace is a good representation of the behaviour observed in the fluorescence micrographs. The radius decreases as the aster continues to condense by the action of the assemblers. The condensing stops after the disassembly signal is added and then after ∼100s the radius increases sharply as the aster disassembles. It saturates as disassembly completes and microtubules fill the field of view.

Not all experiments behave in this way. Owing to the destructive nature of the experiment, microscopy of disassembly was often difficult as parts of semi-destroyed asters drift in and out of focus. This causes large quantities of noise in the traces for those asters which do not break apart cleanly and so these traces are not shown.

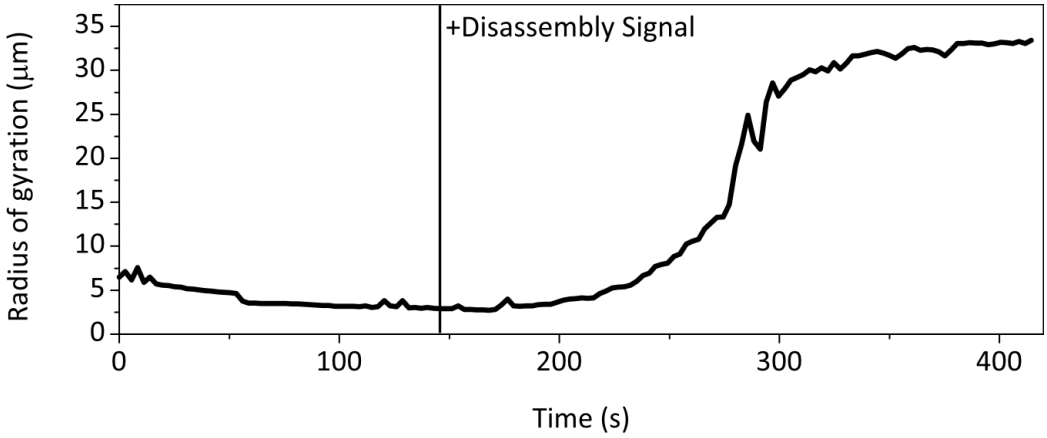

Figure 4.10: Radius of gyration of the aster plotted over time, increasing rapidly as the aster is destroyed.

4.3 Delivery of the wrong signal

In control experiments, shuttles carrying the wrong DNA signal were added to asters formed from the cleaveable assembler. These shuttles carried DNA that was not complementary to the linker strand. As expected, asters did not disassemble in response to this signal.

4.4 Diffusive transport of the disassembly signal

The disassembly strand alone - without attachment to a kinesin shuttle - was added to asters formed from the cleavable assembler. This signal was much less effective than the actively transported signal. The results are summarised in Figure 4.11. Eight actively transported disassembly experiments and six diffusively transported disassembly experiments are shown. Signs of disassembly were seen in six of the active experiments but only two of the diffusive. As with cargo release, diffusion is much less effective than active transport in bringing signals into the centre of the aster.

4.5 Conclusion

A modified assembler was designed which could split in response to a DNA encoded signal. Splitting the construct separates the kinesins, interrupting microtubule cross-linking and destroying asters. The assembler was tested with PAGE and found to contain misformed assemblers caused by incorrect stoichiometry of its component strands. This contamination did not impede the assembler from forming asters. Asters formed using this assembler were immobilised in flow chambers and their response to the disassembly signal

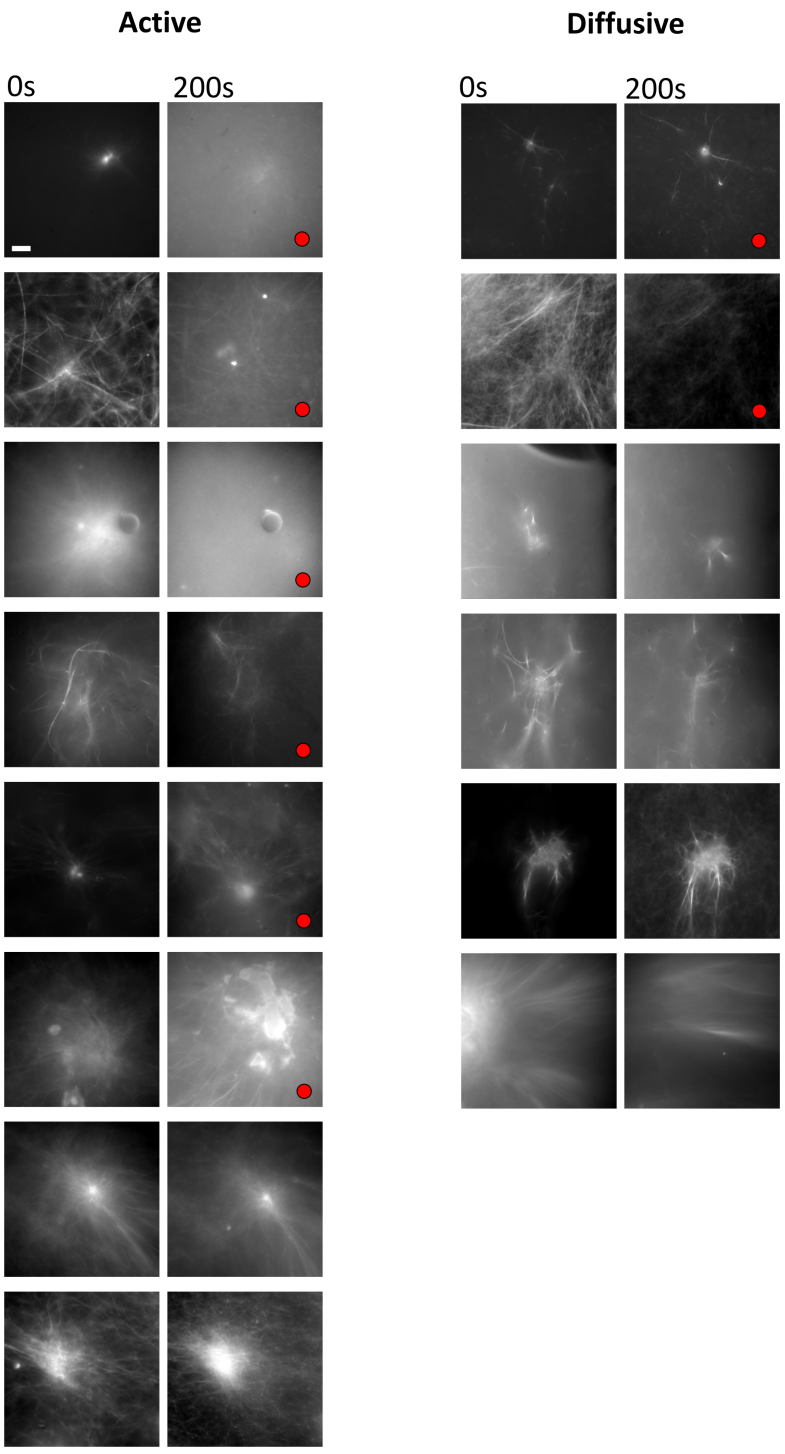

Figure 4.11: Summary of disassembly experiments fluorescence micrographs just as the disassembly signal is added (t=0s) and after 200s for actively transported signal and diffusively transported signal. Asters have mostly disassembled by 200s with the actively transported signal but not with the diffusive. Those which disassemble have been indicated with a red dot. Scale bar 10μM

tested. When the signal was actively transported, they were found to readily disassembly but with diffusive delivery, disassembly occurred in only a minority of asters. Again, active transport is required for effective delivery of the signal.

The extension of the aster-based transport system to allow DNA encoded signals to interrupt the track network itself, rather than just cargo transported on it, represents a significant advance to the functionality of the system. In theory, it allows for complete recycling. Not only can the cargo be cycled through concentration and release but following this, the track network itself could be dismantled, back into its constituent microtubules. Such functionality could allow for an adaptive system, re-organising itself into different devices in response to signals.

Chapter 5

Single Molecule Transport

In Chapter 3 Section 3 bulk transport by shuttles was investigated and characterised. In this Chapter, complementary single-molecule measurements are presented. Fluorescently labelled shuttles were observed moving on unorganised microtubules. The shuttles required a different label for these experiments, a quantum dot (QD). This labelling required purification. Monofunctionalised QDs were purified from multi-functionalised QDs using ion exchange. Three different methods for tracking moving shuttles were investigated: by hand, Gaussian tracking and kymography. The latter was chosen and used to characterise the assembler and a shuttle.

The single molecule assay developed was extended to investigate the min-

imal motor unit. A truncated single headed version of the zinc finger kinesin fusion protein was used and linked in teams of up to 12 motors to investigate their dynamics. Five heads were required for sustained movement and the optimal number of heads was eight. These findings are discussed in terms of other minimal motor studies.

DNA used in this chapter was designed by Dr Helen Carstairs and she also developed the QD mono-functionalisation protocol. The QD assay was a modified version of that developed by Dr Helen Carstairs.

5.1 Labelling the shuttle

The shuttle used in Chapter 3 Section 3 is labelled with Cy3. A different fluorescent label was used for the single-molecule experiments. Quantum Dots (QDs) have advantages over fluorophores as they are significantly brighter and far less prone to photo-bleaching. Cy3 was bright enough for bulk experiments but not for single-molecule experiments. Although an oxygen scavenging system was used to prevent photo-bleaching, it cannot be completely avoided. If a fluorophore-labelled shuttle bleaches midway through its trajectory along the microtubule, it is indistinguishable from a shuttle which has fallen off the microtubule, leading to artificially decreased measured run lengths. Quantum Dots with emission at 655nm coated with strep-

tavidin were used (Invitrogen) and conjugated to biotinylated DNA. Each QD is coated with multiple streptavidin molecules and, as streptavidin is a tetramer, QDs will be multi-functionalised with biotinylated DNA. A high ratio of QDs to DNA would ensure that there were very few multi-functionalised QDs. This would lead to a large population of unlabelled QDs which would add background fluorescence. In the presence of a heterogeneous population of QDs, it would also be unclear which population of QDs were moving; it might only be the few multifunctionalised QDs. Thus for experiments where the effect of motor number is unclear, as with the minimal motor unit, it was necessary to insure that the QDs were mono-functionalised with DNA.

5.1.1 QD Monofunctionalisation

Mono-functionalised QD-DNA conjugates can be purified by ion exchange using diethylaminoethyl (DEAE) Sepharose-packed spin columns (Carstairs et al. (2009)). The full protocol is outlined in Appendix A Section A.12. QDs and biotinylated DNA were mixed at a 1:1 ratio and incubated for half an hour. This mixture was added to the equilibrated spin column and washed with a low salt (NaCl) buffer to remove unbound QDs. The column was washed with buffer containing increasing concentrations of salt, collecting a fraction each time, until the desired QD-DNA conjugate had eluted.

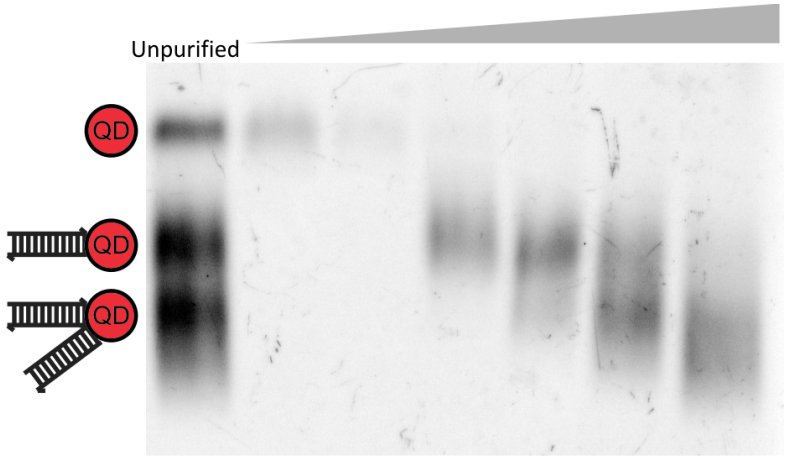

Figure 5.1: Agarose gel of QD-DNA samples. Salt Concentrations.

The QD fractions can be placed under a trans-illuminator and the amount of fluorescence assessed to determine the relative concentration of QDs in the fraction. These fractions can be run on an agarose gel to determine if mono-functionalisation has been successful. Figure 5.1 shows an agarose gel imaged using the QD emission. In the unpurified sample, a mix of unlabelled, mono-functionalised, bi-functionalised and multi-functionalised QDs can be seen. The subsequent lanes contain increasing salt concentration, with mono and bifunctionalised bands separated in different lanes. Once the salt concentration to mono or bi-functionalise a particular QD-DNA conjugate is known, the purification can be completed without running a gel. In this way mono and bi-functionalised QD-DNA conjugates using different DNA strands were obtained.

5.2 Single-molecule Assay

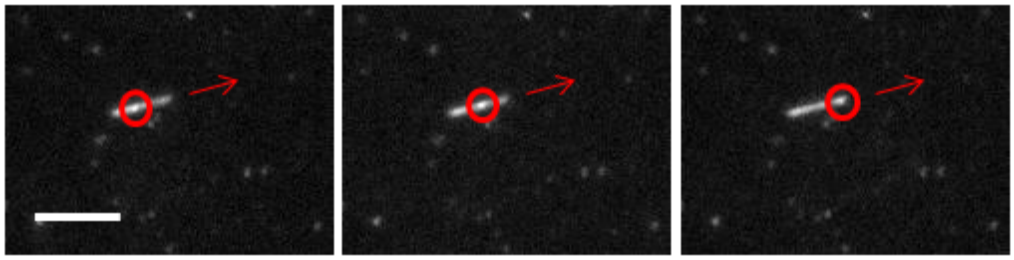

Figure 5.2: Time series of fluorescent micrographs showing a QD labelled shuttle moving along a microtubule over 6s. Scale bar 10μm.

This assay is described as single-molecule to differentiate it from the bulk transport of cargo observed on asters although it does not involve observing single fluorophore molecules but single quantum dots. The full protocol for the QD assay can be found in Appendix A Section A.13. QDs with 655nm emission were used with rhodamine-labelled microtubules. If the microtubules are not heavily labelled with fluorophore, the QDs and microtubules are both visible using the same filter cube - the QDs as bright dots on the long microtubule filaments - Figure 5.2 shows a QD labelled shuttle moving on a microtubule. QD-DNA conjugates were incubated with kinesin as described previously. Microtubules were immobilised on the surface of the simple flow chamber using tubulin antibody. BSA washes were used to prevent non-specific interaction between the microtubules and antibody and also between QD labelled shuttles and the surface. QD labelled shuttle solutions were diluted in imaging buffer and placed in the chamber. The chamber was

sealed and imaged immediately. Shuttles were observed binding to microtubules, moving and then dropping off. The number of moving shuttles was seen to decrease with time and after ∼15 minutes very few moving shuttles were seen. Experiments were temperature controlled by water baths connected to cooling collars on the objective and stage. All measurements taken at 23.5°C.

5.3 Analysing Trajectories

Three different methods of analysing the shuttle trajectories were investigated. Tracking was attempted by hand using Retrac to define the centre of each QD in each frame. Two different Matlab programs were used to fit 2D-Gaussian profiles to each QD in each frame, to determine the position and then stitch the positions together into trajectories. The shuttles were also tracked using kymography where the profile along a microtubule in a series of fluorescent images is plotted over time and the QD trajectory appears as a diagonal line. Different tracking methods were all applied to the same data; non mono-functionalised QD labelled assembler.

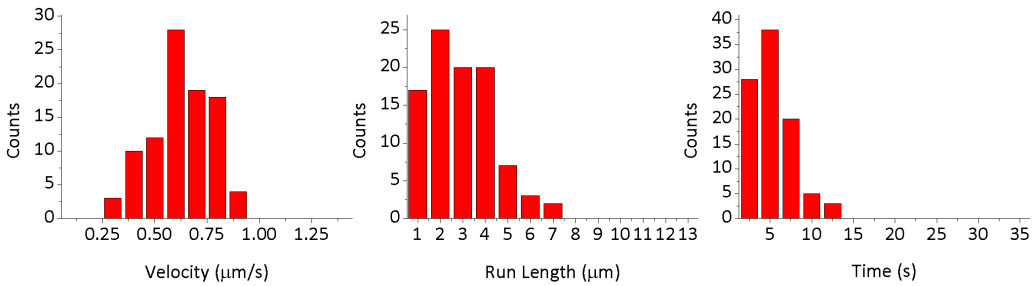

Figure 5.3: Velocity, run length and run time distributions for QD labelled assembler teams measured by hand using Retrac. Mean Velocity, run length and run time ± standard deviation are 0.6±0.1, 2.4±1.4, 4.2±2.5.

5.3.1 By Hand

QDs can be tracked using the same Retrac program used for tracking gliding assays. The centre of a moving QD was determined by eye and recorded at each frame. The position data obtained this way was fitted with a line of best fit and the velocity, run length and run time determined. This was repeated for ∼100 moving QDs for each sample. Tracking by hand, it is easy to determine moving QDs and any anomalies are easily found. However the process is laborious and time intensive. As the QDs to track are chosen manually there could be selection bias and there is a tendency to choose longer trajectories over very short ones. A summary of by-hand tracking data is shown in Figure 5.3. Short run lengths and times appear to be slightly under represented in the data as the run length distribution should decrease monotonically for longer run lengths as the motor has a probability of falling off at each step. It is also difficult to track very slow moving QDs

by hand as the QD does not move very far between frames. Over defining the QD position in this way leads to noise in the position data although appropriate smoothing can alleviate this.

5.3.2 Gaussian Tracking

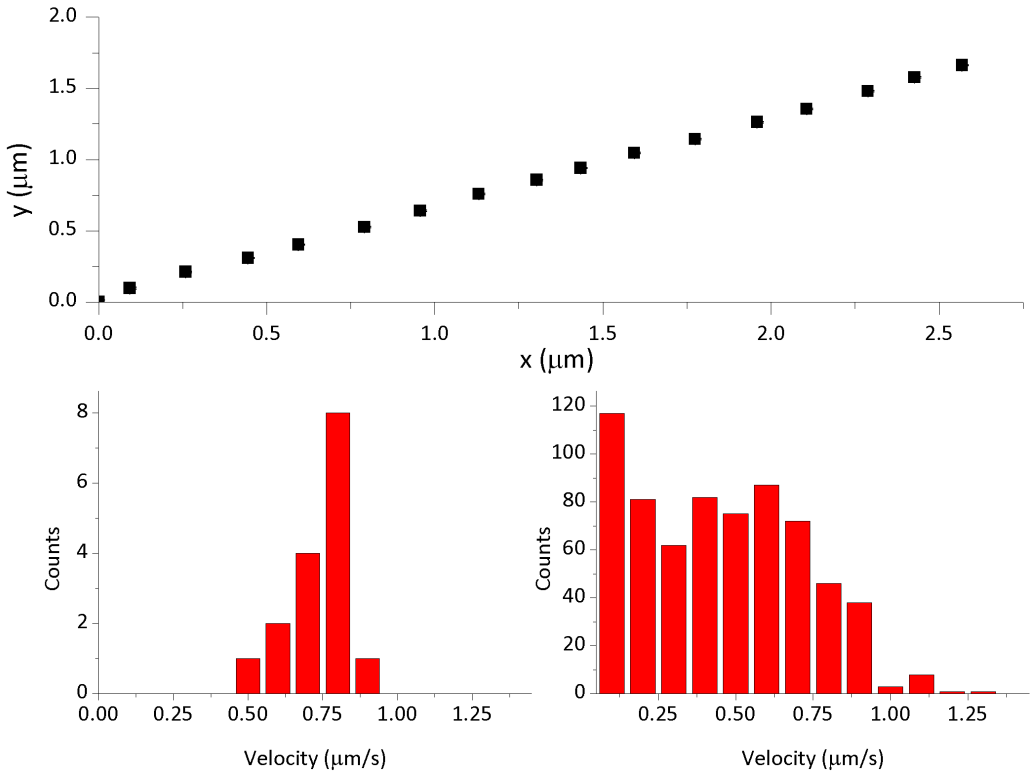

Figure 5.4: Top: QD trajectory (distance from starting co-ordinates) from the Fiesta programme for QD labelled assembler constructs. Bottom Left: Velocity distribution from the trajectory above. Bottom Right: Segment velocity distribution over all data. Mean Velocity ± standard deviation are 0.40±0.26.

Particle tracking software can fully automate tracking particles. Programs operate by finding all the bright spots (local maxima) in a frame and then fitting a 2D Gaussian to each one. The centre of the Gaussian defines the

particle's co-ordinates and can be determined with sub-pixel accuracy. This is repeated for each frame, generating a list of space and time co-ordinates. These are joined together based on estimates of the distance each particle can move between frames. A series of particle trajectories are then obtained. In theory this method is completely automated. For each QD, large amounts of data are obtained and very fine detail can be observed in this data, such as pausing or changes in velocity. The problems with Gaussian tracking are that the software often requires very high quality data. This can mean cleaning the data by passing it through a band pass filter or subtracting the first frame to remove the background. In the data obtained from this assay, there are often >100 QDs in each frame and 1000 frames taken. The software can have problems with this many particles, particularly when stitching together co-ordinates into trajectories. This can be alleviated by cropping each frame into smaller subframes but then requires more user input. These programs will indiscriminately track any bright spot in frame so fluorescent contaminants are sometimes mistakenly tracked and the data recorded as a QD trajectory. Stationary QDs, not necessarily bound to a microtubule (possibly non-specifically bound to the surface) are also tracked. Despite indiscriminately tracking bright particles, some moving QDs can be missed by the software - QD brightness is highly variable - and so some data is lost. Finally the creation of trajectories from the co-ordinates is prone to error.

The software can miss a particle for several frames and then erroneously split what should be a continuous trajectory into multiple parts.

Two tracking programs were tested. The first was a Matlab implementation of the algorithms of Crocker and Grier (1996) and the second was a more polished tracking suite (also written in Matlab) called FIESTA and created by Ruhnow et al. (2011), specifically for work with kinesin so it can also track moving microtubule filaments. Although the first program allowed more control through access to the source code, it crashed when dealing with many QDs as it could not create trajectories from the high quantity of position data. FIESTA was much better and data from a sample QD is shown in Figure 5.4 top. The position of the QD was determined very precisely and slight variations in the particles motion are observable. The velocity distribution for this trajectory is shown in Figure 5.4 bottom left.

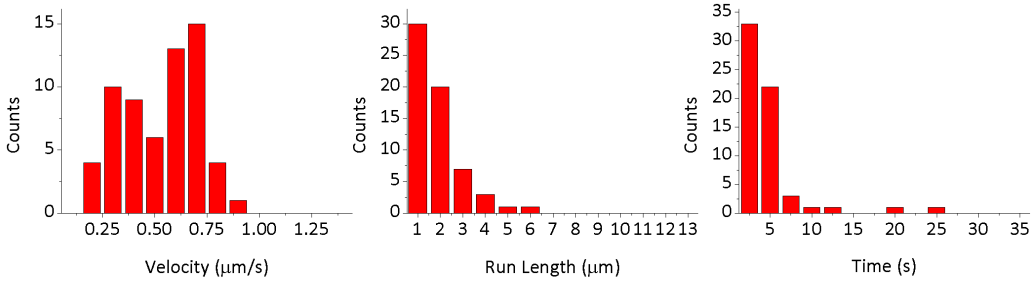

Figure 5.5: Velocity, run length and run time distributions for QD labelled assembler teams measured by tracking Gaussian intensity profiles with the Fiesta programme. Mean Velocity, run length and run time ± standard deviation are 0.48±0.18, 1.35±0.98, 3.30±3.83.

5.3.3 Kymography

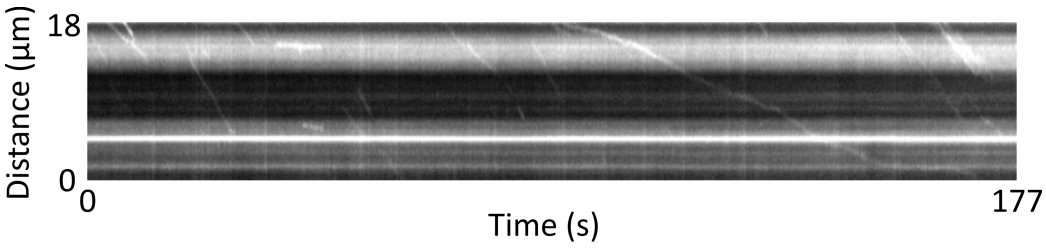

Figure 5.6: Kymograph of the QD labelled assembler team.

The third method of QD tracking investigated was kymography. An example kymograph is shown in Figure 5.6. Starting from a time series stack of images of QDs moving on microtubules, a line was drawn along a microtubule of interest. The fluorescence intensity along that line is plotted for each frame. These plots are used to generate a pseudo-image with distance along one axis and time along the other. QD trajectories appear as diagonal lines in this image. This tracking method was used by Derr et al. (2012) and Furuta et al. (2012) for tracking teams of motors moving on microtubules. The advantage of this method is that it is not as labour intensive as tracking by hand or even using Gaussian tracking once the necessary cleaning of the data is taken into account. Large amounts of data can be obtained and in theory every moving QD can be measured if every microtubule is sampled. The only problem with kymography is that it measures an averaged trajectory and so the finer details of the QDs behaviour are missed.

5.3.4 Comparing Tracking Data

Data from tracking by hand, with Gaussian tracking and by kymography are shown in Figure 5.3, Figure 5.5 and Figure 5.8. Comparing the data, tracking by hand gives a narrow spread of velocities - possibly an artefact - although the mean velocity is consistent between all different tracking methods. The Gaussian tracking velocity is slightly lower and the mean run length much lower. The lower velocity is probably caused by the software continuing to track QDs which have become stuck. This is supported by the zero velocity peak in the segment velocity distribution in Figure 5.4. This probably explains the strange QD velocity distribution for Gaussian tracking (Figure 5.5). The shorter run length may be due to splitting trajectories but may also be because the software is better at recording very short run lengths. Both the kymography data and the hand tracking data under represent short trajectories. For kymography, this is because short trajectories appear as dots rather than lines on the kymograph and so are untrackable. The kymography velocity distribution is a reasonable Gaussian. Kymography was chosen as the preferred tracking method as large amounts of data could be collected easily and it samples the population almost completely, except for some very short trajectories.

5.3.5 Defining uncertainty in kymography

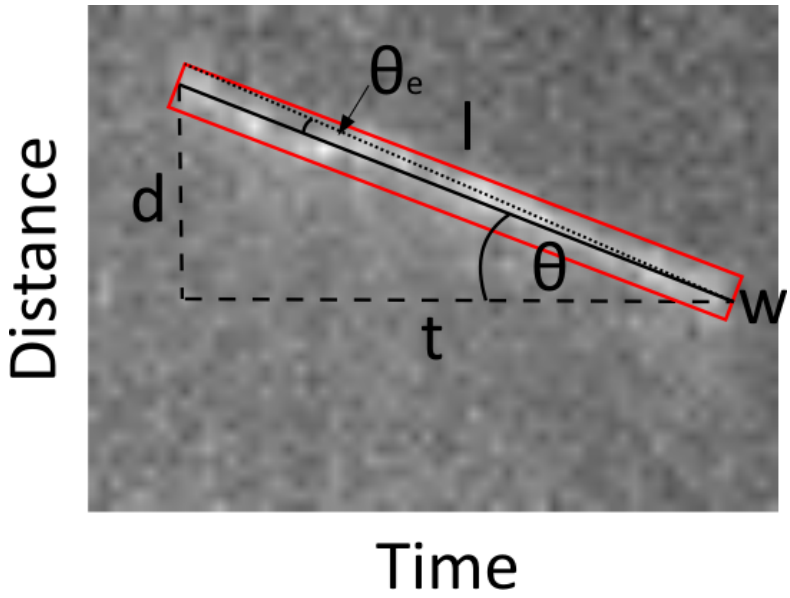

Figure 5.7: Kymograph of the QD labelled assembler team, labelled with a red box defining the measurement uncertainty. d is the run length of the quantum dot, t is the run time, θ is the angle between such that $\tan\theta = v$ the velocity, w is the full width half maximum of the QD trajectory, l is the length of the trajectory and θ_e is the uncertainty in the angle.

The uncertainty in estimating the line of best fit of a kymograph was determined. Figure 5.7 shows an example QD trajectory labelled with various properties: d is the run length of the quantum dot, t is the run time, l is the length of the trajectory, θ is the angle between l and t - such that $\tan\theta = v$ the velocity, w is the full width half maximum (FWHM) of the QD trajectory and θ_e is the uncertainty in the angle. The FWHM was chosen as a measure of the uncertainty defining the line of best fit as it is easy to measure although it is probably an overestimate. The FWHM was measured for 10 trajectories with a mean of 2.7 pixels. The red box in the Figure 5.7

represents this uncertainty. The velocity of the moving QD is:

$$v = d/t = \tan\theta \tag{5.1}$$

thus the error angle, θ_e gives the error in the velocity:

$$v_e = \tan\theta_e = w/2l \tag{5.2}$$

The velocity error is inversely proportional to the total line length. For the line shown in Figure 5.7 the velocity ± error is 0.538±0.015μm/s. The mean error for double head shuttles is 0.023μm/s and 0.001μm/s for single head shuttles. These are both significantly less than the inter trajectory variation.

Error can also arise in velocity data from drift. Temperature fluctuation can cause the microscope sample to drift during imaging. As temperature control was used on the stage and objective, the sample was kept in equilibrium with its surroundings, minimising sample drift. Drift could easily be identified in the kymographs as slope in the background and QD trajectories corrected if necessary.

5.4 Kinesin Dimer Constructs

For comparison to bulk transport, the assembler and a shuttle variant were tested in the single-molecule assay. The assembler construct was the same construct used in Chapter 3 and the shuttle variant was the biotinylated construct used in Chapter 2 Section 2.6. The assembler was also mono-functionalised to determine whether mono-functionalised QD shuttles were impaired by the purification process.

5.4.1 Assembler

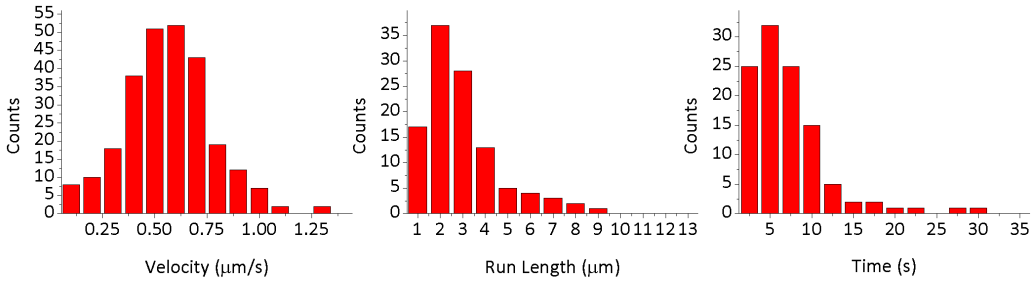

Figure 5.8: Velocity, run length and run time distributions for QD labelled assembler teams measured by kymograph analysis. Mean Velocity, run length and run time ± standard deviation are 0.53±0.27, 2.45±1.69, 5.68±5.29.

The assembler was conjugated to a QD and imaged moving on microtubules. The data was tracked using kymography. The velocity agrees with the gliding velocity for the double headed kinesin construct. The run length is quite long, with some trajectories as long as 9μm. Multiple dimers in a team increase the run length but leave the velocity unchanged Rogers et al. (2009);

Derr et al. (2012). The kinesins in the assembler construct are orientated to increase their likelihood of interacting with two microtubules rather than the same one. Thus the long run lengths are likely due to multi-functionalised QDs.

5.4.2 Shuttle

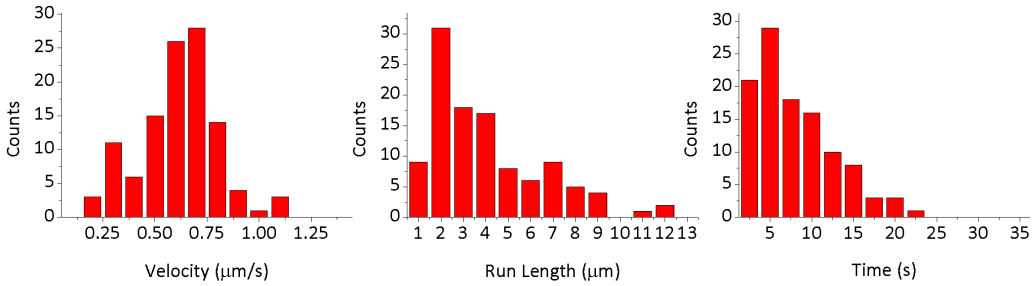

Figure 5.9: Velocity, run length and run time distributions for QD labelled shuttle teams measured by kymograph analysis. Mean Velocity, run length and run time ± standard deviation are 0.55±0.19, 3.55±2.49, 7.03±5.54.

A similar DNA construct to the shuttle, a biotinylated duplex with only one zinc finger binding site was conjugated to a QD and imaged moving on microtubules. The velocity distribution was similar to the assembler but also the run length distribution. If both assembler kinesins were interacting with the microtubule, the assembler should have longer run lengths than the shuttle. This indicates that either both assembler kinesins are prevented from interacting with the microtubule or that the effects of multi-functionalised QDs dominate.

5.4.3 Mono-functionalised Assembler

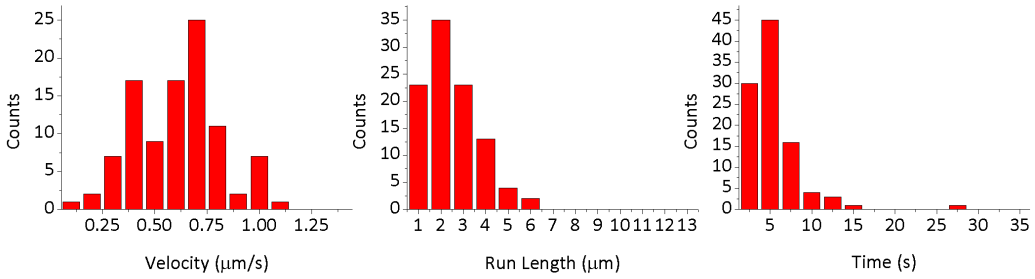

Figure 5.10: Velocity, run length and run time distributions for monofunctionalised QD labelled assembler teams measured by kymograph analysis. Mean Velocity, run length and run time ± standard deviation are 0.55±0.21, 1.96±1.13, 4.12±3.40.

The assembler-QD conjugate was mono-functionalised as described above and imaged moving on microtubules. >100 QDs were observed moving indicating that mono-functionalisation does not damage the QD-DNA conjugates or impede motion. The velocity was the same for the shuttle and non mono-functionalised assembler as expected. The run length is much lower consistent with the fact that there are no multi-functionalised QDs in the sample.

5.5 Kinesin Single head

Single headed kinesin was investigated as this is the minimal functional motor unit. By understanding it, the mechanics of the whole protein may be elucidated. Single heads cannot sustain processive movement (Hancock and Howard (1998, 1999); Bieling et al. (2008); Kamei et al. (2005); Vale et al.

(1996)) although some movement has been observed (Inoue et al. (2001)), see Chapter 1 1.2.9. Questions remain about number of heads needed for movement: Hancock and Howard (1998) suggested 4-6 from fitting to the landing rate on single head coated surfaces but Kamei et al. (2005) found two moved in an optical trap. Kamei et al. (2005) recorded velocities were much higher than their measured gliding velocity. They attribute this to crowding in the gliding assay but Hancock and Howard (1998) performed low density gliding assays and should have found high velocities at low density if Kamei et al. (2005) are correct. No density dependence on velocity was found. Miyazono et al. (2009) saw some restoration of velocity using covalently linked DNA to dimerise two heads. This tight coupling may partially re-establish inter head communication. To resolve the discrepancy between these studies, QD assays were performed using teams of single heads attached to DNA.

5.5.1 Single Head Construct

The single head construct consisted of the first 345 amino acids of rat kinesin 1 bound to the same zinc finger protein as the double head construct. It was also designed by Dr Junichiro Yajima. This contains the head, neck linker and a small amount of coiled coil but not enough to dimerise. Five glycine residues were also included between the neck and zinc finger to improve

protein solubility. Details of the design, expression and purification of the protein are in Appendix A Section A.2.

5.5.2 Gliding Assay

Gliding assays were performed with the single head construct bound to single binding site biotinylated DNA as Chapter 2 Section 2.6. The single head was found to support gliding of microtubules at $0.10 \pm 0.01 \mu$m/s at 23.5°C. This is in agreement with other single head gliding measurements (Hancock and Howard (1998)).

5.5.3 DNA Constructs

Teams of different numbers of single heads were linked together on DNA constructs designed by Dr Helen Carstairs. These DNA constructs are similar to those used for the assembler, full sequences in Appendix B Section B.1.4. There are 5 base pairs at either end of the duplex to stabilise the ends and then varying numbers of zinc finger binding sites with 2 bases between each one. The binding sites are on an 11 base pair repeat, slightly larger than the 10.5 base pairs per turn of a DNA duplex (Drew and Wing (1981)). This means with successive binding sites, each motor will be slightly twisted to the previous one, limiting the number of motors which can be placed on a single

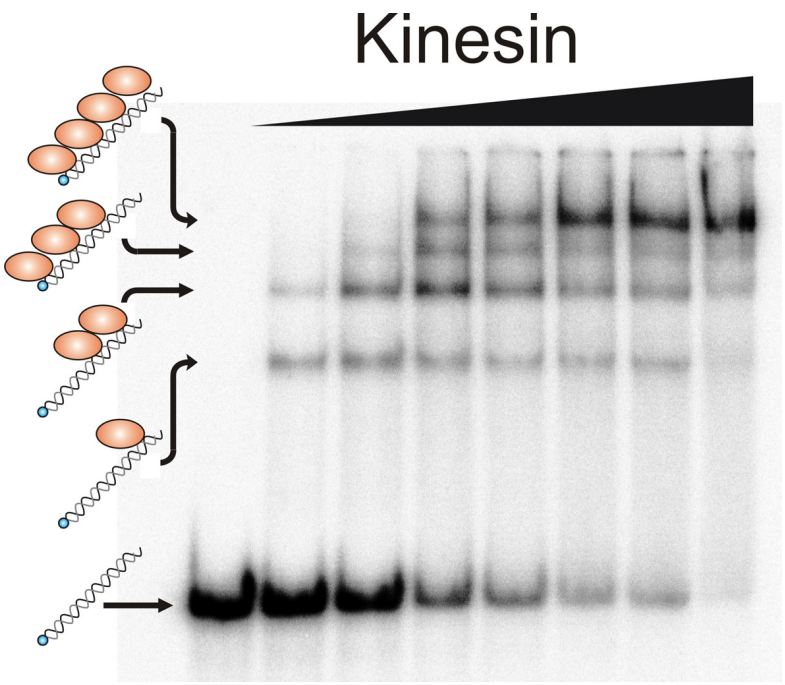

Figure 5.11: Binding assay of zinc finger with DNA duplex containing four binding sites from Carstairs (2008). 7% 74:1 Native TAE acrylamide gel. The DNA is radio-labelled with 32P. The volume and concentration of DNA in each lane is identical (1l of 40pM) and the concentration of protein increases from left to right (0, 0.08, 0.2, 0.5, 1, 2.5, 5, 40nM). This leads to an excess of protein from 2 to 1000 times.

duplex and still all interact with the same microtubule. Extra base pairs could be added to correct for the twist but this would break the periodicity and gaps between motors might effect their behaviour. Zinc fingers can bend DNA (Sjø ttem et al. (1997)) and it is unclear what effect the zinc finger used here is having on the DNA. The more motors attached to the DNA the greater the potential bending. Taking into account the effects of DNA bending and the twist between motors, the maximum number of motors attached to a single duplex was six. Any more heads than this and some may be prevented from binding by the binding or the twist between heads

(between two heads is 11/10.5∼5% and then ∼30% between the first and last head on a team of 6). Figure 5.11 shows a gel from Carstairs (2008) with a DNA duplex containing four binding sites and increasing concentration of single headed kinesin. With adequate kinesin concentration, four kinesins can bind to the DNA.

To link more than 6 motors together, QDs were bifunctionalised using the same protocol for mono-functionalisation but using higher salt concentrations to isolate bifunctional QDs. It was harder to isolate these QDs so there may be contamination with other multi-functionalised QDs in these samples. Longer DNA duplexes were also harder to purify. These QD-DNA complexes stuck in the column so that good separation between functionalised QDs was difficult.

Four DNA constructs were used to investigate teams of single heads, with 3, 4, 5 and 6 binding sites. By bi-functionalising these constructs, teams of up to 12 heads were investigated. The effects of geometry were also investigated by comparing 6 heads on a single duplex and bi-functionalised, 3 binding site constructs.

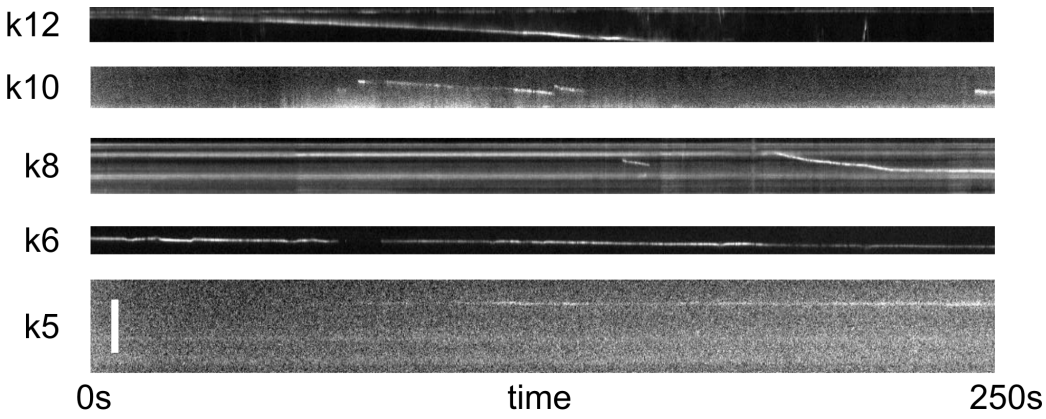

Figure 5.12: Example kymographs for single head teams with 5-12 heads (k5-12). Scale bar 10μm. Time in seconds indicated.

5.5.4 Single-molecule Assays

Single-molecule assay performed were performed as described in Section 5 for teams of single heads tracked using kymography. No movement was seen for teams of 4 heads but with 5 heads, very slow movement was observed (2.0±1.7nm/s). Higher velocities were observed with more heads, the results are summarised in Figure 5.13 with example kymographs in Figure 5.12 and complete histograms are given in Figure 5.14. Most teams were slow and stayed on the microtubule too long for run length to be measured except for 8 and 10 heads. Run length histograms for these teams are shown in Figure 5.15.

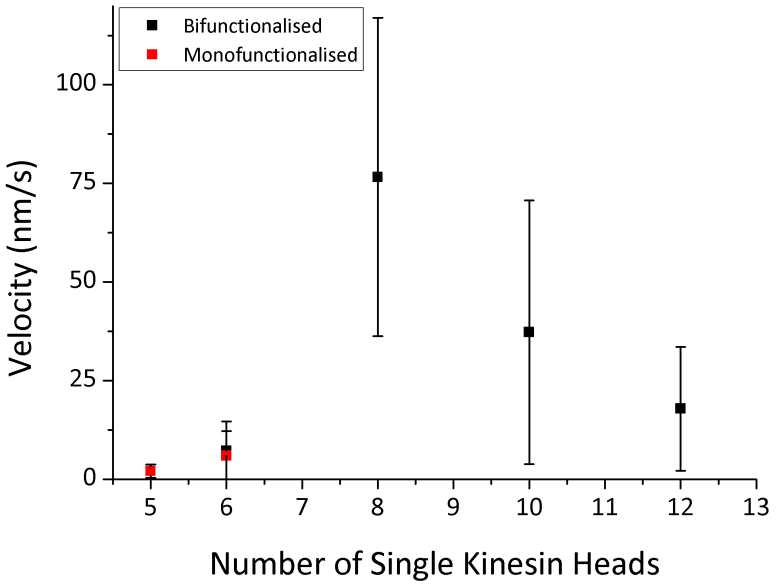

Figure 5.13: Velocity for single head teams with different number of heads. Bi-functionalised teams are plotted in black and mono-functionalised in red. The error bars used were the standard deviation of the data.

Velocity vs. Number of heads

The velocity for each team is plotted against number of heads in Figure 5.13. 5 and 6 head teams were found to be very slow but a dramatic increase in speed was observed for 8 heads. This increase dropped steadily for 10 and 12 heads but remained much higher than <8. The extremely slow velocity for the 5 and 6 head teams meant that kymographs had to be compressed by a factor of 5 in time to be measured. The mono-functionalised and bi-functionalised 6 headed teams gave very similar results. The effects of geometry on velocity are discussed in Section 5.5.5.

The velocity distributions are shown in Figure 5.14. All distributions have a large spread of velocities and all have a long, high-velocity tail. The

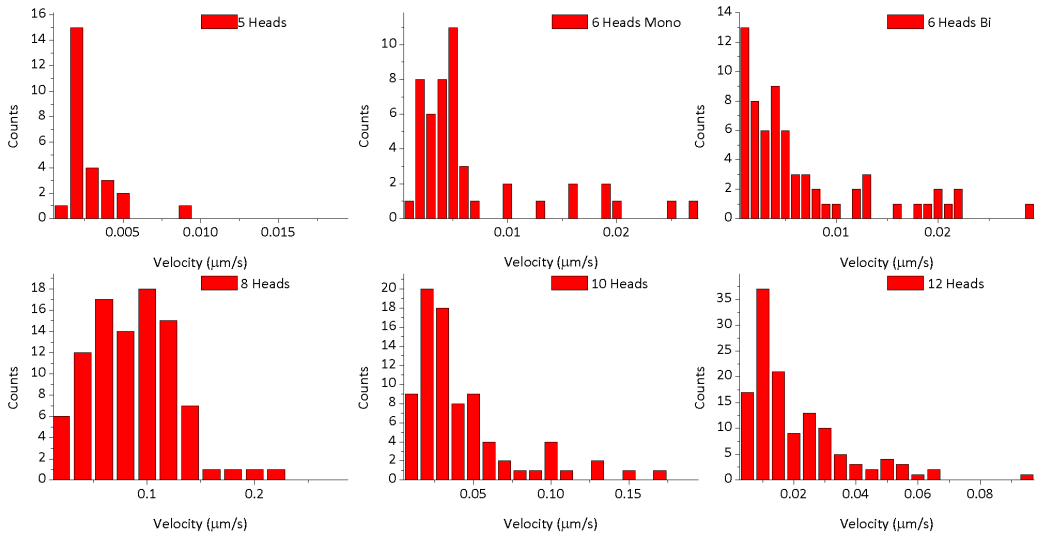

Figure 5.14: Velocity distributions for different numbers of kinesin heads.

kymograph trajectories (examples in Figure 5.12) appear relatively smooth so the spread in velocity and variation between teams, at least partially, represents some real differences between teams. Differences in the local environment such as the condition of the microtubule or presence of obstacles (such as stuck teams) may account for some of the variation. The geometry with which the team binds may also have a continuing effect on the velocity. This is discussed further in Section 5.5.5.

It is possible that the high velocity tail is caused by problems with the mono-functionalisation of the QDs. Multi-functionalised QDs with more heads could be contaminating the sample and contributing higher velocity trajectories. Although from the observed relationship between velocity and number of heads this could only be true for the 5 and 6 head teams as the

velocity is maximal for teams of 8. Inoue et al. (2001) analysed trajectories from individual single head constructs. The mean movement from their constructs was very low but they also observed long tails in their instantaneous velocity distributions, extending up to 600nm/s.

Run Length

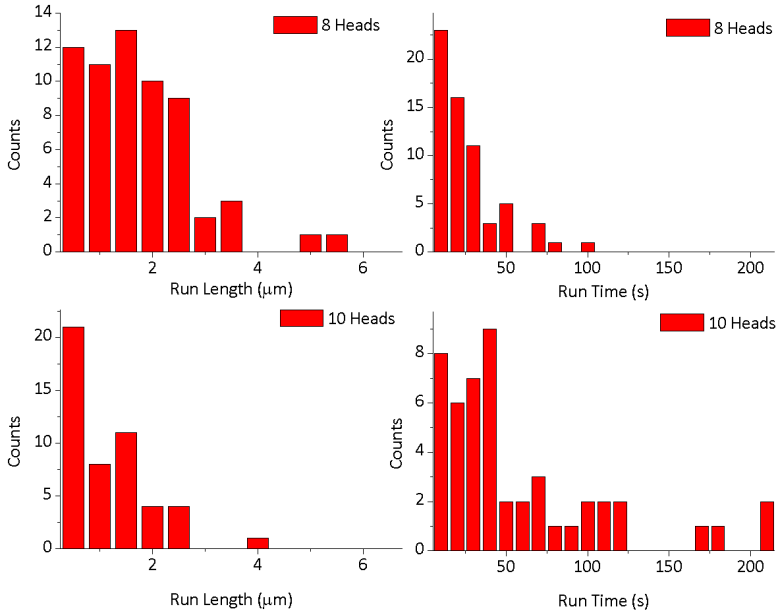

Figure 5.15: Run length and run time distributions for different numbers of kinesin heads.

Run lengths were only measured for complete trajectories where both the start and end were observed. This may truncate measures of run length and run time to within the imaging time of ∼300s. The run length was only measurable for teams of 8 and 10 heads as all other teams remained bound to the microtubule for sufficiently long times that there were very few complete

trajectories observed. The results are summarised in Figure 5.15.

The run length and run time distributions for 8 and 10 heads looks similar distribution to the double head. It peaks at low run length and decreases as the likelihood of a team dropping off increases with time. The run length for 8 heads is long (1.5±1.3μm) , similar to a single kinesin dimer. Derr et al. (2012); Furuta et al. (2012) both observed steep increase in average run length for teams of dimers with increasing numbers of motors from 1.5μm with a single dimer to 5μm with 4 dimers. With single heads, the mean run length for 10 heads (0.84±0.80μm) is lower than for 8 heads. From the distribution, this appears to be caused by a large population of teams moving less than 0.5μm whereas 8 head teams are spread more evenly.

It is unclear whether the run length increases with increasing numbers of single heads in a team, as it does with dimers but there is clearly a relationship between team size and run time. For teams of dimers, more motors leads to longer run times as the probability of detachment decreases (Derr et al. (2012); Furuta et al. (2012)). With single heads, the run time is related to velocity with faster teams having shorter run times and slower teams remaining on the microtubule for a long time. Hancock and Howard (1998); Rice et al. (2003) predict that single heads will remain bound to the microtubule for a long time because there is no partner head accelerating detachment. The

single head attachment time is compounded by the observations of Jiang and Hackney (1997), who found that single heads may go through as many as 4 hydrolysis cycles, without stepping, before detaching from the microtubule. Thus the single head run time results are consistent with the literature as teams were found to remain attached to the microtubule for long times with faster teams having shorter run times, indicating detachment is accelerated by having more heads. This effect is presumably counteracted by the effect of increasing run time with more heads, hence 12 head teams have longer run times than 8 head teams.

5.5.5 Discussion

Why are 5 heads needed for sustained motion?

No movement was detected with fewer than 5 heads in the single-molecule assay. This result agrees with Hancock and Howard (1998), who predicted that 4-6 heads were required for sustained movement in a gliding assay. Other single-molecule studies have been conducted on single heads. Inoue et al. (2001) saw what they describe as processive movement with isolated single heads. Heads took many back-steps and the average run length was only 40nm. Using single heads on a bead in an optical trap, Kamei et al. (2005) found two single heads could displace the bead 50nm on average. These run

lengths would only be 5 or 6 steps for a kinesin dimer and are too short to be detected in the single-molecule assay used here. There may be some motion below 5 heads on a team but it is very difficult to detect using the system described here. For sustained motion, greater than 300nm (the threshold used by Hancock and Howard (1998)) the results shown here indicate that 5 heads are required.

Wild type kinesin requires only two heads for sustained motion so why is it that when the heads are split and rejoined, 5 are required? As all teams remain bound to the microtubule for a long time, it cannot be that lack of head coordination requires at least five heads, simply to hold the team on the microtubule. Rather, the results imply that part of the dimer motion is impaired. Single head team velocities never recover to dimer velocities (the fastest velocity observed with any team was $\sim$200nm/s) so the motion cannot be the same. Considering the dimer, there are two functions of the heads which could be impaired by separating them, forward bias and internal strain. Docking of the neck linker is thought to pull or bias the trailing head forwards (Rice et al. (1999)) enough to make an 8nm step. This may be impaired in teams of single heads and so 5 heads are required to recover forward motion. The internal strain which coordinates the motors (Kawaguchi (2008)) may also be lost from the dimer and 5 heads could be required to recover the

strain.

Internal strain can be communicated between heads through the microtubule or the link between heads. The wild type dimer is linked by the coiled coil but teams of single heads are linked by the DNA and the zinc finger proteins. There is also a flexible glycine hinge before the zinc finger. These protein linkers provide flexibility but the DNA is very rigid (with ∼4.5nm between binding sites) so it is unclear how much strain is communicated between heads in single head teams compared to the wild type dimer. There are two possible reasons single head teams could require strain mediated coordination: either heads must be coordinated to avoid all detaching at the same time and falling off the microtubule; or strain is required to detach heads. Teams remain attached for a long time, ruling out the former. The latter is possible but maybe less likely if only a subset of the available heads on a team are interacting with the microtubule. Figure 5.16 **a** shows the inter-head distances on the DNA-kinesin team and the distances between binding sites on the microtubule. It is clear that only ∼2 heads in a 5 head team can bind. Strain cannot be ruled out and is likely an important component of the motion but the forward bias must also be considered.

Hancock and Howard (1998) propose a model for single head gliding where each head can only make a small contribution to the motion, illustrated in

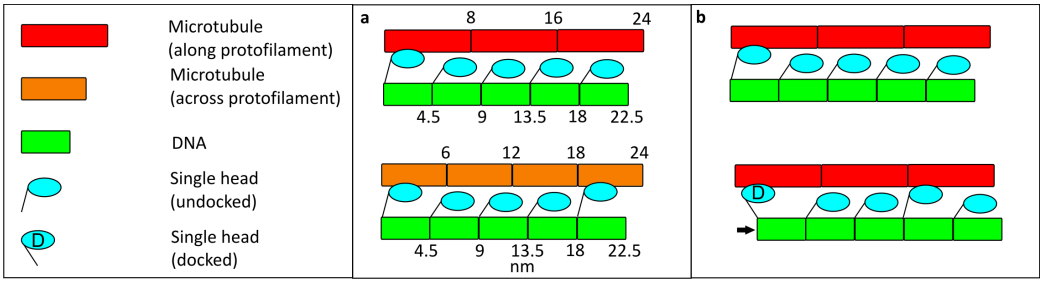

Figure 5.16: Schematic illustrating the number of heads which are able to interact in **a** and the walking cycle involving at least 5 heads in **b**.

Figure 5.16 **b**. This contribution moves (or kicks) the team or the microtubule on a small distance allowing another head (or heads) to bind. Enough heads are required such that there is always at least one head which can bind after each contribution. The number of heads required is thus equal to the microtubule binding site distance divided by the single head contribution size.

The wild type dimer takes 8nm steps, the distance between binding sites on a microtubule protofilament, but single heads have been shown to take steps onto adjacent microtubule protofilaments, a distance of ∼6nm (Song and Mandelkow (1993) - see Figure 5.17). Yajima and Cross (2005) identified a torsional component in single head gliding which led microtubules to rotate with a pitch of ∼500nm. This implies single heads took ∼10% side steps. The minimum binding site distance a single head team can move is then ∼6nm.

Hancock and Howard (1998) arrive at the size of the single head con-

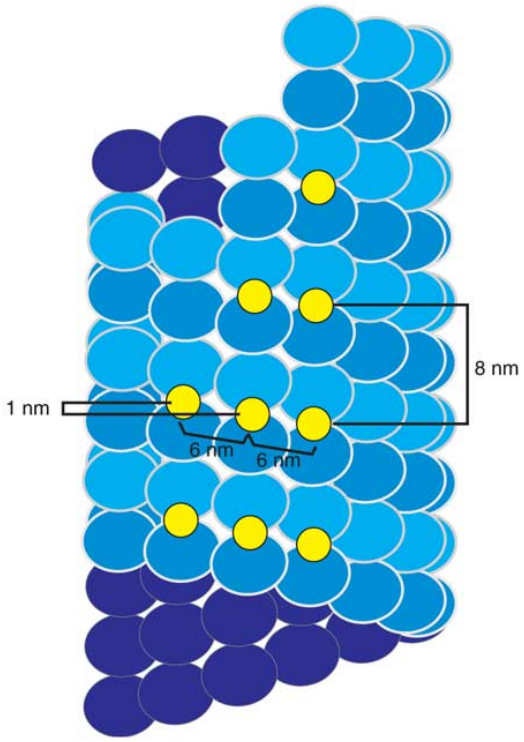

Figure 5.17: Schematic illustrating the binding sites on a microtubule from Yajima and Cross (2005). Tubulin monomers are in blue and purple and binding sites are in yellow.

tribution by considering the working distance of a single head. This is the distance moved during the part of the ATP hydrolysis cycle where the head is attached and is the multiple of the velocity and attachment time. Hancock and Howard (1998) suggest that if the attachment time is the same for single and double heads then the working distance of single head kinesin is ∼1nm. This value is very similar to the displacement the docking of the neck linker is thought to provide of 1-2nm (Rice et al. (1999); Block (2007); Kawaguchi (2008)). The requirement of 5 heads for sustained movement thus implies that the ability of heads in teams to amplify neck linker docking into an 8nm step requires a conformational change at the upper end of this range. An estimate of the single head contribution can be made from the 5 head requirement and the distance between binding sites. If 5 head teams can follow a protofilament, with 8nm between binding sites, then the single head contribution is ∼1.6nm but if they can only move onto adjacent protofilaments, with ∼6nm between binding sites, as is probable, then the single head contribution is ∼1.2nm.

What effect, if any, does the geometry play?

Mono-functionalised and bi-functionalised 6 head teams move with approximately the same velocity. However, considering that velocity is dependent on the geometry of single head stepping on the microtubule, it seems likely that

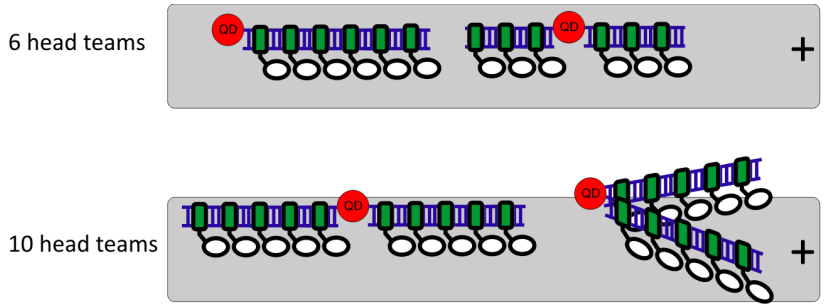

Figure 5.18: Schematic illustrating mono-functionalised and bi-functionalised 6 head teams (above) and two different orientations of a 10 head team (below).

the structure of the teams, including the difference between 1 and 2 template teams, is having an effect. The significant variation between teams might be explained by the geometry of binding (see Figure 5.18). Some configurations may be faster than others as they allow access to more favourable binding sites, those along the microtubule rather than around it. The shape of the velocity distribution may then represent the likelihood of teams binding in (or accessing) certain configurations. The long high velocity tails would then show that the fastest configurations are unlikely to occur - these may represent the motors perfectly aligned along the microtubule. It would be interesting to probe the effects of team geometry, possibly by using DNA origami to arrange single heads in different patterns and measuring the single-molecule velocity.

Why are 8 heads so much faster than 5 and 6?

The increase in velocity up to 8 heads in a team can be explained by considering the geometry of teams stepping on a microtubule. If the single head contribution is too small for 5 and 6 head teams to cycle through 8nm, that is to say the contribution from each head does not sum to 8nm, then sustained motion requires these teams move the 6nm between adjacent protofilaments around the microtubule. Teams with enough heads to cycle through 8nm (>7 heads) can move along the protofilament. This could account for the increase in velocity from 5-8 head teams. Splitting heads across two templates may also confer an advantage, although for 6 heads there was no observed difference between 1 and 2 template teams.

Figure 5.17 illustrates that moving 6nm around the microtubule only advances 1nm along the microtubule. Kymographic analysis means that only motion along the microtubule is measured and so if a team only moved around the microtubule, very low velocities would be measured. It takes 5 single head kicks around the microtubule to produce 1nm forward motion whereas 8 single head kicks produce 8nm, with each 1nm kick producing 1nm forward motion. This would imply that 8 head teams would travel with a velocity 5 times greater than 5 or 6 head teams. This is similar to the factor of $\sim$7 observed between 5 and 8 head teams in the data shown in Figure 5.13.

This description of stepping by teams of single heads is overly simplistic. In reality, teams step randomly, 8 head teams will make some movements around the microtubule and heads on 5 and 6 head teams will also step along the protofilament. Teams cannot step all the way around the microtubule as it is attached to the surface. Teams will also take back-steps. Wild type dimers take 5-10% back-steps (Schnitzer et al. (2000); Vale et al. (1996)) and Inoue et al. (2001) observed single heads to take almost as many back-steps as forward steps. Back-steps from single head teams would only be 1 single head contribution, ∼1nm and so individual back-steps would be unobservable in these experiments but it may be that teams with different number of heads and geometries take different numbers of back-steps.

Differences in the stepping or detachment rate of single head teams could also effect the velocity. If the stepping or detachment rate was the same for heads in all teams, then the run time would be proportional to the number of heads in a team as more heads would decrease the likelihood of a team falling off the microtubule (as found in dimers by Derr et al. (2012); Furuta et al. (2012)). The fact that slower teams with less heads remain bound to the microtubule for longer than faster teams with more heads (5 and 6 head teams vs. 8 head teams) implies that the detachment rate is not the same. This may be partially explained by the possible back-steps in teams

but could also be explained by internal strain accelerating stepping. This may also play a role in the velocity relationship with number of heads in a team.

Internal strain is thought to coordinate the heads in the wild type dimer (Kawaguchi2008) through two possible, non mutually exclusive, gating mechanisms. In the rear head gating model, release of the trailing head is accelerated by strain. The observations of Crevel et al. (2004); Schief et al. (2004) support this as they show that strain on the dimer accelerated the detachment of the rear head. A front head gated model is also possible where ATP binding in the front head is suppressed by internal strain until the back head detaches. Front head gating cannot account for increased detachment rates as this kind of gating would surely decrease velocity with number of heads (see Section 5.5.5). Rear head gating would account for accelerated detachment rates as the strain from many single heads could accelerate their detachment, increasing the velocity. It may be that 8 heads is optimal as this provides the optimal amount of internal strain to accelerate stepping.

The restoration of internal strain is probably the reason that Miyazono et al. (2009) observed an increase in velocity with single heads bound together. They covalently attached single heads to DNA using exposed cysteine residues at the end of the neck linker. Gliding velocity doubled to

235nm/s for DNA-dimerised single heads compared to single heads alone. This rigid dimerisation probably allowed restoration of some of the natural internal strain between the heads and accelerated stepping.

It is very likely that a combination of increased internal strain and an increased capacity to move along (rather than between) protofilaments accounts for the increase in velocity observed for larger single head teams. As the geometry of single head teams binding to the microtubule appears to explain the 5 head requirement, it seems likely that this is also the predominant factor in the velocity increase but the role of internal strain cannot be ignored.

Why does the velocity decrease with more than 8 heads?

The velocity decreases steadily for 8-12 head teams but remains significantly faster than < 8 heads. Thus more heads interacting with the microtubule slows down the team. A similar velocity decrease was seen by Kamei et al. (2005) using single head coated beads in an optical trap, from 350nm/s to 230nm/s, interpreted as move from 2-3 motors interacting. With kinesin dimers in single-molecule studies, teams of up to 7 dimers moved at constant velocity in experiments conducted by Derr et al. (2012) but Furuta et al. (2012) observed a slight decrease with more linked dimers in similar

experiments. In gliding assays, dimer velocity was thought to be independent of motor number (Hancock and Howard (1998)) but has been shown to decrease with large numbers of interacting motors by Bieling et al. (2008). They attribute drag to uncoordinated stepping and find that loose mechanical coupling of motors prevents drag. Single head teams may be slowed down by drag but molecular crowding and stepping geometry may also be a factor.

It is possible that molecular crowding slows down teams of single headed motors. 8 head teams can step freely on the microtubule but in teams larger than this, heads may interfere by attempting to step on each other or get in the way of finding a new binding site. This is difficult to reconcile with the geometry of the teams. 8-12 head teams are split across two sections of DNA and it seems unlikely that they should bind close enough to seriously interfere. The 10 head team has only 1 extra binding site on each of its two DNA templates compared to the 8 head team and it also seems unlikely that this should dramatically increase molecular crowding.

As the geometry of stepping on the microtubule accounts for the increase in velocity with heads, it might also explain the decrease. For this to be the case more than 8 heads would have to encourage more side steps. It is difficult to envisage how this would occur, as more heads would appear to be an advantage as they increase the available binding sites for the team. It is

more likely that more motors starts to produce a drag force on the team.

To understand the drag mechanism, it is helpful to consider the majority state of the motors. For the dimer, the majority state consists of a neck linker docked rear head and a strongly bound, nucleotide free, front head (Mori et al. (2007)). This is a strained state in the dimer and it is thought that this gates the motors, either by preventing the front head from binding nucleotide (front head gating) or accelerating detachment of the rear head (rear head gating). It is likely that this is also the majority state of single head teams with half the interacting heads having docked ('rear' heads) and the other half having bound strongly ('front' heads) [1]. The difference between single head teams and dimers is that the front heads in single head teams do not bind in a strained conformation. There is no mechanism (other than Brownian fluctuations) to strain them forwards, as there is in the dimer. Single heads maybe coordinated by strain when multiple motors in a team are able to interact with the microtubule at one time. With more motors interacting, it may be that front heads have to wait for some rear heads to detach before they can bind ATP and dock their neck linkers, as they cannot strain against the rear heads. This is front head gating. If detachment of rear heads is random and uncoordinated (and they do not otherwise contribute to

[1] N.B. 'front' and 'rear' refers to head conformation, not to position relative to the microtubule

motion), then it will take an increasingly long time with increasing numbers of heads before enough detach and allow the front heads to dock. This would cause velocity to decrease with increasing numbers of heads. If front heads can dock their neck linkers despite the strain produced by the rear heads, this would allow more front heads to bind but also create strain on the rear heads. Even if the new front heads can still bind their neck linkers against this strain, there must come a point where the rear strain is too much for front heads to dock neck linkers and they must wait for rear heads to detach. This produces a decrease in velocity with increasing numbers of heads.

It is also possible that strain may accelerate detachment of the rear heads - rear head gating. There is evidence from the run time data that faster teams have accelerated rear head detachment (discussed above) and other studies have shown strain accelerates detachment of the rear head (Crevel et al. (2004); Schief et al. (2004)). If this were the only gating mechanism, front heads would always be able to bind their neck linkers, producing forward movement and strain, accelerating detachment of rear heads. This would mean front heads would be able to dock their neck linkers despite any number of rear heads attached, which cannot be the case - as discussed above, there must be a point where rear head strain is too much for front heads to dock their neck linkers. Rear head gating may alleviate the drag caused

by front heads as the strain preventing front heads from docking their neck linkers also accelerates detachment of the rear heads. Single head teams may move with a combination of front head gating slowing them down but alleviated by accelerated rear head detachment. This could mean the velocity will plateau at a minimum value where front head gating and rear head detachment balance.

Further analysis and experiment

Further analysis of the data might yield more information about the mechanics of single head teams. The use of kymographs to obtain trajectories averages the motion of single teams. There is some noise in the kymograph and the Gaussian tracking showed some pausing events. Analysis of this motion might elucidate the number of motors involved in movement. More motors attached might reduce noise. Pausing events might be less likely with more motors as more motors allows the team to access more binding sites on the microtubule. Such analysis could be carried out on the kymograph trajectories by measuring the variance from a straight trajectory but might require Gaussian tracking. Control experiments on double head teams would show whether noise in single head teams was from their motion or noise in the experimental set up. Careful measurement of the experimental noise and the achievable positional accuracy would be required by tracking immobilised

QDs. This level of analysis was not undertaken because of time constraints but also to keep the analysis similar to recently published studies (Derr et al. (2012); Furuta et al. (2012)).

A number of experimental approaches from other kinesin studies could be applied to single head teams. Hackney (1994) measured the kinesin ADP release rate in the presence of microtubules. This showed an important step in the kinesin chemomechanical cycle but also the number of heads binding to the microtubule (1 or 2 in this case). This technique could be used with single head teams to show how many heads in a team initially bind to the microtubule. Coy (1999) correlated the kinesin speed with the ATPase rate to ascertain that one nucleotide is hydrolysed per step. Similar ATPase rate studies of single head teams would determine how ATP hydrolysed correlated with distance travelled. This would reveal information about the number of heads interacting and the step size. Yajima and Cross (2005) performed gliding assays with end-bent microtubules to measure their rotation. This could be repeated using a low density of single head teams. This might reveal if the number of heads in a team determined whether the team stepped more along or around the microtubule.

A geometric model of single head teams walking on microtubules might help confirm the walking model for these teams. A states based model where

teams step along or around the microtubule depending on the distance between the stepping head and the binding site and nucleotide state could be used. Full confirmation of the walking model could be had by measuring the step size, which may be ∼1nm for single head teams. This measurement is difficult but possible using advanced microscopes such as iSCAT (Ortega-Arroyo and Kukura (2012)) which uses interferometry of scattered light to image with high spatial and temporal resolution. Measurements of microtubules gliding on single heads and gold nanoparticle labelled single head teams are now being carried out by Dr Philip Kukura and his group to measure the step size of teams.

Conclusion

A number of explanations for the observed behaviour of single head teams have been explored but the most likely model is as follows. Single heads in teams are not capable of amplifying the small ∼1-2nm conformational change from neck linker docking into the 8nm steps observed in the dimer. Instead, single head teams advance along the microtubule by small kicks which place new heads in a position to bind the microtubule. This requires a minimum of 5 heads such that there is always a new head in a position to bind following a kick. This motion does not necessarily only proceed along the microtubule but may step around it, as binding sites on adjacent

protofilaments are closer (∼6nm) than on the same protofilament (8nm). This leads to an increase in the velocity of teams with more heads, up to 8. More heads provides more chance of binding along a single protofilament, producing more forward motion and faster velocities. More heads may also accelerate detachment of heads through internal strain, increasing velocity. Velocity decreases with more than 8 heads as more and more heads interact with the microtubule. The drag mechanism may be due to the prevention of nucleotide free heads from binding ATP and docking their neck linkers until the other docked heads have detached. The variation between teams can be explained by their binding geometry on the microtubule with some configurations allowing much better access to forward binding sites.

Chapter 6

Summary and future prospects

The work presented in this thesis uses the structures, dynamic interactions and the information carrying properties of DNA, combined with kinesin for nanotechnology and to create novel motor complexes to better understand kinesin itself. DNA has been used with kinesin (Schmidt and Vogel (2010); Derr et al. (2012); Furuta et al. (2012)) but mostly as a simple linker. Many systems have harnessed kinesin for nanotechnology but mainly using the inverted geometry where microtubule shuttles carry cargo on a carpet of kinesin (Schmidt and Vogel (2010); Dennis et al. (1999); Fischer et al. (2009)). The natural geometry has been under used because it requires organised track architectures (Goel and Vogel (2008)). Track systems have been created (Doot

et al. (2007)) but required top down construction rather than utilising the range of self-organised microtubule structures *in vivo* (Rogers et al. (2002); Tuma et al. (1998)) and *in vitro* (Nédélec et al. (1997); Hess et al. (2005)). This thesis presents a molecular transport system using a self-organised track network controlled by DNA encoded signals. It also presents a novel study of the minimal functional motor unit of kinesin using DNA to link teams of single kinesin heads and investigate their dynamics.

In Chapter 2 a DNA-kinesin hybrid was demonstrated. This hybrid was used in a novel construct similar in geometry to Eg5 kinesin (Subramanian and Kapoor (2012)) but which is capable of self-organising microtubules into radial asters. Methods were developed to use asters as a platform for transport and in Chapter 3 a shuttle was demonstrated using the DNA-kinesin hybrid which could travel on asters. These shuttles were used for molecular transport of cargo but also to transport DNA encoded signals which control the distribution of cargo on the microtubule architectures. In Chapter 4, shuttle transported signals were made to interact with the self-organisation process itself, adding a DNA-encoded disassembly signal which can destroy asters. Shuttles were studied at the single molecule level in Chapter 5 and then re-purposed to study the motor itself. DNA architectures can be used to link many motors together in defined geometries (Derr et al. (2012); Diehl

et al. (2006); Furuta et al. (2012)). Shuttles were designed to link teams of single kinesin heads together, study their behaviour and understand the minimal functional motor unit of kinesin.

A DNA-kinesin hybrid was developed and discussed in Chapter 2. A zinc finger kinesin fusion protein was created which could bind to a specific sequence of DNA. This allowed a DNA nanostructure to be used to arrange hybrids such that they could cross-link microtubules. This kinesin-DNA assembler could self-organise asters from cross-linked microtubules by sliding and sorting microtubules by polarity. To add new solutions whilst imaging asters, methods for tethering them to the surface were investigated. Biotinilated DNA on the assembler and a streptavidin coated surface in a flow chamber were used to tether asters. A flow chamber was designed which used passive pumping, where the difference in pressure between a larger and smaller droplet at connected inlets was used to make micro-litre fluid additions. Tethered asters were found to survive fluid flow, which allowed them to be used as a platform for transport as cargo carrying shuttles could be added and observed during imaging. Asters in these chambers were characterised by measuring their density in the flow chamber and their size distribution. They were found in the chamber with a frequency of $10^{-4}/\mu$m with an average radius of gyration of $\sim 4\mu$m. No asters were observed if assemblers were

used with only one kinesin or if there was no half twist of DNA between the kinesins. It was not possible to image aster formation from free microtubules but intermediate dynamics were observed.

The aster structure, similar to the radial microtubule array utilised in nature, was used as a track network for the transport of cargo by DNA-kinesin shuttles in Chapter 3. In the presence of ATP, these shuttles actively concentrate their cargo to the centre of asters. This effect was harnessed to create a cyclic transport system where cargo was scavenged from solution, actively concentrated and then released back into solution by an actively transported DNA signal. The signal operated using toe-hold mediated strand exchange between the signal and cargo shuttle. The transport system was found to operate as designed and two cycles of its operation were demonstrated.

The release signal could be actively transported by kinesin shuttles or passively transported, relying on diffusion to reach the cargo shuttles at the centre of the aster. These methods of transport were compared and active transport was found to be significantly more effective in the crowded environment at the centre of an aster. Averaging the skewness of the intensity weighted pixel intensity distribution of the cargo following addition of the release signal, only active transport produced a decrease in skewness corresponding to cargo release. The results are consistent with slowed diffusion

due to molecular crowding from assemblers and microtubules at the centre of the aster. As in eukaryotic cells, molecular motors are required for molecular transport but in cells this is to over come longer distances and less mobile cargoes.

The system was adapted to allow DNA encoded signals to disrupt asters. A modified assembler was designed which could split in response to a DNA encoded signal. Splitting the construct separates the two assembler kinesins, interrupting microtubule cross-linking and destroying asters. The two halves of this assembler were linked by a single strand containing a toe-hold such that toe-hold mediated strand displacement splits the assembler. Asters formed using this assembler were immobilised in flow chambers and their response to the disassembly signal tested. Disassembly could be measured by plotting the aster radius of gyration over time. This was observed to increase as the aster disassembled but, in many cases, with a lot of noise due to sections of the destroyed aster drifting in and out of focus. Thus disassembly was determined by eye. When the signal was actively transported, asters were found to readily disassemble but with diffusive delivery, disassembly occurred in only a minority of asters. Active transport was again required for effective delivery of the signal.

In these experiments, molecular complexes that are a few nanometres in

dimension transport cargo and control information flow over tens of micrometres. The active concentration of components, demonstrated by shuttles on asters, could be used to create colour changes (Bouchard et al. (2006); Tuma et al. (1998)) and to speed up reactions at low concentration or with high activation barriers (Simmel (2012)). The extension of the aster-based transport system to allow DNA encoded signals to interrupt the track network itself, rather than just cargo transported on it, represents a significant advance to the functionality of the system. In theory, it allows for complete recycling. Not only can the cargo be cycled through concentration and release but following this, the track network itself could be dismantled, back into its constituent microtubules. Such functionality could allow for an adaptive system, re-organising itself into different devices in response to signals.

The transport system could be improved in a number of ways. The number of sequential additions is limited by the violence of the fluid flow. A more complicated microfluidic system could be used with a much lower velocity flow. Such a system would also allow for many more different solutions to be added. The robustness of asters could also be improved by using a dilute solution of gluteraldehyde to fix the assembler kinesin to the microtubules (Doot et al. (2007)). If a low enough concentration of gluteraldehyde is used, transport by kinesin shuttles on top of fixed asters would not be inhibited,

although disassembly of these asters would not be possible. A micro-array of chambers just large enough to contain as aster could be used to create an array of asters. Such an array could be used to detect the bulk surface effects of the movement of cargo and detect colour changes. More control of cargo positioning could be engineered by labelling the microtubule minus ends with DNA adapters which could be made to bind cargo or shuttles which in turn could be released with DNA signals. Molecular transport technology is at an early stage but may one day be utilised in a diverse range of systems, already it might be used in lab on a chip devices for biosensing and medical testing. Molecular motors could shuttle analytes to different modules on the chip or perhaps even self-organise the modules themselves.

In Chapter 5 DNA-kinesin transport was investigated at the single molecule level. This was compared to the bulk transport on asters in previous chapters but was also used to investigate the mechanics of the motor itself. A single molecule assay was developed to observe DNA-kinesin moving on microtubules. Quantum dot labelling was chosen for its brightness and resistance to photo-bleaching. Various methods for tracking moving particles were investigated and kymography chosen as the optimum method for these studies. The assay was used to investigate assemblers and shuttles at the single molecule level to compare with the bulk transport in Chapter 3.

The single molecule assay was re-purposed to investigate the motor itself. The minimal motor unit of kinesin is a single head, which has been observed to move microtubules in gliding assays at ∼1/8th of the dimer velocity (Hancock and Howard (1998)) but cannot move processively in single molecule assays (Hancock and Howard (1998, 1999); Bieling et al. (2008); Kamei et al. (2005); Vale et al. (1996)). Hancock and Howard (1998) suggested that 4-6 motors are required for sustained movement. Some studies have observed increases in speed when multiple single heads are linked together (Kamei et al. (2005); Diehl et al. (2006)). The DNA-kinesin hybrids, used here, allow defined numbers of single heads to be linked together into a team.

DNA duplexes containing varying numbers of zinc finger binding sites were used to create teams of single heads. Teams of 4-12 heads were observed moving on microtubules. It was found that 5 heads were required for sustained movement, within the predicted number from Hancock and Howard (1998). 5 and 6 head teams moved very slowly at ∼1/8th of the single head gliding velocity ($0.10\pm0.01\mu$m/s) but the velocity was restored to the gliding value with 8 heads. Above this 10 and 12 head teams slowed down but remained significantly higher than <8 heads.

A number of explanations for the observed behaviour of single head teams

are explored but the most likely model is as follows. Single heads in teams are not capable of amplifying the small ∼1-2nm conformational change (Rice et al. (2003)) from neck linker docking into the 8nm steps observed in the dimer. Instead, single head teams advance along the microtubule by small kicks which place new heads in a position to bind the microtubule (Hancock and Howard (1998)). This requires a minimum of 5 heads such that there is always a new head in a position to bind following a kick. This motion does not necessarily only proceed along the microtubule but may step around it, as binding sites on adjacent protofilaments are closer (∼6nm) than on the same protofilament (8nm). This leads to an increase in the velocity of teams with more heads, up to 8. More heads provides more chance of binding along a single protofilament, producing more forward motion and faster velocities. More heads may also accelerate detachment of heads through internal strain, increasing velocity. Velocity decreases with more than 8 heads as more and more heads interact with the microtubule. The drag mechanism may be due to the prevention of nucleotide free heads from binding ATP and docking their neck linkers until the other docked heads have detached, analogous to the front head gating model (Kawaguchi (2008)).

Appendix A

Materials and methods

A.1 Alternative Kinesin-DNA binding Strategies

Two different methods for binding kinesin to DNA were investigated. A Tris-NTA modification to DNA was bound to the his-tag on the protein and covalent attachment, binding thiol modified DNA to exposed cysteine residues, was investigated.

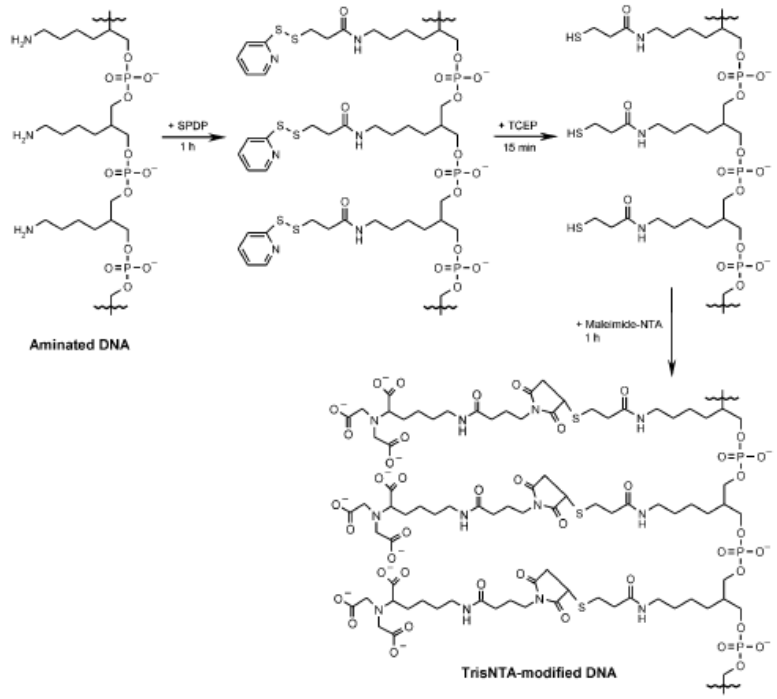

Figure A.1: Schematic of tris-NTA modification of triple aminated DNA from Goodman et al. (2009). Aminated oligos were reacted with a heterobifunctional crosslinker, N-succinimidyl 3-(2-pyridyldithio)propionate (SPDP). The disulphide bond was reduced, using (tris(2-carboxyethyl)phosphine (TCEP) and the remaining thiol group reacted with maleimide NTA.

A.1.1 Tris-NTA

Goodman et al. (2009) demonstrated linking his-tagged proteins to tris-NTA modified DNA. Recombinant proteins often carry a his-tag, six histidine residues, for metal affinity purification (see Chapter 2 Section 2.2.1). A Nickel mediated reaction with nitrilotriacetic acid (NTA) can bind the his tag. Lata et al. (2005) have shown that three NTA residues binds particularly well with a his tag. Tris NTA DNA is created from DNA modified with three amino groups, available commercially (IDT). Aminated oligos were reacted with a heterobifunctional crosslinker, N-succinimidyl 3-(2-

pyri- dyldithio)propionate (SPDP). The disulphide bind was reduced, using (tris(2-carboxyethyl)phosphine (TCEP) and the remaining thiol group reacted with maleimide NTA. The resulting product was purified using reverse phase liquid chromatography. When mixed with a his tagged protein and in the presence of nickel, the modified DNA should bind. The binding can be broken with addition of a suitable chelating agent.

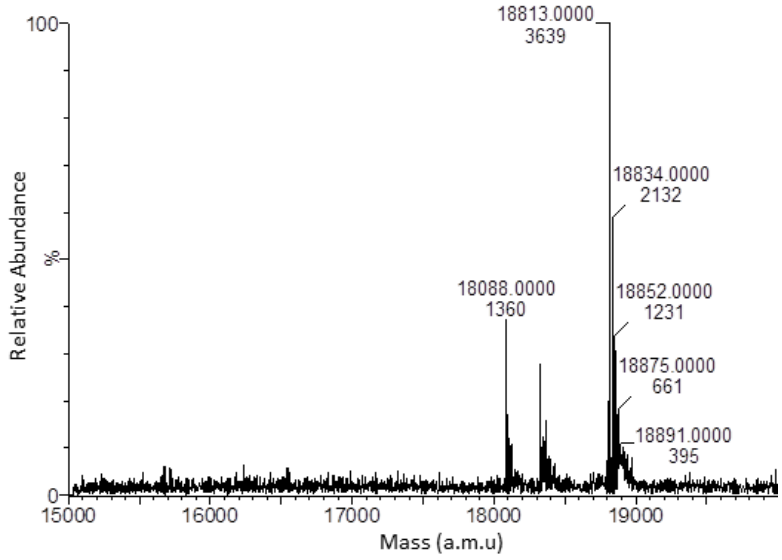

Figure A.2: Mass Spectrum of tris-NTA modified DNA. Expected mass of tris-NTA modified DNA was 18813 a.m.u. and a peak is observed in the trace at this point.

25μl of 100 μM DNA modified with three amino groups on the 5' end was modified with Tris-NTA. Bio-rad Spin 6 columns were equilibrated in phosphate buffer and the DNA spun into phosphate buffer. 12.5μl of 28mg/ml SPDP (Sigma) was added and incubated for 1 hour. Excess SPDP was removed with a spin and 7μl of TCEP (Sigma) added and incubated for 15

minutes. Excess TCEP removed with a spin column and 7μl of 50mg/ml Maleimide-NTA (Dojindo, Kumamoto, Japan) added and incubated for 1 hour. The modified oligo was spun into phosphate buffer, purified with reverse phase chromatography and stored at 4°C.

Modification of DNA was undertaken with Dr Carlos Sanchez-Cano. Figure A.2 shows the mass spectrum of the Tris-NTA modified oligo with the expected mass of 18813 a.m.u.. Repeated modification of the oligo was inconsistent and never obtained in high yield, probably as the quantity of starting material was too low - due to the expense of the modified oligo. For these reasons this attachment strategy was never used.

A.1.2 Cysteine

Proteins, including kinesin, can also be bound using exposed cysteine residues (Takeda et al. (2004)). Naturally occuring surface cysteine residues on a protein can be mutated to lysines. A single cysteine can then be placed where the DNA is desired. DNA modified with an amino group can then be cross-linked to the exposed cysteine using Sulfosuccinimidyl-4-(N-maleimidomethyl) cyclohexane-1-carboxylate (Sulfo-SMCC) which contains a maleimide group which reacts with cysteine and an NHS ester which reacts with the amine. Unlike the Tris-NTA binding, using this method the DNA is covalently bound to the

protein. The problem with labelling a dimer like kinesin is that it is difficult to avoid dual labelling the protein with DNA. The DNA-kinesin complexes obtained must be purified, by ion exchange or similar, to select only singularly labelled complexes. This was undertaken in collaboration with Dr Carlos Sanchez-Cano but was unfortunately unsuccessful.

A.2 Protein expression and purification

A.2.1 Vector Design

The kinesin zinc finger mutants were created by fusing the first 430 or 345 amino acids of rat kinesin-1 (K430 or K345) with a synthetic zinc finger (A1). K430 contains the head, neck linker and enough coiled coil for the protein to dimerize. K345 contains the head, neck linker and only a short section of coil so this protein is a monomer. The plasmid for the zinc finger protein was kindly supplied by Monika Papworth from the Laboratory of Molecular Biology, Cambridge. This plasmid was amplified from cDNA and further mutated by Dr Junichiro Yajima at the Marie Curie Cancer Research Centre, introducing a BamHI site and a (GGC)5 at the 5 end of the amplified DNA and a Sma I site, a His tag(CAT CAT CAT CAT CAT CAC) , a stop codon and an EcoR1 site at the 3 end of the amplified DNA. K345 and K430

were constructed from pKN172(RK430Gel) (Yajima et al. (2002)). After sequencing, both fragments were cloned into the pKN172 vector.

A.2.2 Transfection and expression

0.7μl Plasmid DNA mixed with 100μl of BL21 DE3 competent *e. coli* cells and placed on ice for 30 minutes, heat shocked for 2 minutes at 42°C and placed on ice again for a further 2 minutes. The cells were then plated on LB agar with 100μg/ml Carbenicillin and 10μg/ml D-Glucose and left at 37°C overnight.

Three colonies picked and grown in 5ml LB with 100μg/ml Carbenicillin at 37°C, shaking until OD>0.7. One of these cultures was then added to 400mL of LB with 100μg/ml Carbenicillin and 10μg/ml D-Glucose and grown overnight at 37°C, shaking at 300rpm. Eight 2l flasks with 500ml of 2x TY medium were also placed in the same incubator.

Each flask inoculated with 100μg/ml Carbenicillin and the 400mL culture split between the flasks. Flasks left shaking at 37°C until the OD $>$ 0.4, then placed on ice for 5 minutes. 5ml 100mM Zn SO4 added to a final concentration of 1mM and left on ice for 5 minutes. IPTG added to 0.41mM concentration and left at 20°C until the OD $\sim$1.

A.2.3 Purification

Cells were spun in a Sorvall ultracentrifuge with a 4l, SLC-4000 rotor for 10 minutes at 9000rpm, collected with PBS into a falcon tube and spin at 4000rpm for 15 minutes. Purification buffers were made. Buffer S1 contained 50mM Phosphate pH7.4, 100M ATP, 1mM MgCl2, 100M ZnSO4, 3mM-Mercaptoethanol and 0.025% Tween20. S2 was S1 supplemented with 350mM NaCl and S3 was S2 supplemented with 650mM Imidazol.

The cell pellet was dissolved in buffer S1, 3ml of buffer/gram of cell pellet and supplemented with EDTA tablet (1/50ml) (Roche) , lysozyme 0.1 mg/ml and triton X-100 to 0.05%. Mixture incubated on ice for 30 minutes and then sonicated to further break down the cells. DNAase added to 40μg/ml and $MgCl_2$ to 10mM and left on ice for a further 15 minutes. The cell lysate was spun at 45,000rpm in a T-865 rotor in a Sorvall ultracentrifuge for 1 hour. Supernatant immediately applied to Co-Talon resin (Clontech), equilibrated in buffer S1, and the protein left to bind to the beads for 2 hours.

The beads were packed in a column in a fast protein liquid chromatography (FPLC) system (Akta). The column was washed with buffer S2 until the conductivity had stabalised at 2ml/min. The protein was eluted with an imidazol gradient of 0-650mM by running increasing amounts of buffer S3 at 1.5ml/min. The protein eluted at 250mM imidazole as determined by slight

increase in absorbance at 280nm. 0.5mL factions were collected and ran on a dentaturing gel. A pre-cast 4-12% Bis-Tris stacking gel was run in MOPS buffer for 40 minutes at 200V. Fractions were chosen from the gel, pooled and concentrated overnight in a Slide-A-Lyzer dialysis casette (Pierce) in storage buffer which contained 50mM Pipes pH=6.8, 1mM MgCl2, 200μM ZnSO4, 5mMβ-Mercaptoethanol, 0.025% Tween20, 100mM NaCl and 20%Glycerol. The protein was then aliquoted and flash frozen and stored in liquid nitrogen.

A.3 Buffers

Experiments were performed in motility buffer (MB), unless otherwise stated: 20nM PIPES, 10mM CH3COOK, 1mM MgCl2 in ultrapure water (MilliQ). This was supplemented with 100μM ZnSO4 whenever the zinc finger was present (MZ100). The imaging buffer was made fresh for each experiment. MZ100 was supplemented with: 1mg/mL BSA; an oxygen scavenging system (D-glucose 4.5mg/mL, catalase 40μg/mL, glucose oxidase 216μg/mL and 0.5% 2-mercaptoethanol); an ATP regeneration system (creatine phosphate 5mM, creatine kinase 0.3mg/mL) and taxol 20μM to stabilize microtubules. Supplemented with 4mM ATP as required.

Other buffers used: BRB80 which contained 80 mM PIPES and 1 mM EGTA, pH 6.9. TAE which contained 40mM Tris pH 8.0, 20mM acetic acid

and 1mM EDTA. QD Buffer which contained Tris pH 8.0, 1mM EDTA, 100mM NaCl and 20mM $MgCl_2$. Phosphate buffer which contained 100mM sodium phosphate, 100 mM NaCl, pH 7.3.

A.4 Microtubules

Microtubules were polymerized from 20μg porcine tubulin (Cytoskeleton) and 2μg Hylite-labelled or Rhodamine-labelled porcine tubulin (Cytoskeleton), suspended in 20μL GBRB80 (80 mM PIPES, 1 mM EGTA, 5% glycerol, pH 6.9) with 1mM NaGTP and 2.5nM MgCl2 and incubated for 30 mins at 37 C before adding taxol to 25μM. Microtubule solution final concentration is 10μM (tubulin concentration). Aliquots were used fresh each day.

A.5 DNA Templates

DNA oligonucleotides were ordered lyophilized and HPLC purified (IDT) and re-suspended to 100μM in ultrapure water. DNA templates were prepared by mixing the required strands in MB to 10μM and annealing from 95°C to room temperature over ∼30 mins. Formation was tested by native polyacrylamide gel electrophoresis (PAGE). DNA-kinesin hybrids were formed by incubating the kinesin-zinc finger protein with the required DNA substrate for 30 mins

in MZ100 at room temperature. These samples were found to remain active for 1-2 hours. An excess of protein (∼3x) was required for acceptable DNA binding without excessive aggregation.

A.6 Gel Electrophoresis

A.6.1 Acrylamide Gels

DNA templates were tested in 15% 29:1 native polyacrylamide gels and tested with protein in 7% 74:1 native polyacrylamide gels. These were formed by mixing the correct ratio of 40% acrylamide solution (Sigma) and 2% bis-acrylamide solution in 1x TAE buffer supplemented with 0.01% mass/w ammonium persulfate (APS) and 0.01% v/v Tetramethylethylenediamine (TEMED). The were run in 1xTAE in a Bio-Rad gel kit at 250V for 15% and 100V for 7%. Gels were stained with SYBR^{TM}Gold and imaged in a gel scanner.

A.6.2 Agarose Gels

QD-DNA conjugates were tested in agarose gels. 1% agarose was dissolved in 1xTAE and microwaved for 2 minutes. the gel was run in a Bio-rad kit in 1xTAE at 300V. These gels were imaged directly by monitoring emission

from the QDs in a gel scanner.

A.6.3 PAGE purification

DNA complexes were PAGE purified by running 100μl of 10μM DNA on 15% 29:1 native polyacrylamide gels. Gels were imaged using a transilluminator and UV shadowing. Desired bands were cut out of the gel and soaked in MB buffer overnight. The gel mix was filtered through an Ultrafree MC filter (Millipore) by spinning at 12,000g for 1 hour.

A.7 Flow Chambers

The simple flow chamber was constructed from 25x50mm glass coverslip (Matsunami) with two 12x30mm peices of parafilm placed along the coverslip to form a channel. The chamber was sealed with a 25x25mm coverslip (Matsunai) by heating to 50°C for 30 minutes. Passive Pumping chambers were constructed from a glass microscope slide with two 0.5mm holes positioned 15mm apart using an ultrasonic drill. A section of parafilm, 25x50mm, was placed on the slide and a channel cut between the holes. The chamber was covered with a glass cover slip (Matsunami) and heated to 50°C for 30mins to seal. The external surface of the slide was coated in Rain X® a hydrophobic coating designed for car windscreens for better droplet formation on the

chamber ports. Mixing chambers were constructed with a similar method, two inlet holes were drilled at one end of the slide 10mm apart and the outlet drilled at the other end, 15mm from the inlets. A Y shaped channel was cut in the parafilm connecting the holes. Fluid was passivley pumped in these chambers by placing small drops at the inlets and then a big drop at the outlet.

A.8 Fluorescence Microscopy

Single channel fluorescence microscopy was performed using an Olympus IX71 inverted microscope with a 100x or 60x oil immersion objective. The Rhodamine microtubule filter (Olympus) had an excitation/emission range of 525-560nm/560-800nm. The light source was an Olympus U-RFL-T mercury burner. Tubulin was labelled with Rhodamine (excitation 525-600nm / emission 600-650nm). For single molecule studies, Qdot® 655 Streptavidin Conjugate (Invitrogen) with emission at 630-680nm.

Dual colour fluorescence microscopy was performed on an Olympus IX81 inverted microscope with a 100x or 60x oil immersion objective. Cy3 and Cy5 filters (Chroma) were used with excitation/emission ranges 530-560nm/575-645nm and 595-650nm/665-740nm respectively. These filters were mounted in an automated filter cassette (Prior) which allowed switching in 3.5-4s, set-

ting the frame rate for dual colour imaging. An Andor iXon 897 camera was used with the Andor iQ software for data acquisition. The light source was a Prior Lumen 200. Tubulin was labelled with Hylite 647® (excitation 600-630nm / emission 660-680nm) and the cargo was a Cy3 fluorophore (supplied conjugated to DNA strand F by IDT) (excitation 540-575nm / emission 550-590nm).

When neccessary, during gliding assays or QD assays, the temperature was controlled using the air conditioning of the room, a peltier temperature controlled stage (Linkam Scientific Instruments, Guildford UK) and an objective lens temperature controller (Bioptechs, USA).

A.9 Gliding Assay

Kinesin zinc finger fusion protein was characterized using a gliding assay by attaching to 1μM biotinylated, double-stranded DNA containing the zinc-finger binding site (name of strands in B). Motor solution was made with 1μM DNA, 3μM Kinesin and 2.5mg/ml BSA in MZ100. Microtubule solution was made with 0.5 μl microtubules, with 20μM Taxol and 2mg/ml BSA in 200μl MB. A simple flow chamber (7μl volume) was prepared by pipetting in: 2 volumes 4mg/ml streptavidin (3 minutes incubation each), 2 volumes 6mg/ml BSA (1 minute incubation each), 3 volumes motor solution (4 minute

incubation each), 1 volume 6mg/ml BSA (1 minute incubation, 1 volume microtubule solution (5 minute incubation) and finally, 1 vol imaging solution. Chambers were imaged immediately and microtubules were observed gliding over the surface. They were tracked using the Retrac program to deifne the microtubule end in each frame and measure the velocity between frames. Experiments were temperature controlled by water baths connected to cooling collars on the objective and stage. All measurements taken at 23.5°C.

A.10 Assemblers and shuttles

Assembler solution: 3.5μL MZ100, 0.75μl DNA (10μM), 5.25μL kinesin (10μM). Shuttle solution: 0.5μL DNA (10μM), 2μL kinesin (10μM), 2.5μL MZ100. Asters were formed in solutions of 3.5μL imaging buffer, 3μL assembler solution and 0.5μL microtubule solution (10μM tubulin concentration) and incubated for 10mins before insertion into the chamber. Shuttle solutions were diluted 50% in imaging buffer before chamber insertion.

A.11 Aster surface attachment

Chamber volume is approximately 7μL. Chamber surface was prepared by flowing in 2 volumes of 4 mg/ml streptavidin (Sigma Aldrich) in MB with 3

mins incubation per volume. Two volumes of 6mg/ml bovine serum albumin (Sigma Aldrich) in MB were then added with 1 min. incubation time to block any parts of the surface uncovered by streptavidin.

A.12 QD Monofunctionalisation

QD-DNA conjugates were mono-functionalised by mixing 3μl QD (1μM), 3μl DNA (1μM) and 2mg/ml BSA in 20μl total volume QD buffer. A centrifuge column was packed with 700μl of DEAE Sepharose beads (GE Healthcare) equillibrated in QD buffer by passing 3 volumes (700μl) through by hand. The QD-DNA conjugate sample was then applied to the column and non-conjugated beads were washed out with three volumes of QD buffer. The column was washed with increasing concentrations of NaCl from 200mM to 380mM in the QD buffer and a fraction collected for each wash. These fractions were ran on an agarose gel. Chosen fractions were buffer exchanged and concentrated in an Amicon Ultra 10kDa centrifugal filter. The fraction was spun through the column at 15,000g for 15 minutes. 500μl of MB were added and spun again. The concentrated sample was then collected by inverting the column and spinning at 15,000g for 5 minutes.

A.13 QD Assay

DNA-kinesin complexes were characterised using a single molecule assay by tagging the complexes with a quantum dot (QD) and imaging individual chromophores traversing along microtubules. QD shuttles were prepared using a biotinated duplex containing 1 zinc finger binding site (full sequence in Supplementary Table 1) and streptavidin coated QDs (Invitrogen), emission at 655nm. QD shuttle solution contained 100nM QDs, 100nM DNA, 300nM kinesin and 0.5mg/ml BSA in MZ100. Chambers were prepared by coating with 0.1mg/ml polyclonal tubulin antibody (Cytoskeleton) to immobilise microtubules, washing with 6mg/ml BSA solution to remove excess antibody, adding 100 fold dilution of rhodamine labelled microtubules (prepared as above), a further wash to remove excess microtubules and finally the QD shuttle solution diluted 300x in imaging buffer. Chambers were observed using the Cy3 filter. Both QDs and microtubules are visible in this filter with the QDs showing as bright spots on less bright microtubules. Experiments were temperature controlled by water baths connected to cooling collars on the objective and stage. All measurements taken at 23.5°C.

A.14 HPLC

Reverse phase seperates strands of DNA based on their hydrophobicity under denaturing conditions and was used to purify the tris-NTA modified strand. An Agilent 1200$^{\text{TM}}$high performance liquid chromatography (HPLC) was used with a Waters XBridgeTM OST C18 2.5 μm 4.6 x 50 mm column. Flow rate was set at 1 mL/min with a linear gradient of buffer A, 0.1 M triethylammonium acetate (TEAA), 5% acetonitrile, pH 7.0 to buffer B, 0.1 M triethylammonium acetate, 70% acetonitrile, pH 7.0. Fractions were collected based on the absorbance at 260nm and tested by mass spectometry.

A.15 Mass Spectometry

Samples for mass spectometry were eluted from a Waters XBridge OST C18 2.5 4.6 x 50 mm column heated to 50°C with a linear buffer gradient from Buffer C (400 mM 1,1,1,3,3,3-hexafluoroisopropanol, 16.3 mM triethylamine, 5% methanol) to Buffer D (400 mM 1,1,1,3,3,3- hexafluoroisopropanol, 16.3 mM triethylamine, 60% methanol). These samples were injected straight into a Waters LCT Premier reflectron TOF mass spectrometer

Appendix B

DNA and Protein Sequences

B.1 DNA sequences

B.1.1 Aster

Tris NTA modified strands

Tris NTA A

5'-CCTTACGGACGCTGAAGTAATGCCGGAATCCTGCGATAGTCAT

ATCTAGAGC/iAmMC6T//iAmMC6T//3AmMC6T/-3'

Tris NTA B

5'-GCTCTAGATATGACTATCGCAGGATTCCGGCATTACTTCAGCG

TCCGTAAGG-3'

biotinylated strands

biotinylated duplex containing 1 zinc-finger binding site, used for gliding assays and in the streptavidin assembler.

K1(4)A

5'-biotinGGAAGGATCGGGCGTAGACTGACGATAGACTGACGATAG ACTGACGAGCTAG-3'

K1(4)B

5'-CTAGCTCGTCAGTCTATCGTCAGTCTATCGTCAGTCTACGCCC GATCCTTCC-3'

Assemblers

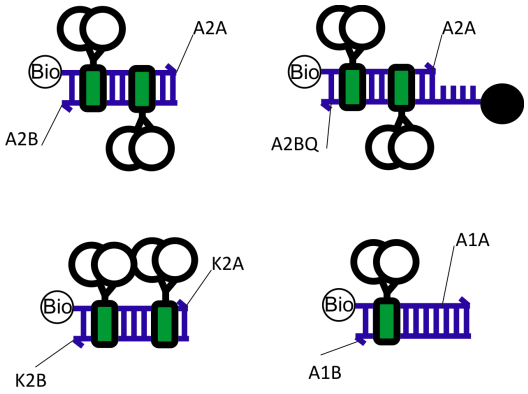

Figure B.1: Schematic of DNA designs. Strands labelled.

The regular assembler.

A2A

5'-GGAAGGATCGGGCGTCAAGCAGATCGGGCGGCTAG/Biotin-3'

A2B

5'-CTAGCCGCCCGATCTGCTTGACGCCCGATCCTTCC-3'

A2BQ

5'-CTAGCCGCCCGATCTGCTTGACGCCCGATCCTTCCGCACGGGG

TTCGTTGAGTCG/BHQ2-3'

A1. The regular assembler with a mutated zinc finger binding site. This strand was used as the QD carrying shuttle in Chapter 5.

A1A

5'-biotinGGAAGGACTGACGATAGATCGGGCGGCTAG3-'

A1B

5'-CTAGCCGCCCGATCTATCGTCAGTCCTTCC-3'

K2. The regular assembler without the half twist between the two binding sites.

K2A

5'-biotinGGAAGGATCGGGCGTAGATCGGGCGGCTAG-3'

K2B

5'-CTAGCCGCCCGATCTACGCCCGATCCTTCC-3'

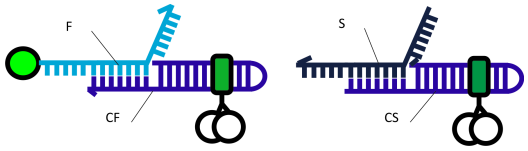

Figure B.2: Schematic of DNA designs. Strands labelled.

B.1.2 Cargo Transport

The fluorophore carrying shuttle, CF, and the fluorophore carrying cargo strand, F.

CF

5'-CGCCCCGCCCGATCGAGGCACACGAGCCTCGATCGGGCGGGG
CGGCACGGGGTT-3'

F

5'-Cy3/CGACTCAACGAACCCCGTGCTTAGTATTATCATTTACGCC
-3'

The release strand carrying shuttle, CS, and the release signal strand, S.

CS

5'-CATTTACGCCCGGACGATCGGGCGGCAGCACACGAGCTGCCG
CCCGATCGTCCG-3'

S

5'-GGCGTAAATGATAATACTAAGCACGGGGTTCGTTGAGTCG-3'

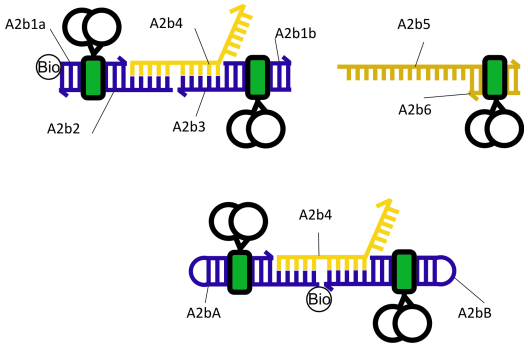

Figure B.3: Schematic of DNA designs. Strands labelled.

B.1.3 Disassembly

A2b1a

5'-Biotin/GGAGGATCGGGCGTACACCTCGGTGCAG-3'

A2b1b

5'-GGAGGATAGTGGTTAGATCGGGCGGCAG-3'

A2b2

5'-GCATTTGAGAATCCCCTGCACCGAGGTGTACGCCCGATCCTCC
-3'

A2b3

5'-CTGCCGCCCGATCTAACCACTATCCTCCCCCTAAGAGTTTACG-
3'

A2b4

5'-GGGATTCTCAAATGCCGTAAACTCTTAGGGCCCTAGGG-3'

A2bhpA

5'-GCATTTGAGAATCCCCTGCACCGAGGTGTACGCCCGATCCTCC

TGAAGTGGAGGATCGGGCGTACACCTCGGTGCAG-3'

A2bhpB

5'-GGAGGATAGTGGTTAGATCGGGCGGCAGTCCTTTCTGCCGCC

CGATCTAACCACTATCCTCCCCCTAAGAGTTTACG-3'

A2b5

5'-CTAGCCGCCCGATCCTTCCCCCTAGGGCCCTAAGAGTTTACGG

CATTTGAGAATCCC-3'

A2b6

5'GGAAGGATCGGGCGGCTAG3'

B.1.4 Single Molecule

DNA for teams of single heads used in Chapter 5 with 3-6 kinesin binding sites, K3-6.

K3A

5-biotin/GGAAGGATCGGGCGTAGATCGGGCGTAGATCGGGCGGC

TAG-3

K3B

5-CTAGCCGCCCGATCTACGCCCGATCTACGCCCGATCCTTCC-3

K4A

5-biotin/GGAAGGATCGGGCGTAGATCGGGCGTAGATCGGGCGTA

GATCGGGCGGCTAG-3

K4B

5-CTAGCCGCCCGATCTACGCCCGATCTACGCCCGATCTACGCCC

GATCCTTCC-3

K5A

5-biotin/GGAAGGATCGGGCGTAGATCGGGCGTAGATCGGGCGTA

GATCGGGCGTAGATCGGGCGGCTAG-3

K5B

5-CTAGCCGCCCGATCTACGCCCGATCTACGCCCGATCTACGCCC

GATCTACGCCCGATCCTTCC-3

K6A

5-biotin/GGAAGGATCGGGCGTAGATCGGGCGTAGATCGGGCGTA

GATCGGGCGTAGATCGGGCGTAGATCGGGCGGCTAG-3

K6B

5-CTAGCCGCCCGATCTACGCCCGATCTACGCCCGATCTACGCCC

GATCTACGCCCGATCTACGCCCGATCCTTCC-3

B.2 Kinesin Zinc finger constructs

Single-headed rat kinesin with zinc-finger protein (rK345-A): MGFADPAE
CSIKVMCRGRPLNEAEILRGDKFIPKFKGEETVVIGQGKPYVFDRVL
PPNTTQEQVYNACAKQIVKDVLEGYNGTIFAYGQTSSGKTHTMEGK
LHDPQLMGIIPRIAHDIFDHIYSMDENLEFHIKVSYFEIYLDKIRDLLDV
SKTNLAVHEDKNRVPYVKGCTERFVSSPEEVMDVIDEGKANRHVAV
TNMNEHSSRSHSIFLINIKQENVETEKKLSGKLYLVDLAGSEKVSKTG
AEGAVLDEAKNINKSLSALGNVISALAEGTKTHVPYRDSKMTRILQD
SLGGNCRTTIVICCSPSVFNEAETKSTLMFGQRAKTIKNTVSVNLELT
AEEWKKKGSGGGGGAEERPYACPVESCDRRFSRSDELTRHIRIHTG
QKPFQCRICMRNFSRSDHLSTHIRTHTGEKPFACDICGRKFATNSNRI
KHTKIHLRQKDAARDPHHHHHH

Double-headed rat kinesin with zinc-finger protein (rk430-A): MGFADPAE
CSIKVMCRGRPLNEAEILRGDKFIPKFKGEETVVIGQGKPYVFDRVL
PPNTTQEQVYNACAKQIVKDVLEGYNGTIFAYGQTSSGKTHTMEGK
LHDPQLMGIIPRIAHDIFDHIYSMDENLEFHIKVSYFEIYLDKIRDLLDV
SKTNLAVHEDKNRVPYVKGCTERFVSSPEEVMDVIDEGKANRHVAV
TNMNEHSSRSHSIFLINIKQENVETEKKLSGKLYLVDLAGSEKVSKTG
AEGAVLDEAKNINKSLSALGNVISALAEGTKTHVPYRDSKMTRILQD
SLGGNCRTTIVICCSPSVFNEAETKSTLMFGQRAKTIKNTVSVNLELT

AEEWKKKGSYEKEKEKNKALKSVIQHLEVELNRWRNGEAVPEDEQ

ISAKDHKSLEPCDNTPIIDNITPVVDGISAEKEKYDEEITSLYRQLDDK

GGGGGAEERPYACPVESCDRRFSRSDELTRHIRIHTGQKPFQCRICM

RNFSRSDHLSTHIRTHTGEKPFACDICGRKFATNSNRIKHTKIHLRQK

DAARDPHHHHHH

Bibliography

Alonso, M. C., Drummond, D. R., Kain, S., Hoeng, J., Amos, L., and Cross, R. a. (2007). An ATP gate controls tubulin binding by the tethered head of kinesin-1. *Science*, 316(5821):120–3.

Amaratunga, A., Leeman, S. E., Kosik, K. S., and Fine, R. E. (2002). Inhibition of Kinesin Synthesis In Vivo Inhibits the Rapid Transport of Representative Proteins for Three Transport Vesicle Classes into the Axon. *Journal of Neurochemistry*, 64(5):2374–2376.

Andersen, E. S., Dong, M., Nielsen, M. M., Jahn, K., Subramani, R., Mamdouh, W., Golas, M. M., Sander, B., Stark, H., Oliveira, C. L. P., Pedersen, J. S., Birkedal, V., Besenbacher, F., Gothelf, K. V., and Kjems, J. (2009). Self-assembly of a nanoscale DNA box with a controllable lid. *Nature*, 459(7243):73–6.

Arnal, I. and Wade, R. H. (1998). Nucleotide-dependent conformations of the kinesin dimer interacting with microtubules. *Structure*, 6(1):33–8.

Asbury, C. L. (2005). Kinesin: world's tiniest biped. *Current opinion in cell biology*, 17(1):89–97.

Bazylak, A., Heinrich, J., Djilali, N., and Sinton, D. (2008). Liquid water transport between graphite paper and a solid surface. *Journal of Power Sources*, 185(2):1147–1153.

Berthier, E. and Beebe, D. J. (2007). Flow rate analysis of a surface tension driven passive micropump. *Lab on a Chip*, 7(11):1475.

Bieling, P., Telley, I., Piehler, J., and Surrey, T. (2008). Processive kinesins require loose mechanical coupling for efficient collective motility. *EMBO reports*, 9(11):1121–7.

Block, S. M. (2007). Kinesin motor mechanics: binding, stepping, tracking, gating, and limping. *Biophysical journal*, 92(9):2986.

Block, S. M., Asbury, C. L., Shaevitz, J. W., and Lang, M. J. (2003). Probing the kinesin reaction cycle with a 2D optical force clamp. *Proceedings of the National Academy of Sciences of the United States of America*, 100(5):2351–6.

Bouchard, A., Warrender, C., and Osbourn, G. (2006). Harnessing microtubule dynamic instability for nanostructure assembly. *Physical Review E*, 74(4):1–16.

Braun, M., Drummond, D. R., Cross, R. A., and McAinsh, A. D. (2009). The kinesin-14 Klp2 organizes microtubules into parallel bundles by an ATP-dependent sorting mechanism. *Nature cell biology*, 11(6):724–730.

Carroll-Portillo, A., Bachand, M., Greene, A. C., and Bachand, G. D. (2009). In vitro Capture, Transport, and Detection of Protein Analytes Using Kinesin-Based Nanoharvesters. *Small*, 5(16):1835–1840.

Carson, J. and Collier, A. (1981). Morphometric aspects of ciliary distribution and ciliogenesis in human nasal epithelium. *Proceedings of the National Academy of Sciences*, 78(11):6996–6999.

Carstairs, H. (2008). *A DNA-Kinesin based molecular shuttle & studies of DNA Kagome arrays*. PhD thesis, Univeristy of Oxford.

Carstairs, H. M. J., Lymperopoulos, K., Kapanidis, A. N., Bath, J., and Turberfield, A. J. (2009). DNA monofunctionalization of quantum dots. *ChemBioChem*, 10(11):1781–3.

Case, R. B., Rice, S., Hart, C. L., Ly, B., and Vale, R. D. (2000). Role of the kinesin neck linker and catalytic core in microtubule-based motility. *Current biology : CB*, 10(3):157–60.

Coy, D. L. (1999). Kinesin Takes One 8-nm Step for Each ATP That It Hydrolyzes. *Journal of Biological Chemistry*, 274(6):3667–3671.

Crevel, I. M., Lockhart, A., and Cross, R. A. (1997). Kinetic evidence for low chemical processivity in ncd and Eg5. *Journal of molecular biology*, 273(1):160–70.

Crevel, I. M.-T. C., Nyitrai, M., Alonso, M. C., Weiss, S., Geeves, M. A., and Cross, R. A. (2004). What kinesin does at roadblocks: the coordination mechanism for molecular walking. *The EMBO journal*, 23(1):23–32.

Crocker, J. and Grier, D. (1996). Methods of digital video microscopy for colloidal studies. *Journal of colloid and interface science*, 310(179):298–310.

Cross, R. (2004a). Molecular Motors: Kinesin's Interesting Limp. *Current Biology*, 14(4):R158–R159.

Cross, R. a. (2004b). The kinetic mechanism of kinesin. *Trends in biochemical sciences*, 29(6):301–9.

Dennis, J. R., Howard, J., and Vogel, V. (1999). Molecular shuttles: directed motion of microtubules along nanoscale kinesin tracks. *Nanotechnology*, 10(3):232–236.

Derr, N. D., Goodman, B. S., Jungmann, R., Leschziner, a. E., Shih, W. M., and Reck-Peterson, S. L. (2012). Tug-of-War in Motor Protein Ensembles Revealed with a Programmable DNA Origami Scaffold. *Science*, 662.

Desai, A. and Mitchison, T. J. (1997). MICROTUBULE POLYMERIZATION. pages 83–117.

Diehl, M. R., Zhang, K., Lee, H. J., and Tirrell, D. A. (2006). Engineering cooperativity in biomotor-protein assemblies. *Science*, 311(5766):1468.

Doot, R. K., Hess, H., and Vogel, V. (2007). Engineered networks of oriented microtubule filaments for directed cargo transport. *Soft Matter*, 3(3):349–356.

Douglas, S. M., Dietz, H., Liedl, T., Högberg, B., Graf, F., and Shih, W. M. (2009). Self-assembly of DNA into nanoscale three-dimensional shapes. *Nature*, 459(7245):414–8.

Dreblow, K., Kalchishkova, N., and Böhm, K. J. (2010). Kinesin passing permanent blockages along its protofilament track. *Biochemical and biophysical research communications*, 395(4):490–5.

Drew, H. and Wing, R. (1981). Structure of a B-DNA dodecamer: conformation and dynamics. *Proceedings of the National Academy of Sciences*, 78(4):2179–2183.

Drummond, D. R., Kain, S., Newcombe, A., Hoey, C., Katsuki, M., and Cross, R. A. (2011). Purification of tubulin from the fission yeast Schizosaccharomyces pombe. *Methods in molecular biology*, 777:29–55.

Du, Y., Shim, J., Vidula, M., Hancock, M. J., Lo, E., Chung, B. G., T. Borenstein, J., Khabiry, M., M. Cropek, D., and Khademhosseini, A. (2009). Rapid generation of spatially and temporally controllable long-range concentration gradients in a microfluidic device. *Lab on a Chip*, 9(6):761.

Evett, J. and Isenberg, I. (1969). DNA-Polylysine interaction as studied by polarization of fluorescence. *Annals of the New York Academy of Sciences*, 158(1 Electronic As):210–222.

Fischer, T., Agarwal, A., and Hess, H. (2009). A smart dust biosensor powered by kinesin motors. *Nature nanotechnology*, 4(3):162–6.

Furuta, K., Furuta, a., Toyoshima, Y. Y., Amino, M., Oiwa, K., and Kojima, H. (2012). Measuring collective transport by defined numbers of processive and nonprocessive kinesin motors. *Proceedings of the National Academy of Sciences*, 110(2).

Gardner, M. K., Odde, D. J., and Bloom, K. (2008). Kinesin-8 molecular motors: putting the brakes on chromosome oscillations. *Trends in cell biology*, 18(7):307–10.

Gardner, M. K., Zanic, M., and Howard, J. (2013). Microtubule catastrophe and rescue. *Current opinion in cell biology*, 25(1):14–22.

Gennerich, A. and Vale, R. D. (2009). Walking the walk: how kinesin and

dynein coordinate their steps. *Current Opinion in Cell Biology*, 21(1):59–67.

Gibbons, I. R. (1966). Studies on the adenosine triphosphatase activity of 14 S and 30 S dynein from cilia of Tetrahymena. *The Journal of biological chemistry*, 241(23):5590–6.

Gilbert, S. P., Moyer, M. L., and Johnson, K. A. (1998). Alternating site mechanism of the kinesin ATPase. *Biochemistry*, 37(3):792–9.

Goel, A. and Vogel, V. (2008). Harnessing biological motors to engineer systems for nanoscale transport and assembly. *Nature Nanotechnology*, 3(8):465–475.

Goldstein, L. and Yang, Z. (2000). Microtubule-based transport systems in neurons: the roles of kinesins and dyneins. *Annual Review of Neuroscience*, 23:39–71.

Goodman, R. P., Erben, C. M., Malo, J., Ho, W. M., McKee, M. L., Kapanidis, A. N., and Turberfield, A. J. (2009). A Facile Method for Reversibly Linking a Recombinant Protein to DNA. *ChemBioChem*, 10(9):1551–1557.

Goodman, R. P., Schaap, I. A. T., Tardin, C. F., Erben, C. M., Berry, R. M., Schmidt, C. F., and Turberfield, A. J. (2005). Rapid Chiral Assembly

of Rigid DNA Building Blocks for Molecular Nanofabrication. *Science*, 310(5754):1661–1665.

Green, S., Bath, J., and Turberfield, A. (2008). Coordinated Chemomechanical Cycles: A Mechanism for Autonomous Molecular Motion. *Physical Review Letters*, 101(23):238101.

Gutierrez-Medina, B. and Block, S. M. (2010). Visualizing individual microtubules by bright field microscopy. *American Journal of Physics*, 78(11):1152.

Hackney, D. D. (1994). The rate-limiting step in microtubule-stimulated ATP hydrolysis by dimeric kinesin head domains occurs while bound to the microtubule. *The Journal of biological chemistry*, 269(23):16508–11.

Hahlen, K., Ebbing, B., Reinders, J., Mergler, J., Sickmann, A., and Woehlke, G. (2006). Feedback of the kinesin-1 neck-linker position on the catalytic site. *The Journal of biological chemistry*, 281(27):18868–77.

Hammond, J. W., Cai, D., and Verhey, K. J. (2008). Tubulin modifications and their cellular functions. *Current opinion in cell biology*, 20(1):71–6.

Hancock, W. O. and Howard, J. (1998). Processivity of the motor protein kinesin requires two heads. *The Journal of cell biology*, 140(6):1395–405.

Hancock, W. O. and Howard, J. (1999). Kinesin's processivity results from mechanical and chemical coordination between the ATP hydrolysis cycles of the two motor domains. *Proceedings of the National Academy of Sciences of the United States of America*, 96(23):13147–52.

Hartman, M. A. and Spudich, J. A. (2012). The myosin superfamily at a glance. *Journal of cell science*, 125(Pt 7):1627–32.

Heald, R., Tournebize, R., Blank, T., Sandaltzopoulos, R., Becker, P., Hyman, A., and Karsenti, E. (1996). Self-organization of microtubules into bipolar spindles around artificial chromosomes in Xenopus egg extracts. *Nature*, 382(6590):420–5.

Hess, H., Clemmens, J., Brunner, C., Doot, R., Luna, S., Ernst, K.-H., and Vogel, V. (2005). Molecular self-assembly of "nanowires"and "nanospools" using active transport. *Nano letters*, 5(4):629–33.

Hess, H., Howard, J., and Vogel, V. (2002). A Piconewton Forcemeter Assembled from Microtubules and Kinesins. *Nano Letters*, 2(10):1113–1115.

Hiratsuka, Y., Tada, T., Oiwa, K., Kanayama, T., and Uyeda, T. Q. (2001). Controlling the direction of kinesin-driven microtubule movements along microlithographic tracks. *Biophys. J.*, 81(3):1555–1561.

Hirokawa, N., Nitta, R., and Okada, Y. (2009). The mechanisms of kinesin

motor motility: lessons from the monomeric motor KIF1A. *Nature reviews. Molecular cell biology*, 10(12):877–84.

Hirose, K., Löwe, J., Alonso, M., Cross, R. A., and Amos, L. A. (1999). Congruent docking of dimeric kinesin and ncd into three-dimensional electron cryomicroscopy maps of microtubule-motor ADP complexes. *Molecular biology of the cell*, 10(6):2063–74.

Hiyama, S., Gojo, R., Shima, T., Takeuchi, S., and Sutoh, K. (2009). Biomolecular-Motor-Based Nano- or Microscale Particle Translocations on DNA Microarrays. *Nano Letters*, 9(6):2407–2413.

Hoenger, A., Sack, S., Thormählen, M., Marx, A., Müller, J., Gross, H., and Mandelkow, E. (1998). Image reconstructions of microtubules decorated with monomeric and dimeric kinesins: comparison with x-ray structure and implications for motility. *The Journal of cell biology*, 141(2):419–30.

Holy, T. E., Dogterom, M., Yurke, B., and Leibler, S. (1997). Assembly and positioning of microtubule asters in microfabricated chambers. *Proceedings of the National Academy of Sciences of the United States of America*, 94(12):6228–31.

Howard, J. (1996). The Movement of Kinesin Along Microtubules. *Annual Review of Physiology*, 58(1):703–729.

Howard, J., Hudspeth, A., and Vale, R. (1989). Movement of microtubules by single kinesin molecules. *Nature*, 342(6246):154–158.

Hsieh, S. S. and Huang, Y. C. (2008). Passive mixing in micro-channels with geometric variations. *Journal of Micromechanics and Microengineering*, 18:065017.

Hua, W., Chung, J., and Gelles, J. (2002). Distinguishing inchworm and hand-over-hand processive kinesin movement by neck rotation measurements. *Science*, 295(5556):844–8.

Hua, W., Young, E. C., Fleming, M. L., and Gelles, J. (1997). Coupling of kinesin steps to ATP hydrolysis. *Nature*, 388(6640):390–3.

Hunt, a. J. and Howard, J. (1993). Kinesin swivels to permit microtubule movement in any direction. *Proceedings of the National Academy of Sciences of the United States of America*, 90(24):11653–7.

Hyman, a., Drechsel, D., Kellogg, D., Salser, S., Sawin, K., Steffen, P., Wordeman, L., and Mitchison, T. (1991). Preparation of modified tubulins. *Methods in enzymology*, 196(1984):478–85.

Idan, O., Lam, A., Kamcev, J., Gonzales, J., Agarwal, A., and Hess, H. (2012). Nanoscale transport enables active self-assembly of millimeter-scale wires. *Nano letters*, 12(1):240–5.

Inoue, Y., Hikikoshi Iwane, A., Miyai, T., Muto, E., and Yanagida, T. (2001). Motility of Single One-Headed Kinesin Molecules Along Microtubules. *Biophysical Journal*, 81(5):2838–2850.

Jamison, D. K., Driver, J. W., Rogers, A. R., Constantinou, P. E., and Diehl, M. R. (2010). Two Kinesins Transport Cargo Primarily via the Action of One Motor: Implications for Intracellular Transport. *Biophysical journal*, 99(9):2967–77.

Jasper, J. J. (1972). The Surface Tension of Pure Liquid Compounds. *Journal of Physical and Chemical Reference Data*, 1(4):841.

Jeune-Smith, Y. and Hess, H. (2010). Engineering the length distribution of microtubules polymerized in vitro. *Soft Matter*, 6(8):1778.

Jiang, W. and Hackney, D. D. (1997). Monomeric Kinesin Head Domains Hydrolyze Multiple ATP Molecules before Release from a Microtubule. *Journal of Biological Chemistry*, 272(9):5616–5621.

Kamei, T., Kakuta, S., and Higuchi, H. (2005). Biased binding of single molecules and continuous movement of multiple molecules of truncated single-headed kinesin. *Biophysical journal*, 88(3):2068–77.

Kaseda, K., Higuchi, H., and Hirose, K. (2003). Alternate fast and slow step-

ping of a heterodimeric kinesin molecule. *Nature cell biology*, 5(12):1079–82.

Kawaguchi, K. (2008). Energetics of kinesin-1 stepping mechanism. *FEBS letters*, 582(27):3719–3722.

Ke, Y., Ong, L. L., Shih, W. M., and Yin, P. (2012). Three-dimensional structures self-assembled from DNA bricks. *Science*, 338(6111):1177–83.

Keith, C. H., Feramisco, J. R., and Shelanski, M. (1981). Direct visualization of fluorescein-labeled microtubules in vitro and in microinjected fibroblasts. *The Journal of cell biology*, 88(1):234–40.

Kikkawa, M. (2008). The role of microtubules in processive kinesin movement. *Trends in cell biology*, 18(3):128–35.

Kim, C. A. and Berg, J. M. (1996). A 2.2 Åresolution crystal structure of a designed zinc finger protein bound to DNA. *Nature Structural Biology*, 3(11):940–945.

Kon, T., Oyama, T., Shimo-Kon, R., Imamula, K., Shima, T., Sutoh, K., and Kurisu, G. (2012). The 2.8 Åcrystal structure of the dynein motor domain. *Nature*, 484(7394):345–50.

Korten, T., Birnbaum, W., Kuckling, D., and Diez, S. (2012). Selective control of gliding microtubule populations. *Nano letters*, 12(1):348–53.

Korten, T. and Diez, S. (2008). Setting up roadblocks for kinesin-1: mechanism for the selective speed control of cargo carrying microtubules. *Lab on a chip*, 8(9):1441–7.

Kozielski, F., Sack, S., and Marx, A. (1997). The crystal structure of dimeric kinesin and implications for microtubule-dependent motility. *Cell*, 91(7):985–994.

Kull, F. J., Vale, R. D., and Fletterick, R. J. (1998). The case for a common ancestor: kinesin and myosin motor proteins and G proteins. *Journal of muscle research and cell motility*, 19(8):877–86.

Kuo, S. C., Gelles, J., Steuer, E., and Sheetz, M. P. (1991). A model for kinesin movement from nanometer-level movements of kinesin and cytoplasmic dynein and force measurements. *Journal of cell science. Supplement*, 14:135–8.

Landau, L. D. and Lifšic, E. M. (1995). *Fluid Dynamics*. Butterworth-Heinemann.

Lata, S., Reichel, A., Brock, R., Tampé, R., and Piehler, J. (2005). High-affinity adaptors for switchable recognition of histidine-tagged proteins. *Journal of the American Chemical Society*, 127(29):10205–15.

Lawrence, C. J., Dawe, R. K., Christie, K. R., Cleveland, D. W., Dawson,

S. C., Endow, S. a., Goldstein, L. S. B., Goodson, H. V., Hirokawa, N., Howard, J., Malmberg, R. L., McIntosh, J. R., Miki, H., Mitchison, T. J., Okada, Y., Reddy, A. S. N., Saxton, W. M., Schliwa, M., Scholey, J. M., Vale, R. D., Walczak, C. E., and Wordeman, L. (2004). A standardized kinesin nomenclature. *The Journal of cell biology*, 167(1):19–22.

Leduc, C., Padberg-Gehle, K., Varga, V., Helbing, D., Diez, S., and Howard, J. (2012). Molecular crowding creates traffic jams of kinesin motors on microtubules. *Proceedings of the National Academy of Sciences of the United States of America*, 109(16):6100–5.

Lindemann, C. B. and Lesich, K. a. (2010). Flagellar and ciliary beating: the proven and the possible. *Journal of cell science*, 123(Pt 4):519–28.

Ma, Y.-Z. and Taylor, E. W. (1997). Interacting Head Mechanism of Microtubule-Kinesin ATPase. *Journal of Biological Chemistry*, 272(2):724–730.

Malcos, J. L. and Hancock, W. O. (2011). Engineering tubulin: microtubule functionalization approaches for nanoscale device applications. *Applied microbiology and biotechnology*, 90(1):1–10.

Mather, W. H. and Fox, R. F. (2006). Kinesin's biased stepping mechanism: amplification of neck linker zippering. *Biophysical journal*, 91(7):2416–26.

Miyazono, Y., Hayashi, M., Karagiannis, P., Harada, Y., and Tadakuma, H. (2009). Strain through the neck linker ensures processive runs: a DNA-kinesin hybrid nanomachine study. *The EMBO Journal*, 29(1):93–106.

Mori, T., Vale, R. D., and Tomishige, M. (2007). How kinesin waits between steps. *Nature*, 450(7170):750–4.

Moritz, M., Braunfeld, M., and Fung, J. (1995). Three-dimensional structural characterization of centrosomes from early Drosophila embryos. *The Journal of cell ...*, 130(5):1149–1159.

Narayana, N. and Weiss, M. a. (2009). Crystallographic analysis of a sex-specific enhancer element: sequence-dependent DNA structure, hydration, and dynamics. *Journal of molecular biology*, 385(2):469–90.

Nédélec, F. and Surrey, T. (2001). Dynamics of microtubule aster formation by motor complexes. *Comptes Rendus de l'Académie des Sciences - Series IV - Physics*, 2(6):841–847.

Nédélec, F., Surrey, T., and Maggs, A. (2001). Dynamic Concentration of Motors in Microtubule Arrays. *Physical Review Letters*, 86(14):3192–3195.

Nédélec, F. J., Surrey, T., Maggs, A. C., and Leibler, S. (1997). Self-organization of microtubules and motors. *Nature*, 389(6648):305–308.

Nilsson, H. and Wallin, M. (1997). Evidence for several roles of dynein in pigment transport in melanophores. *Cell motility and the cytoskeleton*, 38(4):397–409.

Nogales, E., Wolf, S. G., and Downing, K. H. (1998). electron crystallography. 391(January):199–204.

Ortega-Arroyo, J. and Kukura, P. (2012). Interferometric scattering microscopy (iSCAT): new frontiers in ultrafast and ultrasensitive optical microscopy. *Physical chemistry chemical physics : PCCP*, 14(45):15625–36.

Papworth, M., Moore, M., Isalan, M., Minczuk, M., Choo, Y., and Klug, A. (2003). Inhibition of herpes simplex virus 1 gene expression by designer zinc-finger transcription factors. *Proceedings of the National Academy of Sciences of the United States of America*, 100(4):1621–1626.

Popodi, E. M., Hoyle, H. D., Turner, F. R., Xu, K., Kruse, S., and Raff, E. C. (2008). Axoneme specialization embedded in a "generalist" beta-tubulin. *Cell motility and the cytoskeleton*, 65(3):216–37.

Qian, L., Winfree, E., and Bruck, J. (2011). Neural network computation with DNA strand displacement cascades. *Nature*, 475(7356):368–372.

Qiu, W., Derr, N. D., Goodman, B. S., Villa, E., Wu, D., Shih, W., and Reck-Peterson, S. L. (2012). Dynein achieves processive motion using both

stochastic and coordinated stepping. *Nature structural & molecular biology*, 19(2):193–200.

Ray, S. (1993). Kinesin follows the microtubule's protofilament axis. *The Journal of Cell Biology*, 121(5):1083–1093.

Resto, P. J., Mogen, B. J., Berthier, E., and Williams, J. C. (2010). An automated microdroplet passive pumping platform for high-speed and packeted microfluidic flow applications. *Lab on a Chip*, 10(1):23.

Rice, S., Cui, Y., Sindelar, C., Naber, N., Matuska, M., Vale, R., and Cooke, R. (2003). Thermodynamic properties of the kinesin neck-region docking to the catalytic core. *Biophysical journal*, 84(3):1844–54.

Rice, S., Lin, a. W., Safer, D., Hart, C. L., Naber, N., Carragher, B. O., Cain, S. M., Pechatnikova, E., Wilson-Kubalek, E. M., Whittaker, M., Pate, E., Cooke, R., Taylor, E. W., Milligan, R. a., and Vale, R. D. (1999). A structural change in the kinesin motor protein that drives motility. *Nature*, 402(6763):778–84.

Rogers, A. R., Driver, J. W., Constantinou, P. E., Kenneth Jamison, D., and Diehl, M. R. (2009). Negative interference dominates collective transport of kinesin motors in the absence of load. *Physical chemistry chemical physics : PCCP*, 11(24):4882–9.

Rogers, S. L., Rogers, G. C., Sharp, D. J., and Vale, R. D. (2002). Drosophila EB1 is important for proper assembly, dynamics, and positioning of the mitotic spindle. *The Journal of cell biology*, 158(5):873–84.

Romberg, L., Pierce, D. W., and Vale, R. D. (1998). Role of the kinesin neck region in processive microtubule-based motility. *The Journal of cell biology*, 140(6):1407–16.

Rothemund, P. W. K. (2006). Folding DNA to create nanoscale shapes and patterns. *Nature*, 440(7082):297–302.

Ruhnow, F., Zwicker, D., and Diez, S. (2011). Tracking single particles and elongated filaments with nanometer precision. *Biophysical journal*, 100(11):2820–8.

Sanchez, T., Welch, D., Nicastro, D., and Dogic, Z. (2011). Cilia-like beating of active microtubule bundles. *Science*, 333(6041):456–459.

Sanderson, M. J. and Sleigh, M. a. (1981). Ciliary activity of cultured rabbit tracheal epithelium: beat pattern and metachrony. *Journal of cell science*, 47:331–47.

Satir, P. (2011). Coiled-coils and motile cilia. *Nature genetics*, 43(1):10–1.

Schief, W. R., Clark, R. H., Crevenna, A. H., and Howard, J. (2004). Inhibition of kinesin motility by ADP and phosphate supports a hand-over-hand

mechanism. *Proceedings of the National Academy of Sciences of the United States of America*, 101(5):1183–8.

Schmidt, C. and Vogel, V. (2010). Molecular shuttles powered by motor proteins: loading and unloading stations for nanocargo integrated into one device. *Lab on a Chip*, 10(17):2195–2198.

Schnitzer, M. J. and Block, S. M. (1997). Kinesin hydrolyses one ATP per 8-nm step. *Nature*, 388(6640):386–90.

Schnitzer, M. J., Visscher, K., and Block, S. M. (2000). Force production by single kinesin motors. *Nature cell biology*, 2(10):718–23.

Seeman, N. C. (1982). Nucleic acid junctions and lattices. *Journal of theoretical biology*, 99(2):237–47.

Seitz, A. and Surrey, T. (2006). Processive movement of single kinesins on crowded microtubules visualized using quantum dots. *The EMBO Journal*, 25(2):267.

Shibata, Y., Kumar, P., Layer, R., Willcox, S., Gagan, J. R., Griffith, J. D., and Dutta, A. (2012). Extrachromosomal microDNAs and chromosomal microdeletions in normal tissues. *Science (New York, N.Y.)*, 336(6077):82–6.

Simmel, F. C. (2012). DNA-based assembly lines and nanofactories. *Current opinion in biotechnology*, 23(4):521–516.

Sjø ttem, E., Andersen, C., and Johansen, T. (1997). Structural and functional analyses of DNA bending induced by Sp1 family transcription factors. *Journal of molecular biology*, 267(3):490–504.

Song, Y. H. and Mandelkow, E. (1993). Recombinant kinesin motor domain binds to beta-tubulin and decorates microtubules with a B surface lattice. *Proceedings of the National Academy of Sciences of the United States of America*, 90(5):1671–5.

Spoerke, E. D., Bachand, G. D., Liu, J., Sasaki, D., and Bunker, B. C. (2008). Directing the polar organization of microtubules. *Langmuir : the ACS journal of surfaces and colloids*, 24(14):7039–43.

Stellwagen, E. and Stellwagen, N. C. (2002). Determining the electrophoretic mobility and translational diffusion coefficients of DNA molecules in free solution. *Electrophoresis*, 23(16):2794–803.

Subramanian, R. and Kapoor, T. M. (2012). Building complexity: insights into self-organized assembly of microtubule-based architectures. *Developmental cell*, 23(5):874–85.

Sui, H. and Downing, K. H. (2010). Structural basis of interprotofilament

interaction and lateral deformation of microtubules. *Structure*, 18(8):1022–31.

Surrey, T., Nédélec, F., Leibler, S., and Karsenti, E. (2001). Physical properties determining self-organization of motors and microtubules. *Science*, 292(5519):1167.

Svoboda, K. and Block, S. M. (1994). Force and velocity measured for single kinesin molecules. *Cell*, 77(5):773–84.

Svoboda, K., Schmidt, C. F., Schnapp, B. J., and Block, S. M. (1993). Direct observation of kinesin stepping by optical trapping interferometry. *Nature*, 365(6448):721–727.

Takeda, S., Tsukiji, S., and Nagamune, T. (2004). Site-specific conjugation of oligonucleotides to the C-terminus of recombinant protein by expressed protein ligation. *Bioorganic & medicinal chemistry letters*, 14(10):2407–2410.

Taniguchi, Y., Nishiyama, M., Ishii, Y., and Yanagida, T. (2005). Entropy rectifies the Brownian steps of kinesin. *Nature chemical biology*, 1(6):342–7.

Telley, I. a., Bieling, P., and Surrey, T. (2009). Obstacles on the microtubule reduce the processivity of Kinesin-1 in a minimal in vitro system and in cell extract. *Biophysical journal*, 96(8):3341–53.

Thormählen, M., Marx, A., Müller, S., Song, Y.-H., Mandelkow, E.-M., Aebi, U., and Mandelkow, E. (1998). Interaction of monomeric and dimeric kinesin with microtubules. *Journal of Molecular Biology*, 275(5):795–809.

Thorn, K. S., Ubersax, J. a., and Vale, R. D. (2000). Engineering the processive run length of the kinesin motor. *The Journal of cell biology*, 151(5):1093–100.

Tomishige, M., Stuurman, N., and Vale, R. D. (2006). Single-molecule observations of neck linker conformational changes in the kinesin motor protein. *Nature structural & molecular biology*, 13(10):887–94.

Tomishige, M. and Vale, R. D. (2000). Controlling kinesin by reversible disulfide cross-linking. Identifying the motility-producing conformational change. *The Journal of cell biology*, 151(5):1081–92.

Tuma, M. C., Zill, A., Le Bot, N., Vernos, I., and Gelfand, V. (1998). Heterotrimeric kinesin II is the microtubule motor protein responsible for pigment dispersion in Xenopus melanophores. *Journal of Cell Biology*, 143(6):1547–1558.

Turberfield, a., Mitchell, J., Yurke, B., Mills, a., Blakey, M., and Simmel, F. (2003). DNA Fuel for Free-Running Nanomachines. *Physical Review Letters*, 90(11):1–4.

Uemura, S., Kawaguchi, K., Yajima, J., Edamatsu, M., Toyoshima, Y. Y., and Ishiwata, S. (2002). Kinesin-microtubule binding depends on both nucleotide state and loading direction. *Proceedings of the National Academy of Sciences of the United States of America*, 99(9):5977–81.

Vale, R., Reese, T., and Sheetz, M. (1985). Identification of a novel force-generating protein, kinesin, involved in microtubule-based motility. *Cell*, 42(1):39–50.

Vale, R. D. and Fletterick, R. J. (1997). The design plan of kinesin motors. *Annual review of cell and developmental biology*, 13(1):745–777.

Vale, R. D., Funatsu, T., Pierce, D. W., Romberg, L., Harada, Y., and Yanagida, T. (1996). Direct observation of single kinesin molecules moving along microtubules. *Nature*, 380(6573):451–3.

Varga, V., Leduc, C., Bormuth, V., Diez, S., and Howard, J. (2009). Kinesin-8 Motors Act Cooperatively to Mediate Length-Dependent Microtubule Depolymerization. *Cell*, 138(6):1174–1183.

Verhey, K. J., Kaul, N., and Soppina, V. (2011). Kinesin assembly and movement in cells. *Annual review of biophysics*, 40:267–88.

Walker, G. M. and Beebe, D. J. (2002). A passive pumping method for microfluidic devices. *Lab on a Chip*, 2(3):131–134.

Warner, F. D. and Satir, P. (1974). The structural basis of ciliary bend formation. Radial spoke positional changes accompanying microtubule sliding. *The Journal of cell biology*, 63(1):35–63.

Wei, B., Dai, M., and Yin, P. (2012). Complex shapes self-assembled from single-stranded DNA tiles. *Nature*, 485(7400):623–626.

Wickham, S. F. J., Endo, M., Katsuda, Y., Hidaka, K., Bath, J., Sugiyama, H., and Turberfield, A. J. (2011). Direct observation of stepwise movement of a synthetic molecular transporter. *Nature nanotechnology*, 6(3):166–9.

Williams, R. C. and Rone, L. a. (1989). End-to-end joining of taxol-stabilized GDP-containing microtubules. *The Journal of biological chemistry*, 264(3):1663–70.

Winfree, E., Liu, F., Wenzler, L. A., and Seeman, N. C. (1998). Design and self-assembly of two-dimensional DNA crystals. *Nature*, 394(6693):539–544.

Wollman, A. J. M., Sanchez-Cano, C., Carstairs, H. M. J., Cross, R. a., and Turberfield, A. J. (2013). Transport and self-organization across different length scales powered by motor proteins and programmed by DNA. *Nature nanotechnology*, (NOVEMBER):1–4.

Wordeman, L. (2005). Microtubule-depolymerizing kinesins. *Current opinion in cell biology*, 17(1):82–8.

Yajima, J., Alonso, M. C., Cross, R. a., and Toyoshima, Y. Y. (2002). Direct long-term observation of kinesin processivity at low load. *Current Biology*, 12(4):301–306.

Yajima, J. and Cross, R. A. (2005). A torque component in the kinesin-1 power stroke. *Nature cell biology*, 1(6):338–341.

Yildiz, A., Tomishige, M., Gennerich, A., and Vale, R. D. (2008). Intramolecular strain coordinates kinesin stepping behavior along microtubules. *Cell*, 134(6):1030–41.

Yildiz, A., Tomishige, M., Vale, R. D., and Selvin, P. R. (2004). Kinesin walks hand-over-hand. *Science*, 303(5658):676–8.

Yurke, B., Allen P. Mills, J., and Mills, A. (2003). Using DNA to Power Nanostructures. *Genetic Programming and Evolvable Machines*, 4(2):111–122.

Yurke, B., Turberfield, A. J., Mills, A. P., Simmel, F. C., and Neumann, J. L. (2000). A DNA-fuelled molecular machine made of DNA. *Nature*, 406(6796):605–8.

Zadeh, J. N., Wolfe, B. R., and Pierce, N. A. (2010). Nucleic acid sequence design via efficient ensemble defect optimization. *Journal of Computational Chemistry*, 32:439–452.

Zheng, Y., Wong, M. L., Alberts, B., and Mitchison, T. (1995). Nucleation of microtubule assembly by a gamma-tubulin-containing ring complex. *Nature*, 378(6557):578–83.